

Copyright  
by  
Karah Lynn Wertz  
2003

**The Dissertation Committee for Karah Lynn Wertz Certifies that this is the approved version of the following dissertation:**

**FROM SEAFLOOR SPREADING TO UPLIFT: THE  
STRUCTURAL AND GEOCHEMICAL EVOLUTION OF  
MACQUARIE ISLAND ON THE AUSTRALIAN-PACIFIC  
PLATE BOUNDARY**

**Committee:**

---

Sharon Mosher, supervisor

---

Jonathan Snow

---

James N. Connelly

---

William R. Muehlberger

**FROM SEAFLOOR SPREADING TO UPLIFT: THE  
STRUCTURAL AND GEOCHEMICAL EVOLUTION OF  
MACQUARIE ISLAND ON THE AUSTRALIAN-PACIFIC  
PLATE BOUNDARY**

**by**

**Karah Lynn Wertz, B.Sc.**

**Dissertation**

Presented to the Faculty of the Graduate School of

The University of Texas at Austin

in Partial Fulfillment

of the Requirements

for the Degree of

**Doctor of Philosophy**

**The University of Texas at Austin**

**December, 2003**

## **Dedication**

To my parents.

## **Acknowledgements**

This dissertation was made possible by many contributions from scientists around the globe. At times, there seemed to be too many obstacles to do the work that I wanted to, but with the help of many, I completed a study that I am proud of. Funding came from many sources: the Australian Antarctic Division, the University of Texas at Austin Jackson School for Geosciences Geology Foundation and Institute for Geophysics, the Max Planck Society, the University of Tasmania, and the Geological Society of America. Because this study has spanned 5.5 years, 6000 km by sea and countless kilometers by air, three universities, three continents, and one little island, these acknowledgements might seem a little long. But my gratitude is sincere, and I want those to whom I am grateful to know it. So bear with me.

Sharon was the sort of supervisor that every graduate student hopes for, and very few actually get. She has worn many hats during our acquaintance—advisor, boss, collaborator, teacher, student, confidant, cheerleader, and friend. She had the flexibility to let me strike out on my own but was capable of reining me back in, never letting me stray too far. She was always there to encourage me or give me a “reality check”, or to come to the rescue if I needed it, ultimately

enabling me to complete the single biggest achievement of my life. For this I will always be grateful.

I would like to thank my committee for their helpful comments which greatly improved this manuscript. Jon invited me to work and learn at the magnificent Max-Planck-Institut für Chemie in Mainz, believing in my work when others did not, exposing me to the wonderful world of geochemistry, and allowing me to grow as a scientist. I thank Bill and Jim for giving their time to read and make careful edits to my dissertation, and for their helpful criticism.

I earnestly thank Al Hofmann for making it possible for me to join the family at the Max Planck Institute. Eric Hellebrand taught me how to be a geochemist; his enthusiasm and endless patience in answering my endless questions made working with him a joy. Chapter 2 is the result of collaboration with Eric and Jon. Annette von der Handt gave me a happy place to live in Mainz, helped me navigate the rules and regulations of German living and taught me to not just operate, but to love the electron microprobe (it is really just a million-dollar Easy-Bake Oven). I will always remember my family in “The Container”- Gabriella Peressini, Melanie Griselin, and François Nauret, a group of castaway kindred souls who made life in a strange land really a lot of fun.

Leonid Danyushevsky at the University of Tasmania Centre for Ore Deposits Research was my collaborator on chapter 3. He taught me his methods for basalt geochemistry and supervised all of my analyses. He is one of the most meticulous scientists I have ever met, and I feel fortunate to have been able to learn from him.

I thank Nathan Daczko for his assistance and good times in the field, the fabulous field hut bread, and the bravery he showed in eating even my most creative field hut meals. I am grateful for his resilience in working with me in some of the most trying field conditions possible, and for all of the singing and laughter. Our collaboration of his geophysical interpretations and petrography with my field work resulted in chapter 4.

Bobbie John believed in me when I was an undergrad at the University of Wyoming, and has mentored me throughout my academic career, encouraging me to go to grad school, introducing me to the people who taught me about ophiolites and the ocean floor. She has been an inspiration and a friend, and I wouldn't be writing this now if it wasn't for her.

Two of the people Bobbie that introduced me to are Bob Miller and Greg Harper. Bob taught me how to map in field camp, and when I started my Ph.D. at the University of Texas, he taught me the basics of the ophiolite, showed me how to tell diabase from basalt and how to recognize pillow basalts through lichen, by taking me to the Coast Ranges in California and then letting me tag along with him to the Ingalls Complex Ophiolite. Greg Harper was a fantastic field partner (although perhaps a bit too intrepid at times...), and I feel lucky to have had him as a tour guide in what I will always think of as HIS ophiolite, the Josephine; there he showed me how to recognize an epidosite and an oceanic fault, giving me the basics for chapter one. I would also like to thank other people whom I met directly or indirectly through Bobbie, including Sue DeBari and Scott Patterson, for their outcrop conversations about petrology in the Ingalls complex, and the

Leg 176 Josephine Ophiolite field trip participants, especially Jon Snow, Henry Dick, Aaron Yoshinobu, Chris MacLeod, Kathy Gillis, Lawrence Coogan, Mike Cheadle and Benoit Ildefonse. From them I caught the seafloor bug, which developed into my love of the mysteries of the sea.

I would like to thank the Australian Antarctic Division who supported all of my field work, and I would also like to thank the expeditioners of the 53rd and 55th Macquarie Island Australian Antarctic Research Expeditions, especially (in no particular order,) Iain, Tore, Megs, Kiwi, Gerbil, Joe, Adam, Jason, Squeeze, Ingrid, Cath, Nick, Al B and Al D, Dale, Yassa, Doug and Doug, Kev, Rachael, Divine Miss Juzz, Alex, Kerri Anne, Georgie, A-man, Julio, Donald, Louise, and Sambo, a surrogate family that made life on the island even more wonderful. Robb Clifton and Simone Ingham offered their good humor and strong backs, helping me lug hundreds of kilos of rocks up and down the coasts of the island. Without their assistance, all those gabbros and peridotites couldn't have been sampled.

I have dedicated this work to my parents, Lana and Gene Wertz, who taught me to follow my heart and have supported me, not just in my geologic studies, but in everything I have chosen to do, from studying art in France, to flying off to Australia in pursuit of love, to dyeing my hair purple (okay, maybe not really SUPPORT, but at least they let me do it). They made my education happen; they paid the bills during my undergraduate days and encouraged me to take it as far as I could. They have been my safety net in this tightrope walk called life, and words cannot express the magnitude of my gratitude and love.

And finally I thank my beloved Corey for having understanding and patience as deep and wide as the ocean floor I study. It is not easy partnering a Ph.D. candidate, and I will be forever grateful for his enduring support and enthusiasm, for being my safe harbor in the tempest, for encouraging me through the toughest times, for being my best friend and lover and for always, always keeping me laughing. I love you with all of my heart.

**FROM SEAFLOOR SPREADING TO UPLIFT: THE  
STRUCTURAL AND GEOCHEMICAL EVOLUTION OF  
MACQUARIE ISLAND ON THE AUSTRALIAN-PACIFIC  
PLATE BOUNDARY**

Publication No. \_\_\_\_\_

Karah Lynn Wertz, Ph.D.

The University of Texas at Austin, 2003

Supervisor: Sharon Mosher

Macquarie Island (54°30'S, 158°54'E) is unique, consisting of a section of uplifted oceanic crust and upper mantle that still lies within the ocean basin where it formed. Earlier geophysical studies indicate that between ~40 and 6 Ma, this plate boundary evolved from a spreading ridge to the modern transpressional boundary. The rocks of Macquarie Island record both regimes. This study combines structural, geochemical and geophysical data to describe the evolution of Macquarie Island and the adjacent Australian-Pacific plate boundary from spreading to transpression.

The Finch-Langdon fault is the most significant spreading-related structure on the island, juxtaposing upper crust and intrusive/mantle rocks. On

the basis of structural and petrologic data, I propose that this fault zone formed near the inside corner of a ridge-transform intersection (RTI) and that structures on the island are conformable with those in the surrounding seafloor.

Geochemical data for Macquarie Island basalts and peridotites suggest a complex evolution during the last stages of seafloor spreading. The volcanic section consists of enriched basalts formed by low degrees of partial melting. Basalt geochemistry combined with stratigraphic relationships reveal early intervals of variable enrichment followed by periods of more constant, decreasing enrichment.

Peridotite and basalt geochemistries differ distinctly. Peridotites show characteristics of a high degree of melting (heavy rare earth element, or REE, and Al depletion), whereas low degrees of partial melting are inferred for the basalts. The mantle rocks also have spoon-shaped REE patterns and anomalous Sr enrichment. The depletion and trace element patterns are more typical of mantle rocks in ophiolites than of abyssal mantle.

Ridge propagation proximal to an RTI exposing lower crust/uppermost mantle would satisfy these structural and geochemical parameters.

Subsequently, transpression along the Australian-Pacific plate boundary has resulted in transform motion along the plate boundary and vertical deformation along the ~1500 km long Macquarie Ridge Complex. Uplift faults on the island are dominantly high-angle, en echelon, normal faults. The geometries and kinematics of the faults do not match predicted fault patterns for

transpression, but indicate domination by extensional relay zones between stepovers of faults along the plate boundary.

## Table of Contents

List of Tables .....	xvi
List of Figures.....	xviii
Introduction .....	1
The importance of mid ocean ridges .....	1
Geologic studies of Macquarie Island .....	2
Overview of dissertation: from seafloor spreading to uplift.....	4
<b>SEAFLOOR SPREADING HISTORY OF MACQUARIE ISLAND</b> .....	<b>6</b>
Chapter 1: A fossil ridge-transform intersection preserved on Macquarie Island .....	6
1.1 Abstract.....	6
1.2 Introduction .....	6
1.3 The Finch-Langdon Fault zone.....	8
1.3.1 New structural data.....	9
1.3.2 Mineralization.....	10
1.3.3 Rocks adjacent to the fault.....	12
1.4 Discussion.....	14
1.5 Conclusions .....	17
Chapter 2: The melting history of Macquarie Island mantle peridotites and its relationship to seafloor spreading.....	30
2.1 Abstract.....	30
2.2 Introduction .....	31
2.2.1 Tectonic setting.....	32
2.3 Methods .....	34
2.3.1 Field study .....	34
2.3.2 Laboratory techniques .....	35
2.4 Results .....	36

2.4.1 Mineral compositions .....	36
2.5 Discussion.....	37
2.5.1 Comparison with other peridotites: ophiolite or ocean crust? ....	37
2.5.2 Relationship of degree of melting to spreading rate.....	40
2.5.3 Trace element enrichment: Macquarie Island, abyssal peridotites and ophiolites.....	45
2.5.3.1 Spoon-shaped REE patterns .....	45
2.5.3.2 Positive Strontium anomalies .....	46
2.5.4 Alternative models for Macquarie Island geochemistry.....	49
2.6 Conclusions .....	52
Chapter 3: Temporal patterns of incompatible-element enrichment in Macquarie Island basalts .....	70
3.1 Abstract.....	70
3.2 Introduction .....	71
3.2 Methods .....	73
3.2.1 Field techniques.....	73
3.2.2 Analytical techniques .....	74
3.3 Results .....	75
3.3.1 Geology .....	75
3.3.1.1 Relative stratigraphic position.....	77
3.3.2 Geochemistry.....	80
3.3.2.1 Effects of alteration test.....	81
3.4 Discussion.....	82
3.4.1 Geochemical trends .....	82
3.4.2 Incompatible element enrichment .....	85
3.4.3 Evidence of ridge propagation? .....	87
3.5 Conclusions .....	90

## **UPLIFT HISTORY OF MACQUARIE ISLAND**

Chapter 4: Extension along the Australian-Pacific transpressional transform plate boundary near Macquarie Island.....	117
4.1 Introduction .....	117
4.2 Tectonic Setting.....	118
4.3 Macquarie Island field data .....	119
4.3.1 Fault rocks .....	122
4.3.2 Northern recent faults.....	122
4.3.3 Central recent faults.....	122
4.3.4 Southern recent faults .....	124
4.4 Discussion.....	125
4.4.1 Genesis of Macquarie Island recent faults.....	125
4.4.2 Marine geophysical analysis.....	126
4.4.3 Comparison of island and marine geophysical data .....	127
4.4.4 Model for formation of plate boundary faults .....	129
4.5 Conclusion.....	130
<b>SUMMARY AND MODEL</b>	<b>145</b>
Summary.....	145
A geologic model for Macquarie Island.....	148
References .....	155
Vita .....	169

## List of Tables

Table 2.1a	Average major element compositions of spinel of Macquarie Island peridotites.....	65
Table 2.1b	Average major element compositions of spinel of Macquarie Island peridotites.....	66
Table 2.2	Average major element compositions of spinel of Macquarie Island peridotites.....	67
Table 2.3a	Average major and trace element compositions of clinopyroxenes of Macquarie Island peridotites.....	68
Table 2.3b	Average major and trace element compositions of clinopyroxenes of Macquarie Island peridotites.....	69
Table 3.1a	Electron microprobe major element data, S, Cl, H <sub>2</sub> O (wt%) of Macquarie Island basaltic glass.....	104
Table 3.1b	Electron microprobe major element data, S, Cl, H <sub>2</sub> O (wt%) of Macquarie Island basaltic glass. . . . .	105
Table 3.2a	ICP-MS trace element data (ppm) of Macquarie Island basaltic glass. ....	106
Table 3.2b	ICP-MS trace element data (ppm) of Macquarie Island basaltic glass. ....	107
Table 3.2c	ICP-MS trace element data (ppm) of Macquarie Island basaltic glass. ....	108
Table 3.2d	ICP-MS trace element data (ppm) of Macquarie Island basaltic glass. ....	109

Table 3.2e	ICP-MS trace element data (ppm) of Macquarie Island basaltic glass. ....	110
Table 3.2f	ICP-MS trace element data (ppm) of Macquarie Island basaltic glass. ....	111
Table 3.2g	ICP-MS trace element data (ppm) of Macquarie Island basaltic glass. ....	112
Table 3.2h	ICP-MS trace element data (ppm) of Macquarie Island basaltic glass. ....	113
Table 3.2i	ICP-MS trace element data (ppm) of Macquarie Island basaltic glass. ....	114
Table 3.2j	ICP-MS trace element data (ppm) of Macquarie Island basaltic glass. ....	115
Table 3.2k	ICP-MS trace element data (ppm) of Macquarie Island basaltic glass. ....	116
Table 4.1a	Recent fault data. ....	142
Table 4.1b	Recent fault data. ....	143
Table 4.1c	Recent fault data. ....	144

## List of Figures

Figure 1.1	Generalized geologic map .....	18
Figure 1.2	Bathymetry of the Macquarie Ridge Complex near Macquarie Island .....	19
Figure 1.3	Finch-Langdon fault trace superimposed on topography .....	20
Figure 1.4	The Finch-Langdon Fault at Bauer Bay .....	21
Figure 1.5	The Finch-Langdon Fault at Finch Creek .....	22
Figure 1.6	Photomicrographs .....	23
Figure 1.7	Sulfide alteration in the Finch-Langdon Fault zone .....	24
Figure 1.8	Mineral-filled fractures in diabase dikes .....	25
Figure 1.9	Gabbro mylonites .....	26
Figure 1.10	Sedimentary rocks .....	27
Figure 1.11	Talus breccia .....	28
Figure 1.12	Proposed tectonic setting of Finch-Langdon fault: a ridge- transform intersection .....	29
Figure 2.1	Location map of Macquarie Island .....	53
Figure 2.2	Geologic map of Macquarie Island .....	54
Figure 2.3	Detailed geologic maps for areas sampled .....	54
Figure 2.4	Cr-number vs. $\text{TiO}_2$ in spinel .....	56
Figure 2.5	$\text{Al}_2\text{O}_3$ vs. Mg-number .....	57
Figure 2.6	Rare earth elements and trace elements .....	58
Figure 2.7	Yb vs. Cr-number .....	59
Figure 2.8	Ce/Nd, Sr/Sr* vs. Yb .....	60

Figure 2.9	Changing spreading direction.....	61
Figure 2.10	Slab contamination of the mantle.....	62
Figure 2.11	Small-scale subduction.....	63
Figure 2.12	Rifting of pre-existing transform.....	64
Figure 3.1	Simplified geologic map of Macquarie Island.....	92
Figure 3.2	Stratigraphic columns.....	93
Figure 3.3	Stratigraphic columns.....	94
Figure 3.4	Pillow basalt, hyaloclastite.....	95
Figure 3.5	Pillow-rich hyaloclastite.....	96
Figure 3.6	Preserved submarine volcanoes at Pyramid Peak.....	97
Figure 3.7	Major element vs. MgO variation diagrams.....	98
Figure 3.8	Trace element vs. MgO variation diagrams for MI basaltic glass ..	99
Figure 3.9	Macquarie Island trace element analyses. .	100
Figure 3.10:	Degree of fractionation vs. degree of enrichment in incompatible elements.....	101
Figure 3.11	Selected trace element columns.....	102
Figure 3.12	Alkali and silica contents of Macquarie Island basalts.....	103
Figure 4.1	3D perspective view of the MRC.....	132
Figure 4.2	Field data from Macquarie Island.....	133
Figure 4.3	Topographic profiles and faults, Macquarie Island.....	134
Figure 4.4	Recent Fault data.....	135
Figure 4.5	The Brothers Fault.....	136
Figure 4.6	Brothers Fault transfer zones.....	137

Figure 4.7	Prion Lake and Red River .....	138
Figure 4.8	Recent fault patterns .....	139
Figure 4.9	Block diagrams .....	140
Figure 4.10	Recent fault model.....	141
Figure A.1	Ridge propagation model.....	154

## **Introduction**

### **THE IMPORTANCE OF MID OCEAN RIDGES**

The mid-ocean ridge system that encircles the globe is by far the largest volcanic feature in the world and is the dynamic expression of convection processes in the Earth's mantle. These processes have influenced the origin and evolution of ocean basins, the movement of continents, and the physical and chemical evolution of our planet. Magmatism along the ridge creates oceanic crust, which covers >60% of the planetary surface, at a rate of  $\sim 20 \text{ km}^3/\text{year}$ . The interrelated magmatic, tectonic, and hydrothermal processes involved in the creation of oceanic lithosphere allow the mid-ocean ridge to be viewed as a single, complex, dynamic system of energy flow from the Earth's interior to the lithosphere and hydrosphere. Despite the primary importance of the mid-ocean ridge to the geological evolution of Earth, we remain remarkably ignorant of how the system works. In particular, we do not understand how ridges 'turn off', or change their sense of motion. This dissertation investigates this fundamental problem by combining field and geophysical data from a paleo-spreading center that changed into an active transform boundary about 6 million years ago. The boundary studied is the Macquarie Ridge Complex along the Australian-Pacific plate boundary south of New Zealand.

Macquarie Island is located between New Zealand and Antarctica on the eastern edge of the Australian-Pacific plate boundary ( $54^{\circ}30'S$ ,  $158^{\circ}56'E$ ). The island is the only sub-aerial exposure of the Macquarie Ridge Complex, a series

of bathymetric ridges and troughs between approximately 45°S to 56°S that occur along the plate boundary. The island is thought to be both the sole exposure of ocean crust unequivocally formed at a spreading ridge and uplifted in the ocean basin in which it formed; uplift was caused by transpression between the Australian and Pacific plates. Because of this unique geology, the island was inscribed on the World Heritage Site list in 1997 (Anonymous, 2000). Moreover, it presents a unique environment for study of structures and rocks that form during the formation of oceanic crust at spreading ridges as well as structures related to an active oceanic transform fault.

#### **GEOLOGIC STUDIES OF MACQUARIE ISLAND**

The first geologic map of Macquarie Island was produced by cartographer, surveyor and geologist Leslie Russell Blake (b.1890), during his epic field season as a member of Sir Douglas Mawson's 1911-1914 Australasian Antarctic Expedition. He mapped rock distributions and surveyed the entire island, working almost totally alone. His topographic maps remain some of the most accurate maps made on Macquarie Island, despite field hardships unparalleled since that expedition. He enlisted and joined the fighting in World War I in 1915, and he died in France on October 3, 1918. His work was published posthumously by Mawson, who was also a geologist (Mawson and Blake, 1943).

Macquarie Island was first identified as a section of ocean crust by Varne et al, (1969). Further primary investigations into the petrology, geochemistry and geologic setting of Macquarie Island were carried out by Varne and Rubenach (1971), Griffin and Varne (1978, 1983), Duncan and Varne (1988), and

Christodoulou (1994; Christodoulou et al., 1984). Early structural and geophysical studies were done by (Williamson, 1974, 1979, 1988; Williamson et al., 1981; Williamson and Rubenach, 1972). These studies were all carried out with the assumption that Macquarie Island was oceanic crust that had formed at the Indian-Antarctic spreading ridge. However, the radiometric age dates from rocks on the island were too young (Duncan and Varne, 1988) for the crust to have been formed and transported to its current position.

Recent marine geophysical studies have redefined the history of the seafloor surrounding Macquarie Island, and therefore the history of Macquarie Island rocks. Hayes and Talwani (1973) first suggested that extension may have occurred on the Australian-Pacific plate boundary at the latitude of Macquarie Island, which would resolve the age discrepancy. Later studies (Cande and Stock, in review; Cande et al., 2000; Keller et al., 2002; Lamarche et al., 1997; Massell et al., 2000; Wood et al., 1996) have led to a complete tectonic reevaluation of this region and the entire Australian-Pacific Plate boundary, and it is now known that spreading occurred between the Australian and Pacific Plates between ~40-6 Ma and that the rocks of Macquarie Island formed during the last stages of extension (Cande et al., 2000; Massell et al., 2000). Coinciding with these new studies, new geologic maps were published by Mineral Resources Tasmania and the Australian Antarctic Division (Goscombe and Everard, 1998) which greatly improved the detail of past maps. Goscombe and Everard also published the first new structural studies of the island (Goscombe and Everard, 2001). New geochemical studies of volcanic glasses (Kamenetsky, 2000; Kamenetsky and

Maas, 2002) revealed an unusual diversity in basalt geochemistry, and other petrological studies (Bazylev and Kamenetsky, 1998) presented major element geochemical data for Macquarie Island peridotites.

#### **OVERVIEW OF DISSERTATION: FROM SEAFLOOR SPREADING TO UPLIFT**

Recent interpretations of geophysical data collected around the island (Massell et al, 2000) show spreading fabric (faulted abyssal hills) that formed parallel to paleo-spreading centers. This spreading fabric has related perpendicular fracture zones on the seafloor surrounding the island that curve asymptotically into the plate boundary. This dissertation presents field data from Macquarie Island and interprets these data in this context, relating the structural and geochemical evolution of the rocks on the island to the seafloor history discerned from geophysical studies. The primary area of goal of the study was to determine what the rocks of Macquarie Island could reveal about the seafloor and tectonic processes that occurred during the evolution of this plate boundary. Questions were:

1) How did Macquarie Island fit in with the structures that were mapped on the seafloor? Specifically, which faults formed during seafloor spreading, and which formed during uplift? Was there a transitional phase? How were they different in style and orientation? And how did they interact with each other, if at all?

2) Geochemically, what happened within the magmatic system as spreading was shutting down? How did these changes affect mantle melting and

the formation of crust as expressed in the geochemistry of the erupted basalts and residual peridotites?

The first part of the dissertation focuses on structures that formed and magmatic processes that occurred during seafloor spreading. I have identified the most significant fault zone on the island as one that formed during slow seafloor spreading, at the intersection of a ridge and a transform, which I have named the Finch-Langdon fault (chapter 1). I did not find evidence for a transitional phase between spreading and uplift. Chapters 2 and 3 present geochemical studies of the mid-ocean ridge basalts erupted during sea-floor spreading and residual mantle peridotites remaining from melt production. I found that these groups of rocks have very different major and trace element geochemical signatures, and represent different periods of the spreading history: an earlier, higher volume melting episode (represented by depleted mantle peridotites) and a later episode that produced basalts enriched in incompatible elements, the product of smaller volume melting. In the Summary and Model section at the end of the dissertation, I present a possible model to unite these seemingly disparate data.

# **SEAFLOOR SPREADING HISTORY OF MACQUARIE ISLAND**

## **Chapter 1: A fossil ridge-transform intersection preserved on Macquarie Island**

### **1.1 ABSTRACT**

Macquarie Island consists of uplifted oceanic crust that still lies within the ocean basin where it formed. As such it is unique; structures mapped on land may be placed into their regional oceanic tectonic context. The Finch-Langdon fault is the most significant spreading-related structure on the island, juxtaposing upper crust against lower crust and upper mantle rocks. It consists of dominantly oblique strike-slip, NW-, WNW-, and NNE-striking fault segments that bear hydrothermal mineralization indicative of faulting during seafloor spreading. Talus breccias and greywackes overlain by volcanic flows proximal to the fault indicate a long-lived submarine fault scarp that exposed diabase dikes and gabbros during volcanism. Swath reflectivity and bathymetry reveal ridge-parallel spreading fabric and perpendicular fracture zones, the closest ~7 km east of the island. On the basis of field and marine geophysical data, I propose that this fault zone formed near the inside corner of a ridge-transform intersection and structures on the island are conformable with those in the surrounding seafloor.

### **1.2 INTRODUCTION**

Macquarie Island is the sole sub-aerial exposure of a complete section of oceanic crust found in the ocean basin in which it formed (Fig. 1.1) (Varne et al.,

1969; Varne, 2000), thus offering a unique window into the tectonic, magmatic, and hydrothermal processes associated with seafloor spreading and transform faulting. The crust of Macquarie Island formed ~10 million years ago (Duncan and Varne, 1988) at a spreading ridge segment along the Australian-Pacific plate boundary (Varne et al, 2000). Regional marine geophysical data (Massell et al., 2000) show tectonic spreading fabric (faulted abyssal hills) that formed parallel to spreading ridge segments with associated perpendicular fracture zones (Figure 1.2). These fracture zones, spreading fabric, and magnetic anomalies demonstrate that spreading, which started in Eocene time, became increasingly oblique until extension was nearly parallel to the present-day plate boundary, evolving into the transform plate boundary observed today (e.g. Cande et al., 2000; Lamarche et al., 1997; Massell et al., 2000) (Figure 1.2). Transpression along the plate boundary is deforming adjacent oceanic crust to produce the Macquarie Ridge Complex (MRC) with Macquarie Island as its highest point. Spreading fabric can be traced continuously onto the MRC where it is cut by faults related to the current transform plate boundary (Massell et al., 2000). Therefore, the oceanic crust exposed on Macquarie Island formed during the last stages of seafloor spreading along short ridge segments separated by transform faults before volcanism shut off; magnetic anomalies on both plates (Wood et al., 1996, Massell, Meckel, Keller, pers. com.) show both right- and left-stepping ridge segments, including those that project toward Macquarie Island.

Macquarie Island is composed of an upper mantle-lower crust section that is juxtaposed against upper crust by the Finch-Langdon (F-L) fault (Figure 1.1).

The many faults that cut Macquarie Island can be grouped into two major categories: 1) spreading-related faults and 2) recent faults that formed in the subsequent transform or transpressional setting following the cessation of volcanism. The two groups differ markedly in faulting style and orientation. I describe the spreading-related faults below. Recent faults related to the present tectonic regime do not bear hydrothermal mineralization, generally strike northeast, and have pronounced fault scarps. Herein I present the results of field and petrologic investigations of the F-L fault zone and combine these new data with interpretations of surrounding major submarine structures. My results indicate formation of the F-L fault zone near the inside corner of a spreading ridge- transform fault intersection (RTI). This interpretation explains the geology (Varne et al., 2000) and early structures (Goscombe and Everard, 2001) on the island in a tectonic context that is compatible with marine geophysical data (Massell et al., 2000).

### **1.3 THE FINCH-LANGDON FAULT ZONE**

The F-L fault is the most significant spreading-related structure on the island, placing lower crust and mantle rocks in the north against upper crust rocks in the south (Figure 1.1); it is the only fault exposed on the island with such significant displacement, and the highest concentration of faults on the island is adjacent to the F-L fault. It consists of seven segments, ranging in length from 0.5 km-2.25 km that join at high angles (Figure 1.3).

I investigated these previously mapped (Goscombe and Everard, 2001; Mawson and Blake, 1943) fault segments to determine the tectonic setting during

formation (spreading- vs. transform-related), orientation, cross-cutting relationships, kinematics, and extent. Whereas the F-L fault is poorly exposed overall, subsidiary fault planes are plentiful in stream cuts and along the plateau's escarpment in a 200 m wide zone; sparse outcrops vary from 1-60 m<sup>2</sup> and contain fault planes that are generally <1 m<sup>2</sup>. Subsidiary fractures and faults associated with motion on the F-L fault are observed up to ~1 km on both sides of the fault. The fault is best identified by the juxtaposition of different lithologies, linear valleys, and a zone of subsidiary faults that mimic the larger feature.

No dramatic fault scarps are found within the zone, although the fault has affected the topography in some places by enhancing erosion. The northern half (~340° strike) exposed on the west coast has no geomorphological expression. The southern half of the fault (~280° strike) generally coincides with a ~1 km wide, irregular depression, but for the most part lies along the valley edge (Figure 1.3). Two segments displaying some topographical relief are on the west coast above Bauer Bay (025° strike) that parallels the escarpment (Figure 1.4a, 1.4b), and on the east coast above Sandy Bay, where a (350° strike) segment forms a 2 m deep depression with no fresh scarp (Figure 1.5). These short segments roughly parallel the modern day plate boundary (014° strike) and may have undergone minor re-activation, enhancing relief.

### **1.3.1 New structural data**

The seven segments of the F-L fault fall into three orientation groups: 280°-295°, 330°-350°, and ~20°, that form high-angle intersections pointing to the southwest or northeast (Figure 1.3). The faults forming this unusual pattern were

confirmed by changes in lithology and the presence of faults and fault rocks observed along their traces. Neither the mineralized faults nor eroded faults described above appear to truncate one another.

The subsidiary faults are grouped into three orientation regions along the F-L fault zone (Figure 1.3). In all cases, the outcrop-scale, mineralized faults within the zone are similar in orientation to nearby traces of the F-L fault (Figure 1.3a-1.3c), indicating that they are related to the larger system. Most outcrop-scale faults dip steeply and have moderately to shallowly plunging mineral fiber slickenlines (Figure 1.3a-1.3c) with rare steps indicating dextral oblique slip; I observe one sinistral oblique slip and one thrust fault. At Langdon Point, a 15 m long listric normal fault within pillow basalts has four SE-dipping splays that join in one sub-horizontal plane containing epidote slickenlines. At Langdon Bay, the main fault is exposed as a highly fractured  $\sim 160 \text{ m}^2$  plane (330/90), but wave erosion has removed much of the mineralized surface.

### **1.3.2 Mineralization**

Faults are common pathways for hydrothermal circulation associated with seafloor spreading, resulting in fault planes that are cemented with and/or have slickenlines composed of hydrothermal minerals, such as prehnite, epidote, actinolite, sulfides and quartz (Alexander and Harper, 1992). Rock adjacent to the fault is usually hydrothermally altered and/or fractured and has veins filled with hydrothermal minerals. The only high temperature hydrothermal circulation that Macquarie Island has experienced was during seafloor spreading; thus, the

presence of these hydrothermal minerals indicates faulting associated with seafloor spreading.

Along the length of the F-L fault, small fault planes and fault rocks contain hydrothermal minerals. Slickenlines composed of epidote, prehnite and/or retrograde chlorite occur as thin mineral fibers on fault planes. Hydrothermal minerals also cement fault breccia. For example, gabbros adjacent to the fault contain meter-scale faults characterized by 0.5-2 cm thick cataclastic zones of angular clinopyroxene and plagioclase rock fragments cemented by undeformed prehnite (Figure 1.6a). In addition, these fault surfaces are scored by mineral slickenlines indicating dextral oblique slip. The F-L fault zone also contains foliated cataclastite with superimposed shear bands. Small nuggets of hydrothermal epidote are part of the cataclastic material in the brittle sheared rock and prehnite veins truncate the sheared material, indicating faulting prior to and/or during active hydrothermal activity on the seafloor (Figure 1.6b).

The western half of the fault contains exposures of two fault segments with sulfide-rich zones. Here, poorly exposed hydrothermally altered pillow lavas are indistinguishable from sheeted dikes (Figure 1.7a, 1.7b). These sulfide zones also contain many faults that are sub-parallel to the zone, some with slickenlines. Although sulfide deposits have been found at dike-pillow transitions in un-faulted contacts (Harper et al., 1988) faults in the F-L sulfide-rich zones indicate that this contact is not depositional.

Rocks adjacent to faults are extensively fractured, with fractures filled with one or more generations of mineralization consisting of prehnite, epidote,

zeolites, quartz, and/or carbonate (Figure 1.8). Multiple sets of these fractures cross-cut each other at high angles. In places, small (1-4 cm wide) calcium metasomatized shear zones (epidote, Ca-clinopyroxene replacement), are associated with prehnite and epidote veins, and faults. Pervasive sulfide alteration is also common, with abundant pyrite, amphibole, chlorite and epidote in gabbro, diabase and basalt.

### **1.3.3 Rocks adjacent to the fault**

North of the fault, sheeted dikes strike primarily northwest (Figure 1.3d) with dips of 20-80° N and S. Although the dike strikes vary, the dikes are commonly sub-parallel to the adjacent segment of the F-L fault, suggesting that the sheeted dike anisotropy may have controlled the initial orientation of some segments of the F-L fault. Hydrothermal mineral-filled fractures are numerous near the fault, and dikes immediately adjacent contain abundant meter-scale faults filled with cataclastite. Gabbros adjacent to the fault exhibit small (~20 cm wide), ubiquitous mylonite zones (Figure 1.9a, 1.9b) in addition to the fractures and faults described above; most dip steeply (70-90° N and S) with nearly vertical lineations, striking ~150° parallel to the adjacent northwest end of the F-L fault (Figure 1.3e). The sub-parallelism of mylonite zones to the fault suggest they may be related to an early stage of fault motion.

The upper crustal section south of the fault consists of pillow basalts, inter-bedded with massive basalt flows, hyaloclastites, and sedimentary rocks that are exposed in nearly continuous sections for over 10 km in coastal outcrops. Directly adjacent to the fault on the west coast, pillow basalts are overturned,

dipping steeply to the north, but farther from the fault the units are generally upright, dipping moderately to the south. Although outcrop-scale spreading related faults are observed across Macquarie Island, hydrothermally mineralized outcrop-scale faults are most abundant in an approximately 1 km wide zone on either side of the F-L fault.

Talus breccias and other sedimentary rocks are inter-bedded with the volcanic rocks on the west coast for at least 4 km south of the fault (Figure 1.10). Talus breccias are clast supported with mud matrices; clasts are basalt, diabase and gabbro. Greywackes are poorly sorted and contain angular clasts of oxides, de-vitrified glass, clinopyroxene, plagioclase, chlorite, carbonate, epidote, prehnite and lithic clasts of basalt, diabase and gabbro. Rare pink and white limestone and thinly banded chert are exposed.

The largest talus breccia on the island (~150 m wide and ~140 m thick) lies at the southern end of Bauer Bay 500 m from the F-L fault. This breccia is cut by diabase dikes (Figure 1.10b) and is overlain by a repeating sequence of greywacke with rare chert interspersed with volcanic rocks that continues for nearly 2 km (Figure 1.10a). About 700 m from the fault at Douglas Point is another significant sedimentary package that consists of a clast-supported breccia (clasts  $\leq$  40 cm, some red mud matrix) that fines upward to greywacke (Figure 1-11). The package is ~4 m thick, contains gabbro clasts, and is overlain by a basalt flow. These sequences confirm concurrent active volcanism and shedding of clastic material from a large submarine fault scarp. The abundance of talus

breccia and sedimentary rocks on the west coast and general lack along the east coast indicate a topographic high existed to the northeast.

#### **1.4 DISCUSSION**

Macquarie Island is dissected by numerous faults that formed during seafloor spreading and younger faults that formed during transform motion and uplift of the island, following the cessation of spreading. The F-L fault is unique in the magnitude of uplift, the complicated geometry of the fault segments, and the extent and provenance of the sedimentary rocks most likely shed off its fault scarp. Other major spreading-related faults, such as those in the southern part of the island, place sheeted dikes or pillow basalts next to pillow basalts (Figure 1.1) and do not have such thick associated sedimentary packages. The recent faults are also very different with dramatic, fresh fault scarps and no hydrothermal mineralization. Only two segments of the F-L fault have some topographic expression, suggesting some reactivation during uplift; most are not in appropriate orientations for reactivation. The delicate mineral slickenlines preserved on discrete fault planes throughout the F-L zone also argue against major recent reactivation.

At submarine ridge-transform intersections (RTIs) two regions are observed: 1) the “outside” corner ridge-aseismic fracture zone intersection, and 2) the “inside” corner active RTI (Collette, 1986; Severinghaus, 1988) (Figure 1.12). On the outside corner, hot and thin new crust is added adjacent to previously sheared crust; however, little or no further motion takes place along the fracture zone. The inside corner crust is thickened and relief increases as new crust is

added to the edge of the active transform valley (Severinghaus, 1988). Extensive faulting (including detachment faults) exposes deeper rocks whereas rocks in the outside corner are usually basaltic (Karson and Dick, 1983).

At RTIs, structures form in response to tectonic motion on the spreading ridge interacting with the motion on the transform fault. The result is a complex array of structures that form parallel to the spreading ridge, parallel to the transform fault, and oblique to both (Fox and Gallo, 1984) but in the general orientation predicted for formation of faults in a simple shear system along the transform fault (Figure 1.12). A model for deformation at inside corners (Allerton and Vine, 1992), based on observations of the Troodos Ophiolite where a fossil transform-ridge intersection has been described (MacLeod et al., 1990; Moores and Vine, 1971) proposes that the outside corner is dominated by normal faulting, whereas the inside corner experiences both normal and strike slip faulting.

I propose that the F-L fault formed within an inside corner of a RTI (Figure 1.13). Swath reflectivity and bathymetric data in the ocean basin directly east of the island indicate roughly E-W oriented spreading fabric perpendicular to a fracture zone ~7 km from the island (Figures 1.2 and 1.12; Daczko et al., 2003; Massell et al., 2000) Sheeted dikes and spreading-related extensional faults on the island are consistent with the spreading fabric orientations in the swath reflectivity and bathymetric data.

Using interpretations of the marine geophysical data east of the island, I place the unusual geometry of the F-L fault (many short faults at high angles and junctions that point to the southwest or northeast) into a larger oceanic tectonic

context: some F-L fault segments parallel the offshore relict transform fault (fracture zone; north-northeast,) some parallel the relict spreading center (spreading fabric; west-northwest,) and others are oblique to both (northwest). Pervasive hydrothermal mineralization on outcrop-scale faults and alteration along the fault zone are consistent with deformation in a mid-ocean ridge environment. The predominately oblique normal and strike slip faulting along the F-L fault zone is most consistent with fault kinematics within the inside corner of the RTI (Allerton and Vine, 1992). I observed no detachment faults, and mylonite foliations/lineations in the adjacent gabbros also have steep dips/plunges, suggesting the high angle faults first had normal motion and were reactivated with the observed oblique slip motion during further shearing at the RTI. The predominately dextral shear on faults at high angles or oblique to the relict transform fault suggests counterclockwise rotation of fault blocks in an overall sinistral transform zone; the one observed sinistral fault parallel to the relict transform fault supports this interpretation. The talus deposits and angular, unsorted greywackes most likely formed at the base of fault scarps, and their distribution indicates a topographic high to the northeast that is consistent with the location of the lower crust and mantle exposures. Gabbro clasts in the talus breccias and greywackes (Figure 1.11, inset) indicate that gabbros were exposed on the seafloor as commonly occurs in inside corner environments. Furthermore, the volcanic rocks overlying sediments show that volcanism was contemporaneous with sediment deposition. With an inside corner interpretation, the orientation of the oblique faults relative to the spreading fabric and fracture

zones, as well as the location of the paleo-topographic high, require the island to be adjacent to a sinistral transform fault. Such a configuration is reasonable based on the observed magnetic anomalies that predict right and left stepping ridge segments projecting toward the island. The present day dextral transform fault formed later, after volcanism shut off, cross-cutting the short ridge segments.

## **1.5 CONCLUSIONS**

Macquarie Island provides an exceptional opportunity to observe seafloor processes and features on land where the tectonic context is preserved in the surrounding seafloor. The Finch-Langdon fault zone, based on the fault pattern, mineralization, and associated sedimentary deposits, coupled with the tectonic setting documented by marine geophysical data, is best explained as having formed in an inside corner of an active RTI near the end of the oblique spreading phase.

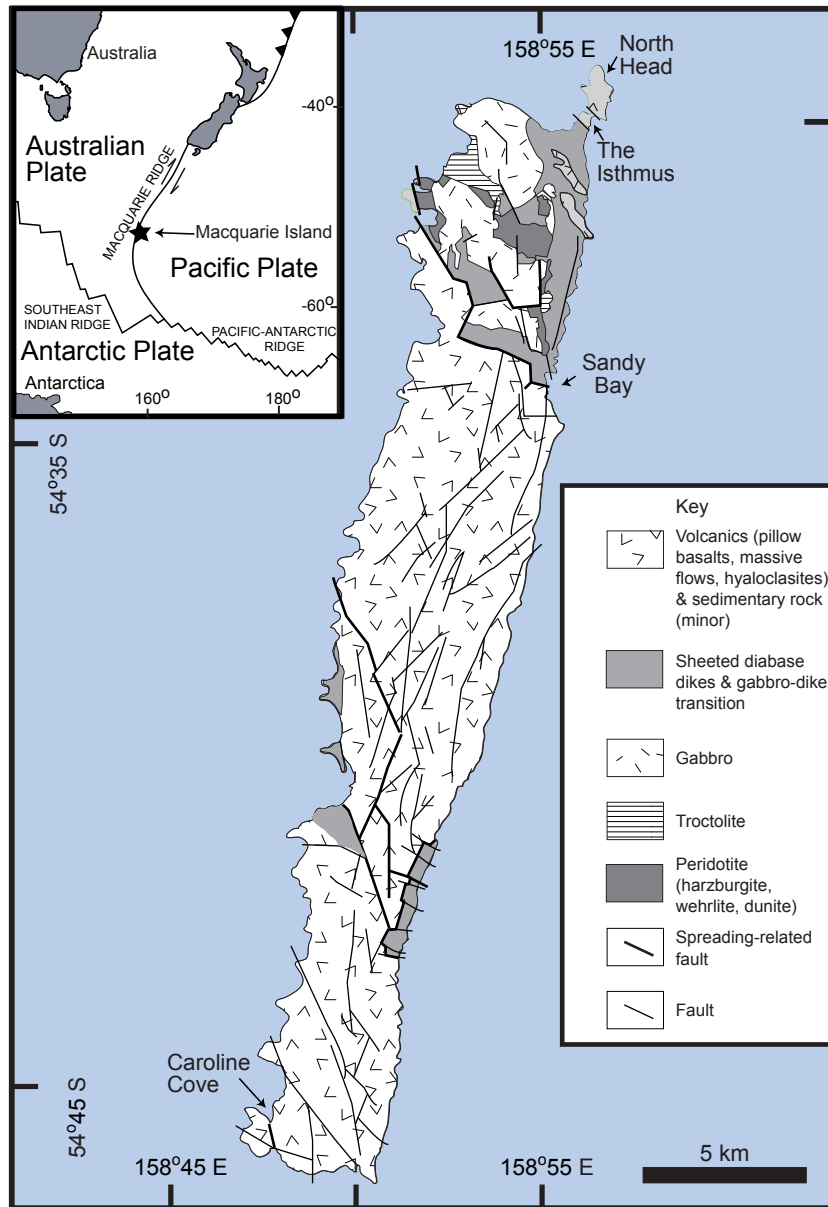


Figure 1.1. Generalized geologic map after Goscombe and Everard (2001). The Finch-Langdon fault, a seafloor spreading-related structure, juxtaposes serpentinized peridotite, gabbroic rocks, and sheeted diabase dikes (northern fourth of island) with volcanic rocks (southern part of island). Faults that formed during both seafloor spreading and uplift of island dissect terrain. Inset shows island location on Australian-Pacific plate boundary.

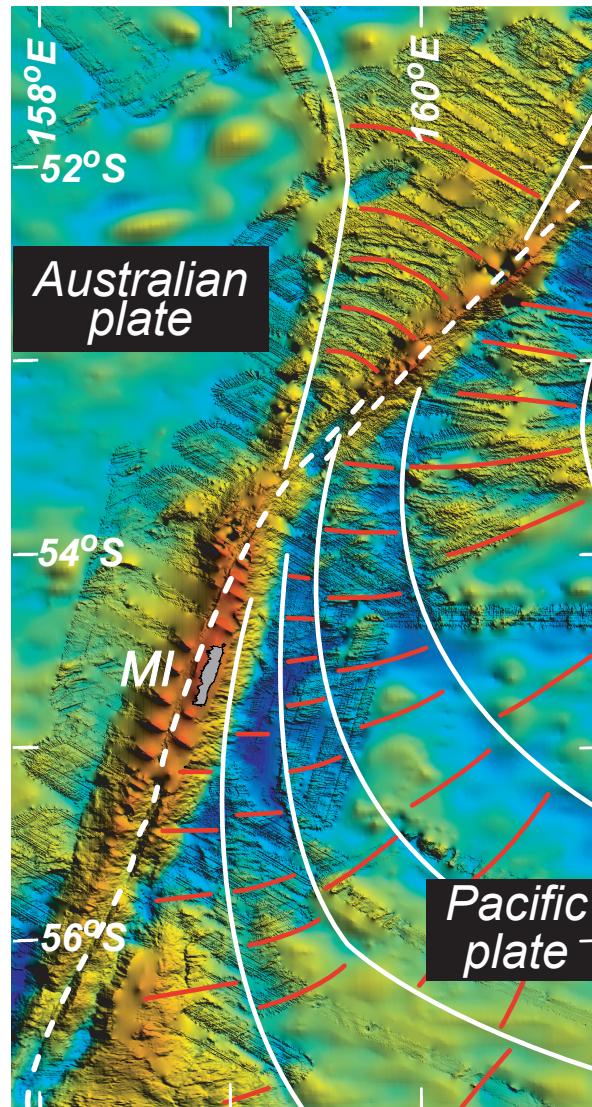


Figure 1.2. Bathymetry of the Macquarie Ridge Complex near Macquarie Island (Bernardel and Symonds, 2001) showing modern-day transform plate boundary (white dashed line). Fracture zones that formed at the Macquarie paleo-spreading center (black lines) become asymptotic approaching the plate boundary; spreading fabric is orthogonal (thin white lines). Macquarie Island (MI) is proximal to both the modern plate boundary (west) and two fracture zones (east). (Data from 1994 Rig Seismic, 1996 Maurice Ewing, and 2000 L'Atalante; rough areas, ship tracks; smooth, predicted bathymetry Smith and Sandwell, (1997)).

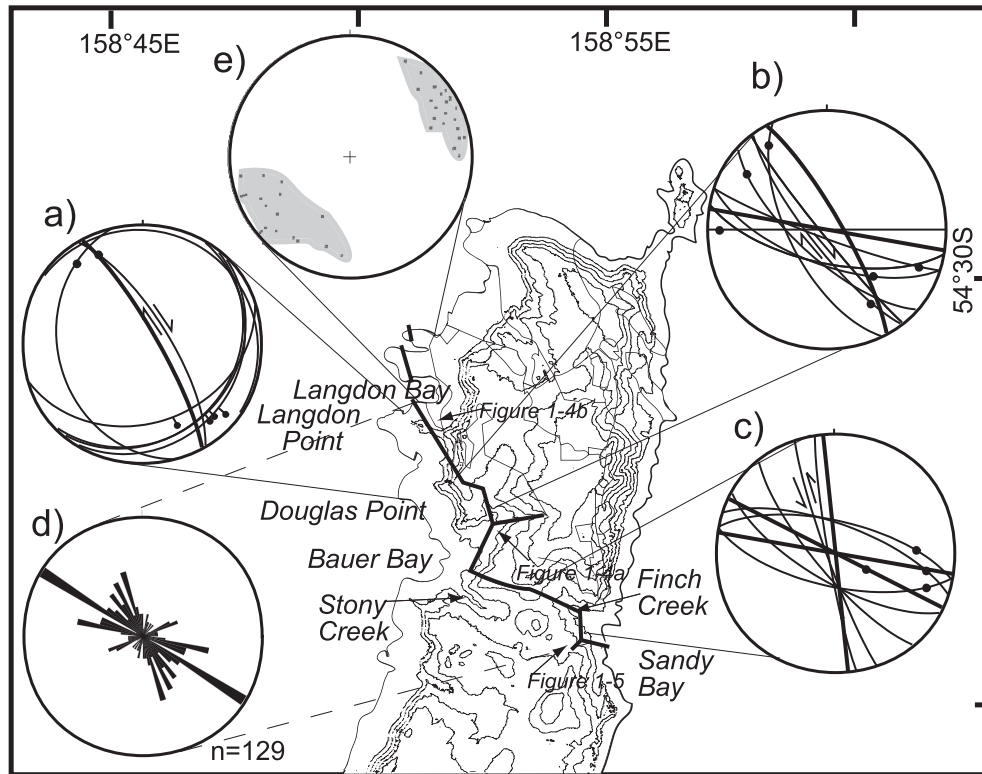


Figure 1.3. Finch-Langdon fault trace superimposed on topography. Note in Finch Creek, fault coincides with valley, whereas in Stony Creek, it does not. a-c) Stereograms (lower hemisphere, equal angle) show fault orientations, slickenlines (dot), and kinematics for three parts of Finch-Langdon fault zone. Trace of Finch-Langdon fault (Goscombe and Everard, 2001) in each region is plotted for comparison (bold lines; if no dip mapped, shown as  $90^\circ$ ). d) Rose diagram showing that strikes of dikes adjacent to fault zone are subparallel to segments of Finch-Langdon fault, dominantly striking northwest (largest petal represents 16 values, 12% of all values; strike direction  $5^\circ$  all classes). e) Stereograms (lower hemisphere, equal angle) show mylonite orientations, poles to planes shown, grey shaded areas define range of values.



Figure 1.4. The Finch-Langdon Fault at Bauer Bay, view to the NE (a) and at Langdon Bay, view to the SW (b). Locations of photographs are shown on Figure 1-3. The fault approximate location is marked by the black dashed lines. Arrowhead indicates fault continuation behind hills. In both locations the fault roughly coincides with topographic features, but does not form a clear fault scarp, indicating that the fault has not had recent motion.



Figure 1.5. The Finch-Langdon Fault at Finch Creek, view to south. Location of photograph is shown on Figure 1-3. The valley coincides with the fault, with pillow lava to the left, diabase dikes to the right. The valley scarps are marked by the black dashed lines. Note the dikes and pillows are at the same topographic level, indicating that the fault has not had recent movement.

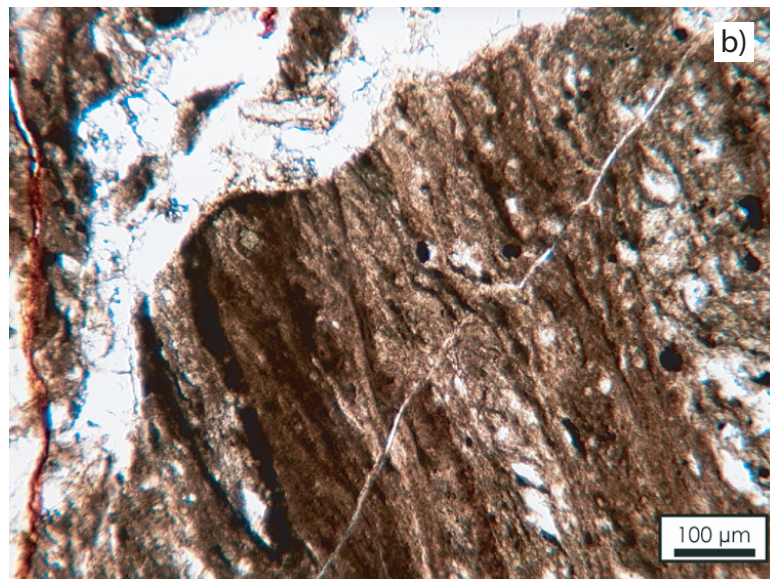
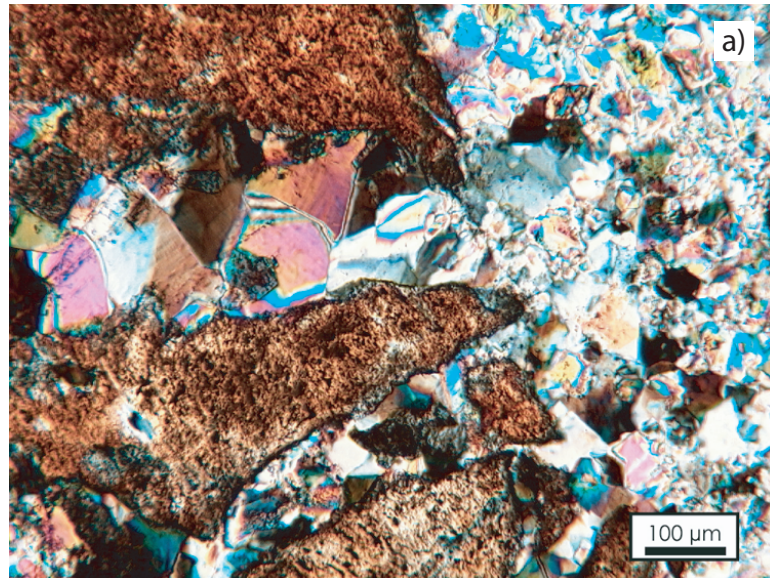


Figure 1.6. Photomicrographs of rocks sampled from the Finch-Langdon Fault zone confirming hydrothermal activity during faulting. a) Prehnite cemented fault breccia. Crossed polar light. b) Cataclastite with hydrothermal epidote within the sheared fabric, cut by a later prehnite vein. Plane polar light.



Figure 1.7. Sulfide alteration in the Finch-Langdon Fault zone a) Outcrop within the zone of rocks that have experienced sulfide alteration. On escarpment to the southeast of Bauer Bay hut, view to southeast. b) Photomicrograph of pillow basalt vesicle filled with pyrite. Sample from Bauer Creek. Reflected light. Sulfide alteration is common during hydrothermal discharge at mid-ocean spreading ridges.



Figure 1.8. Mineral-filled fractures in diabase dikes adjacent to the Finch-Langdon Fault in Bauer Creek. Different fracture sets are filled with combinations of prehnite, epidote, quartz and sulfides. Fractures decrease in concentration with distance from the fault.



Figure 1.9. Gabbro mylonites in the NE corner of Langdon Bay. a) Outcrop with steeply dipping mylonite zone. View to NE. b) Close-up view of same mylonite. Recrystallized material consists of pyroxene and plagioclase; also contains secondary amphibole and chlorite. All mylonite zones have NW strikes.



Figure 1.10. Sedimentary rocks interbedded with volcanics, indicating sedimentation during active volcanism. a) Red greywacke/mudstone between two basalt flows, near Mawson Point. Note radial cooling joints in lower flow, pillow shape and irregular basal surface in upper flow, view to S. b) Diabase dike that has intruded a talus breccia at Bauer Bay, view to S.



Figure 1.11. Talus breccia at Douglas Point that fines upward to greywacke and mudstone. Package is 4m thick, adult female elephant seals for scale (~500 kg, 2m long). View to NE. Inset: Clasts of diabase and gabbro indicate that these rocks were exposed on the seafloor.

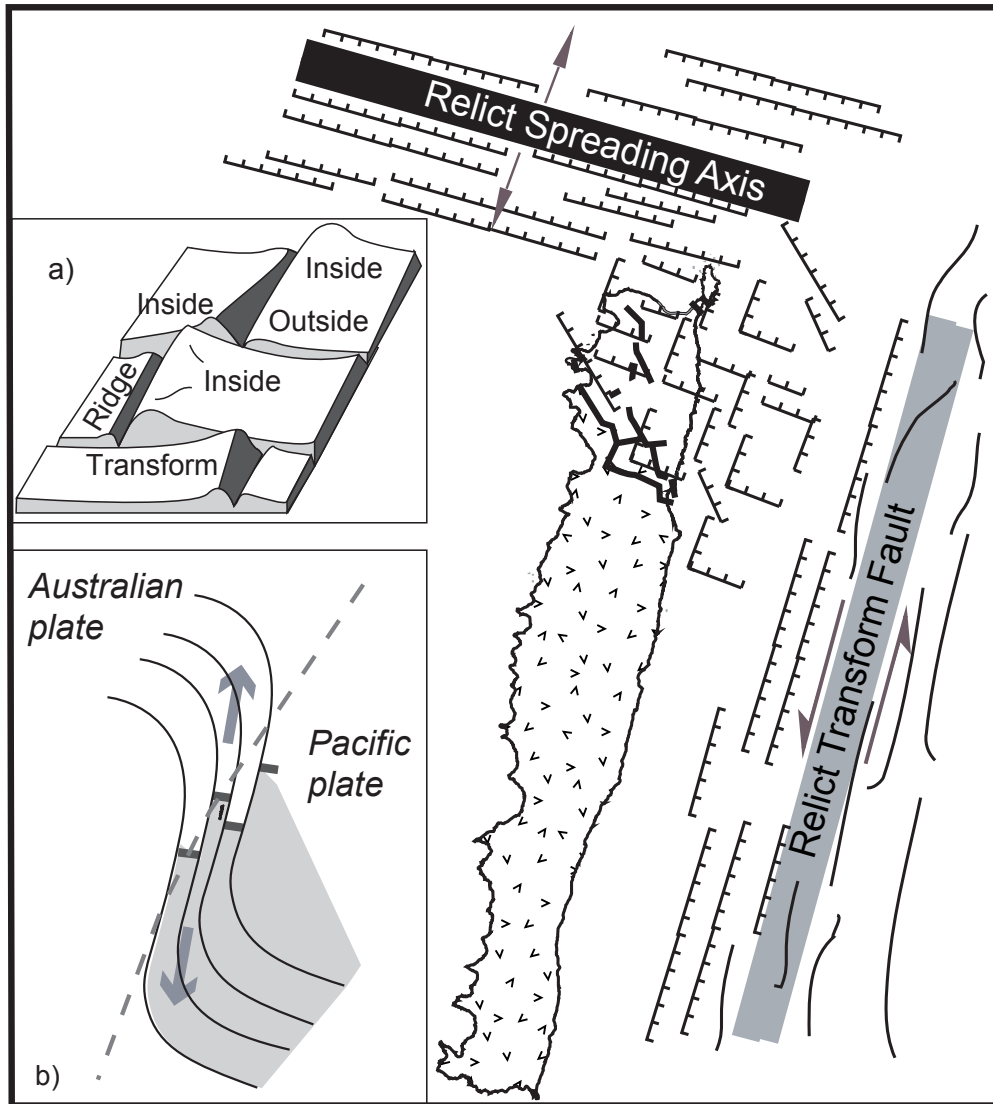


Figure 1.12. Proposed tectonic setting of Finch-Langdon fault: a ridge-transform intersection. Finch-Langdon and related faults shown. Inset A: Schematic geometry of RTI, after Tucholke and Lin (1994). Inside corners have a higher elevation (400-2500 m higher) than outside corners (Severinghaus and Macdonald, 1988). Inset B: Geometry of Australian-Pacific plate boundary at ca. 10 Ma when Macquarie Island crust formed (after Massell et al., 2000). Sigmoidal black lines-fracture zones; short, gray lines-spreading centers; dashed black line-present transform plate boundary; arrows-spreading direction.

## **Chapter 2: The melting history of Macquarie Island mantle peridotites and its relationship to seafloor spreading**

### **2.1 ABSTRACT**

Macquarie Island, located 1500 km southeast of southernmost Australia, is thought to be a complete section of slow- to intermediate-spreading ocean crust and upper mantle uplifted in the ocean basin in which it formed. However, the geochemical characteristics of mantle rocks from Macquarie Island are apparently at odds with this hypothesis. The levels of depletion indicated by the spinel Cr-number and Ti and Na contents of clinopyroxene of the Macquarie Island peridotites are more similar to those seen at fast spreading centers or ophiolites, not at slow spreading centers. Trace element analysis reveals spoon-shaped rare earth patterns (depletion of heavy rare earth and enrichment of light rare earth elements) in clinopyroxene as well as an anomalous enrichment of Sr. A spoon-shaped rare earth pattern and Sr anomaly are a common characteristic of ophiolites, not of abyssal peridotites. These two patterns may be caused by melting enhanced by the presence of fluids, as hypothesized for ophiolites, possibly introduced by an ancient subduction event no longer discernable in the seafloor rock record. It is also possible that these patterns may be unrelated to hydrous melting, and such peridotites may be absent from the seafloor because peridotites are only exposed in specific tectonic settings, resulting in a biased sampling of mantle peridotites. With future exploration or drilling of the seafloor, rocks of this type may be recovered.

## 2.2 INTRODUCTION

Abyssal peridotites sampled from the seafloor and peridotites studied in ophiolites are the residues of the melting and crystallization process that generates ocean crust; as such their geochemical patterns, modal mineralogy and petrology provide information about the production and transport of melts during the formation of two-thirds of the Earth's crust. As it is difficult to sample a complete section of ocean crust from the mantle through the extrusive series on the seafloor, ophiolites have played a critical role in our understanding of the structure and formation of oceanic lithosphere. However, most of the well-studied ophiolites are thought to be associated with subduction settings, rather than forming in a mid-oceanic environment, such as Oman (Searle and Cox, 1999), the Josephine (Harper, 1980), the Ingalls Complex (Metzger et al., 2002), the Bay of Islands (Suhr and Edwards, 2000), Troodos (Miyashiro, 1973). These ophiolites have been influenced both chemically and structurally by this subduction and later transport to continents (Buchan et al., 2001; Harper, 1984; Miyashiro, 1973). Therefore, it is difficult to find localities where 1) seafloor rocks are exposed on land, and 2) these rocks have been influenced by processes only related to the formation of crust on the ocean floor.

Macquarie Island is located between New Zealand and Antarctica on the Australian Pacific plate boundary, ~1500 km south of Australia. It consists of crust that was formed on a mid-ocean ridge and subsequently uplifted within the ocean basin in which it formed (Varne et al., 1969; Varne et al., 2000). Thus it is unique in that it should provide the sole opportunity to study a complete section of

ocean crust where both conditions given above are met. With this in mind, it follows that peridotites on Macquarie Island should be analogous to abyssal peridotites. This paper presents the results of a geochemical investigation of the Macquarie Island peridotites and compares them to abyssal peridotites and ophiolite peridotites.

### **2.2.1 Tectonic setting**

The tectonic setting of Macquarie Island has been described in detail elsewhere (Daczko et al., 2003; Goscombe and Everard, 2001; Varne et al., 2000). To summarize, Macquarie Island is the apex of the Macquarie Ridge Complex, a series of bathymetric highs and lows that lie along the modern Australian-Pacific plate boundary (Figure 2.1a). The crust in the Macquarie region formed on the Macquarie paleo-spreading ridge that was active between ~40 and 6 Ma with the rocks of the island forming during the final stages of spreading before magmatism ended (Cande et al., 2000; Massell et al., 2000; Wood et al., 1996). Slow spreading rates (2-3cm/yr full rate; Wood et al., 1996) have been calculated from published magnetic anomalies (anomalies 18 to 12) in the seafloor in the Macquarie region on the Australian plate, although recently acquired magnetic anomaly data on both the Pacific and Australian plates (anomalies 18 to 9) yield somewhat higher rates in the slow to intermediate spreading range (T. Meckel, C. G. Massell and W.R. Keller pers. comm.). No data exists to constrain the spreading rate as spreading shut down, but estimates for the cessation of spreading using the same spreading rates yields ages equivalent to those for basalts on Macquarie Island (11.5 to 6 Ma; Duncan and Varne, 1988; our

preliminary data), suggesting that slow to intermediate rates continued (T. Meckel, C. G. Massell, pers. comm..). Transpression along the plate boundary has uplifted the island essentially intact, and although the island is cut by numerous brittle uplift-related faults (Daczko et al., 2003; Goscombe and Everard, 2001; Wertz et al., 2000b), many structures that formed on the seafloor, including spreading-related faults (Daczko et al., 2003; Goscombe and Everard, 2001; Wertz et al., 2000b) and intact volcanic eruptive centers (Goscombe and Everard, 1998), have been preserved, attesting to the undisrupted submarine nature of the crust.

All levels of oceanic lithosphere are found on the island, including an extrusive section (pillow basalt, massive basalt flows, and rare sedimentary rocks), an intrusive section (sheeted diabase dikes and gabbroic rocks) and residual mantle peridotites (Figure 2.2). Basalts on the island are E-MORBs ( $(\text{La}/\text{Sm})_N > 1$ ,  $N = \text{chondrite normalized}$ , see chapter 3; Niu et al., 2001), with a wide range of chemical compositions (Kamenetsky, 2000; Kamenetsky and Maas, 2002). The intrusive/mantle section in the northern part of the island was exposed on the seafloor as a result of motion on a major fault active during seafloor spreading, the Finch-Langdon fault (Wertz et al., 2000a; chapter 1, Figure 2.2). Additional erosion occurred as the island breached the sea surface, as evidenced by wave-cut platforms and raised beach deposits (Selkirk et al., 1990).

## **2.3 METHODS**

### **2.3.1 Field study**

Two primary sections of mantle rocks are exposed on Macquarie Island, one along the west coast and a second on the eastern plateau (Figure 2.2, 2.3a, 2.3b.) The western section has 100% exposure in places and is found along a coastal strip 1.5km long. The eastern section forms more sporadic outcrops, found over an approximately 2 km<sup>2</sup> area. The two areas are separated by nearly 2 km<sup>2</sup> of virtually no outcrop. Residual harzburgite samples were collected in both sections at ~100 m intervals; sample sites were marked with a GPS unit with up to 3 m accuracy. The structural level of the mantle section is indeterminate, and the petrologic Moho has not been identified by this or other studies. However, as the peridotites are in close proximity to and intruded by gabbroic and doleritic rocks, they are likely to represent the upper levels of the mantle. Cross-cutting gabbro and diabase dikes were observed in outcrop, and care was taken in sampling to avoid these late features. With each peridotite sample, the distance between it and the nearest gabbro or diabase body was noted. Although rare dunite has been mapped on the island (Goscombe and Everard, 2001), none was found in the sampled sections. This paucity of dunite could be caused by preferential erosion of dunite over harzburgite reducing the amount of exposed dunite, but it is unlikely that there were ever large volumes of dunite within the mantle section.

All samples exhibit alteration similar to that seen in abyssal peridotites. All are over 95% serpentinized, but relict textures are preserved. The samples are homogeneous, orthopyroxene-porphycroclastic harzburgites, devoid of

plagioclase and microscopic magmatic dikelets. Olivine is preserved in one sample, as irregular patches up to 400 $\mu\text{m}$  in diameter surrounded by a network of serpentine. Relict irregular, lobate orthopyroxene (opx) grains are 3mm to 1cm, with fresh cores that are up to 2mm. Some cores are composed of clusters of fresh opx, each 100-200 $\mu\text{m}$ . Clinopyroxene (cpx) occurs in orthopyroxene porphyroclasts as fine exsolution lamellae and exsolution blebs between 50-300 $\mu\text{m}$ , symplectites with spinel, and as small (50-200 $\mu\text{m}$ ) interstitial grains along boundaries of larger opx. Spinel is brown to dark red-brown in color and occurs as isolated subhedral grains or as symplectites with cpx or opx. Grains range from 50  $\mu\text{m}$ -6mm, and symplectites are up to 3mm in length, with arms up to 200 $\mu\text{m}$  thick.

Fresh spinels, opx, cpx and clinopyroxene exsolutions (cpx-xs) were selected for analyses. All analyzed domains are optically clear and bear no evidence of alteration. Of the 25 samples collected, all contained fresh spinels, 13 contained fresh opx, and 11 contained fresh cpx.

### **2.3.2 Laboratory techniques**

Major elements were analyzed using the five-spectrometer JEOL JXA 8900RL electron probe microanalyser at the University of Mainz using an acceleration potential of 20kV, a beam current of 20nA and a spot size of 2 $\mu\text{m}$  for spinels. The acceleration potential was reduced to 15kV and 12nA for cpx and opx analyses. Trace elements in cpx were measured using the Cameca IMS-3f at the Max-Planck Institut für Chemie in Mainz following detailed petrographic and major element analyses. Trace element concentrations were determined by

energy filtering techniques of Shimizu and Hart (1982) using a 25eV energy window and a -80V energy offset from a 4500V secondary accelerating potential. Negative oxygen ions were used as a primary source with an accelerating potential of 12.5kV and a 6nA beam current, resulting in a spot size of <20 $\mu$ m. The overall accuracy and precision is better than 20 % for the REE and better than 12 % for the other trace elements (2 sigma). More detailed analytical procedures are reported in Hellebrand et al. (2002).

## **2.4 RESULTS**

### **2.4.1 Mineral compositions**

Major element data for spinels are presented in table 2.1, major element data for opx are presented in table 2.2, and major and trace element data for cpx are presented in table 2.3a and 2.3b. Spinel is relatively depleted in Al, with Cr-numbers (= molar Cr/(Cr+Al)) ranging from 0.39 to 0.48 (n = 25, Table 2.1, Figure 2.4). Average Al<sub>2</sub>O<sub>3</sub> in opx porphyroclast cores is also low, ranging from 2.05-2.99 wt % (Table 2.2, Figure 2.5). Opx Mg-numbers range from 0.91-0.93 (Table 2.2, Figure 2.5). Na<sub>2</sub>O contents are low, 0.08-0.12 wt % (Table 2.2).

Both cpx porphyroclasts and cpx exsolutions within opx were measured; in one sample that had both porphyroclasts and exsolutions the compositions were identical. This equivalence was extrapolated to analyses of samples with exsolutions but no porphyroclasts; it was assumed that exsolutions reflected the original compositions of altered cpx porphyroclasts. Clinopyroxene TiO<sub>2</sub> contents are extremely low (0.00 – 0.07 wt% TiO<sub>2</sub>, Table 2.3). Sodium contents are variable; eight samples are very low, ranging from 0.02 – 0.08 wt% Na<sub>2</sub>O,

whereas five other others with similar interstitial cpx textures have significantly higher values (0.11 – 0.27 wt% Na<sub>2</sub>O). Mg-numbers are homogeneously high (0.94, Table 2.3).

Cpx trace element analysis revealed a uniform depletion of HREE and variable enrichment of LREE (see section 2.4.2 for discussion, Figure 2.6a, 2.6b, normalized to chondrite), and in some samples a positive Sr anomaly (Figure 2.6c). REE and trace elements in cpx (Figure 2.6a-2.6d) for the east and west sections have been plotted separately for clarity, as there is very limited exposure in the ~2km<sup>2</sup> between the two sections. In the western section, there is a general trend of increasing LREE enrichment to the south. All eastern samples are similarly enriched. Four western samples have a strong positive strontium anomaly. Although all samples with this anomaly are in the west, the southernmost sample from the western section (LB25b, Figure 2.3a) has a trace element pattern that is similar to the eastern section samples with no strontium anomaly; because of this, both sections are treated as the same unit.

## **2.5 DISCUSSION**

### **2.5.1 Comparison with other peridotites: ophiolite or ocean crust?**

Macquarie Island peridotites, which represent oceanic mantle rocks uplifted in situ, show some chemical similarities to abyssal peridotites, but more with ophiolites. Spinel Cr-numbers in the Macquarie Island peridotites (0.39 to 0.48, Table 2.1, Figure 2.4) correspond to 15-16% fractional melting (Hellebrand et al., 2001). In addition, TiO<sub>2</sub> contents in spinel are low (0.02-0.1), attesting to the residual nature of Macquarie Island peridotites (Seyler and Bonatti, 1997)

(Figure 2.4). The Cr-numbers, however, are higher than most abyssal peridotites, which are almost uniformly taken from slow to intermediate spreading ridges (Figure 2.4). The exception is peridotites exposed at Hess Deep, with higher Cr-numbers, that were generated at the fast spreading East Pacific Rise (EPR). Note: this is the only place where fast-spread abyssal peridotites have been sampled, as they have been exposed by rifting caused by propagation of the Galapagos Ridge into older EPR crust. Usually, at fast spreading ridges, extension is accommodated by high volumes of magmatism and not by detachment faulting required to expose mantle and lower crust rocks. The low  $\text{Al}_2\text{O}_3$  and high Mg-numbers (0.92 on average, Table 2.2) in opx also suggest a degree of melting that is higher than for most abyssal peridotites, although the Macquarie Island samples do generally fall on the linear trend exhibited by abyssal peridotites, but filling in a gap where few others fall (Figure 2.5).

The depletion in HREEs and enrichment in LREEs, producing "spoon-shaped" REE patterns in clinopyroxene (normalized to chondrite) (Figure 2.6) is common in ophiolites, (e.g., Bodinier et al., 1990; Büchl et al., 2002; Godard et al., 1995) but is unknown in abyssal peridotites. Figure 2.6 shows a comparison of Macquarie Island and abyssal peridotite clinopyroxene data normalized to chondrite. Abyssal peridotites are typically more depleted in LREE, producing a REE pattern that is concave downward and/or sloping down toward the LREE, thus if LREE show a concave upward pattern they are enriched in LREE. Alternatively, cpx in abyssal peridotites show a flat pattern, evenly depleted in REE, which is characteristic of fertile, un-depleted lherzolites. Despite variable

LREE enrichment, Macquarie Island cpx HREEs, when plotted with abyssal peridotite on a graph of Yb in cpx vs. Cr-numbers in spinel, fall within a linear trend shown by abyssal peridotites, again filling in a gap where no abyssal data has yet been measured (Figure 2.7).

Major element and moderately incompatible trace element characteristics of the Macquarie Island peridotites are similar to abyssal peridotites, but also distinct as indicated above (Figures 2.4, 2.5, 2.7). However, there is a significant difference between the highly incompatible elements (La, Ce, Sr) in the Macquarie Island peridotites and in those sampled from the seafloor. In Figure 2.8, the ratio of the highly incompatible element Ce over the slightly less incompatible Nd is plotted against Yb for Macquarie Island, abyssal peridotites and ophiolites. The ophiolite peridotites included are from Oman, the Horoman, Troodos, Bulquiza-Tropoja (Albania) and Pindos (Greece), and all show a range of Ce/Nd values and low Yb concentrations. A clear difference exists between Macquarie Island and abyssal peridotites, with Macquarie Island cpx possessing higher Ce/Nd at a given Yb concentration. The very few abyssal peridotites that have similar values to some of the Macquarie Island samples (Fig. 2.8) come from the ultra-slow spreading Gakkel ridge (Hellebrand, unpub. data). In addition, for Macquarie Island cpx, Sr/Sr\* (Sr\* = geometric mean of Ce and Nd, indicating an anomalous enrichment of Sr if this ratio is significantly greater than 1) plotted against Yb fall into two groups, those that have a pronounced positive Sr anomaly (four samples from the western section) and those that do not (Figure 2.8).

Thus although Macquarie Island peridotites show many similarities to abyssal peridotites, they have characteristics that are dissimilar, such as their Cr-numbers, spoon-shaped rare earth patterns and positive Sr-anomalies. These geochemical traits are more similar to ophiolite peridotites. In the following sections I discuss the larger implications of these results.

### **2.5.2 Relationship of degree of melting to spreading rate**

The mineral chemistry of relict phases in abyssal peridotites is profoundly affected by the process of melt generation. For example, Dick and Bullen (1984) found that Cr-numbers in spinel are sensitive qualitative indicators of mantle melting, providing information about the activity of Al in the system. The silicate phases are similarly affected. Trace element compositions of clinopyroxenes are another very useful tool for studying mantle partial melting (Johnson et al., 1990) and show that in most cases, mid-ocean ridge melting is nearly fractional (melts are almost completely removed from the source area as they are produced). Hellebrand et al (2001) were able to connect the two and show a consistent melting behavior for both major and moderately incompatible trace elements, providing a quantitative method of determining the degree of melting using Cr-number in spinel.

Although many factors affect the degree of mantle melting, such as the depth of melting and the presence or absence of fluids, it has been proposed that a major control of the degree of melting as recorded in residual peridotites, is the spreading rate of a ridge (Niu and Hekinian, 1997). Thus peridotites that have been melted in a fast-spreading regime will be more depleted in basaltic

components (e.g., major elements like Ca, Al, Ti) than those melted during slow spreading. For example, Cr-numbers from spinels in peridotites formed on the East Pacific Rise (EPR) and exposed at Hess Deep are high (0.54), and the spreading rate is fast (135 mm/yr, full rate). Nearly all other abyssal peridotites have lower Cr-numbers (Figure 2.4) and are almost uniformly taken from slow to intermediate spreading ridges. Although high Cr-number spinels sporadically occur in peridotites from slower spreading ridges (e.g., Hellebrand and Snow, in press), peridotites from the fast-spreading EPR are the only known melting residues which contain such a uniform depletion.

Macquarie Island is generally considered to be a slow spreading ridge ophiolite (Varne et al., 2000; Wood et al., 1996), though recently determined magnetic anomalies indicate slow to intermediate spreading rates (T. Meckel, C. G. Massell and W.R. Keller pers. comm.). In either case, assuming that the rate of spreading did not increase from ~30 to 6 Ma as spreading ceased (as supported by the similarity in the predicted timing of magma cessation and ages for Macquarie Island basalts), the peridotites should therefore be residues of relatively low degree of melting, compatible with major and trace element compositions of Macquarie Island basalts (Kamenetsky, 2000; Kamenetsky and Maas, 2002; Wertz et al., in prep, chapter 3). This assumption is supported by the presence of uplifted mantle, which is not associated with fast spreading ridges. The uniformly depleted character of the Macquarie Island peridotites is not, however, consistent with a slow to intermediate spreading tectonic setting. Thus, either spreading rate must have increased significantly during the last stages of spreading, which is

unlikely, or another explanation for either a high degree of melting (15-16% fractional melting; Hellebrand et al., 2001), high Cr-numbers and/or HREE depletion is needed.

Although the Macquarie Island peridotites have some geochemical similarities to Hess Deep peridotites (in particular depletion that indicates that they produced normal, ~6 km thick crust), they are clearly distinct from them. The Macquarie opx Mg-numbers are higher at similar Al contents (Figure 2.5), and the HREE of the Macquarie Island cpx are more fractionated at slightly lower spinel Cr-numbers (Figures 2.7). Qualitatively, this fractionation suggests that the Macquarie Island peridotites are dominated by near-fractional melt extraction. As will be discussed below, the LREE enrichment is not a residual signature but must be imposed by a percolating fluid and/or melt. Hess Deep peridotites are more dominated by batch melting (as opposed to fractional melting) and melt-percolation (Hellebrand and Snow, pers. comm.) whereby melts remain within the peridotites and equilibrate with residual phases, as indicated by their flatter REE pattern. The percolating melts were depleted in moderately incompatible elements such as the HREE and Al (Figures 2.7, 2.5, respectively), but they cannot represent depleted instantaneous melt increments of a residual melting column (Hellebrand and Snow, pers. com.). Instead the mantle at Hess Deep must have been infiltrated by a minor LREE-bearing component, which had probably aggregated and equilibrated with the locally derived melts generated during the reactive percolation. Therefore the Hess Deep melt most likely was a pooled

MORB-type liquid, diluted by the addition of the depleted peridotite-derived melt through which the exotic melt percolated (Hellebrand and Snow, pers. com.).

It is likely that the global abyssal peridotite database provides a distorted relationship between the extent of depletion of moderately incompatible elements and the spreading rate (Hellebrand et al., 2002b). Most peridotites from slow spreading ridges were collected at fracture zones and non-transform discontinuities. Depleted peridotites from fast spreading ridges are only found in special tectonic settings, such as Hess Deep (Dick and Natland, 1996) where ridge propagation has cut a deep canyon through the crust formed at the fast-spread East Pacific Rise. Elsewhere at fast spreading ridges, extension is primarily accommodated by volcanism rather than detachment faulting that exposes the deep rocks. In the past decade, a number of combined geophysical-petrological studies have shown that slow spreading ridges show along-ridge segmentation (Cannat and Seyler, 1995; Gente et al., 1995; Lin et al., 1990). In segment centers, melt supply is high and a normal magmatic crust is formed with only basalts exposed. At segment ends, melt supply is low with periodic magmatism, seismic velocities indicate that the crust is thin, and upper mantle lithologies are often exposed (Cannat et al., 1997; Gente et al., 1995). The collected peridotites are relatively fertile, supporting a low degree of melting at these locations (Ghose et al., 1996). The peridotites associated with normal, thick (~6 km) crust, however, are sampled only rarely, as they are not normally exposed, but it is very likely that the mantle in the segment centers at slow spreading ridges is similarly depleted as the mantle exposed at Hess Deep (Hellebrand pers. com.). The main difference

between slow and fast spreading would therefore be the temporally and spatially continuous melt generation at fast spreading ridges versus the spatial and temporal heterogeneity at slow spreading ridges. If only peridotites away from fracture zones are considered, the spreading rate dependence of the degree of melting may not exist except for ultra-slow spreading ridges (Hellebrand et al., 2002b; Reid and Jackson, 1981). This being said, however, recent preliminary results from ODP Leg 209 indicate that extremely depleted peridotites need not be restricted to fast-spread ridges, or even slow-spread ridge centers. Drilling of the 15°20' Fracture zone ridge-transform intersection has recovered depleted peridotites, which would not be predicted with the models described above. No analyses have been made available, and the preliminary report only mentions the depleted peridotites in a very general sense, but if further analyses do indicate a high degree of melting at the transform intersection the above argument is moot.

For Macquarie Island, marine geophysical data documents a transform ~7 km to the east of the island (Fig. 1.3), indicating that these peridotites formed near a transform ridge intersection. Furthermore, the uplift of these rocks to the ocean floor synchronous with spreading related volcanism (Wertz et al., 2000a; chapter 1) is compatible with their uplift in an inside corner high of a ridge-transform intersection. Spreading rates, as discussed previously, are most likely in the slow to intermediate range. Thus, Macquarie Island peridotites should be similar to most abyssal peridotites in the presently available database. The very preliminary results from ODP Leg 209, plus the geochemistry presented herein for Macquarie Island that should represent abyssal peridotite uplifted in situ, suggest that the

existing database may be biased. Further sampling of these tectonic windows may require a reevaluation of generally accepted the models discussed above.

### **2.5.3 Trace element enrichment: Macquarie Island, abyssal peridotites and ophiolites**

#### ***2.5.3.1 Spoon-shaped REE patterns***

Relative enrichment of La and Ce in otherwise depleted cpx define the “spoon shaped” REE patterns (Figure 2.6). These anomalies are unknown in abyssal peridotites, but have been reported in many studies on mantle rocks from ophiolites and orogenic lherzolite bodies (Bodinier et al., 1990; Büchl et al., 2002; Godard et al., 1995). Enrichment of the highly incompatible LREEs is thought to be caused by a melting reaction between residual peridotite and a percolating enriched melt or enriched fluids (Bodinier et al., 1990; Navon and Stolper, 1987; Sen et al., 1993; Takazawa et al., 1996). Although the former seems likely to occur in any setting where melting of the mantle is occurring, the latter is generally believed to be a subduction related phenomenon caused by the presence of slab-derived fluids during melting, and this type of spoon-shaped pattern has only been reported in ophiolite peridotites (e.g., Bizimis et al., 2000; Büchl et al., 2002; Godard et al., 1995; Gruau et al., 1998; Miller et al., 2003) and in some peridotite xenoliths associated with mantle plumes (Lenoir et al., 2000; Sen et al., 1993). Abyssal peridotites generally do not show this pattern, indicating that they are residues of near-fractional melting and implying that abyssal peridotites do not record the hydrous melting common in most ophiolite mantle sequences. In addition, in abyssal peridotites, melts are believed to be transported via discrete

channels, limiting interaction between the melts and the residues through which the melts pass (Hart, 1993; Hellebrand et al., 2002a; Johnson et al., 1990; Kelemen et al., 1997).

### ***2.5.3.2 Positive Strontium anomalies***

Abyssal peridotites are not known to possess pronounced strontium anomalies as shown in Figure 2.8. A slight negative Sr anomaly is associated with fertile (cpx rich, Yb ~10x chondrite) abyssal peridotites, which gradually becomes positive with decreasing Yb contents (an indicator of increased degree of partial melting). However, these positive anomalies do not approach the higher values measured in ophiolites and the Macquarie Island peridotites.

Commonly, Sr anomalies are associated with the presence or involvement of plagioclase during the melting process. Cpx in plagioclase-bearing peridotites always have negative Sr anomalies (Sen et al., 2003; Seyler and Bonatti, 1997; Takazawa et al., 1996; von der Handt et al., 2002) whereas resorption of cumulate plagioclase can cause positive Sr anomalies. However, positive Sr anomalies are also seen in plagioclase-free peridotites, which, under magmatic conditions can be caused by 1) fertilization of cpx via interaction with a melt that has resorbed plagioclase elsewhere, 2) Sr enrichments in the source 3) later low-temperature alteration or 4) Sr enrichment during hydrous partial melting. Below I consider each of these possibilities.

In the first case, Macquarie Island cpx may be enriched in Sr by a percolating melt that has dissolved plagioclase during ascent. However, the bulk rock and cpx will also have high Al contents, resulting in low Cr-numbers. The

Macquarie Island samples have high Cr-numbers. In the second case, it is possible that the source rock has an anomalous enrichment in Sr; however, no such source has ever been reported elsewhere. It is clear that the Sr anomaly observed in the Macquarie Island samples was not caused by alteration because all of the samples had alteration identical to that seen in abyssal peridotites, yet a positive Sr anomaly of this magnitude has not been seen in any other abyssal peridotite with similar alteration. In addition, both matrix and exsolved cpx have identical trace element compositions (BH17, Figure 2.5). If the LREE and Sr enrichment was a late stage metasomatic phenomenon, a grain-scale enrichment gradient would be expected, with higher enrichment in the matrix cpx than in the exsolved cpx within the protected opx cores (Van Orman et al., 2001).

The last possibility is the most likely. Both positive Sr anomalies and spoon-shaped REE patterns can be caused by enrichment during hydrous partial melting (Gruau et al., 1998). The presence of fluids during melting affects the melting process in two ways, by enhancing melting and by carrying fluid-mobile elements that can be taken up by the minerals left in the source. The end result is higher degrees of melting, coupled with enrichments of fluid-mobile, highly incompatible elements, such as strontium. This scenario is compatible with the high Cr-numbers and REE patterns of LREE enrichment and HREE depletion, coupled with a positive Sr anomaly seen in the Macquarie Island peridotites. To explain the preferential Sr enrichment in four out of seven samples, it is possible that because Sr is slightly more fluid-mobile than the LREEs (Polat et al., 2003), enrichment of Sr will occur before the LREE enrichment, although both Sr and

LREEs are present in the fluid. In Macquarie Island samples with the Sr anomaly, Sr in cpx may have already reached equilibrium with fluid-enriched melt, while the LREEs have not mobilized into cpx yet. In the samples without a Sr anomaly, both Sr and the LREEs have equilibrated in cpx, creating the overall enrichment of both Sr and LREEs. The samples that do not have a positive Sr anomaly have higher overall LREE and highly incompatible trace element enrichment concentrations.

If a different fluid-mobility of Sr and the LREE is responsible for the Sr-enrichment in some of the studied peridotites, then significant sodium enrichments are expected as well, because this element is even more fluid-mobile than Sr. The apparently fluid-influenced Macquarie Island peridotites, however, record extreme Na<sub>2</sub>O depletion (Tables 2.2 and 2.3). The behavior of sodium in abyssal peridotites is poorly understood, because it is commonly anomalously enriched in many LREE-depleted abyssal peridotites. This decoupling of Na and the LREE suggests that sodic metasomatism is not restricted to the subcontinental mantle, but can also occur in the oceanic lithosphere (Hellebrand and Snow, in press). Therefore, this observation is in apparent contrast with the lack of Na enrichment in the Macquarie Island samples.

In summary, the Macquarie Island peridotites, with their enrichment of Sr and LREE and high degree of melting, are more akin to ophiolitic peridotites and not abyssal peridotites, contrary to expectations derived from the tectonic setting of the island.

#### **2.5.4 Alternative models for Macquarie Island geochemistry**

Emplacement of oceanic crust on the continent (obduction) is the process by which an ophiolite is created (Wakabayashi and Dilek, 2001) and is the key difference between an ophiolite and ocean crust. This emplacement occurs during collisional tectonics, when a sliver of ocean crust is thrust onto a continent or onto a subduction complex that is then transferred to a continent. In contrast, Macquarie Island is a directly uplifted section of ocean crust, and therefore not, by definition, an ophiolite. It has not been thrust over another tectonic plate, but has been simply been uplifted by broad flexure of the plate boundary region, and perhaps block faulting, during transpression (Daczko et al., 2003; Meckel, 2003; Meckel et al., in press). Therefore its geochemistry should not have been affected by processes related to uplift. It is this history that makes Macquarie Island unique as the sole locality where seafloor unaffected by interaction with subduction zones, continental obduction, or mantle plumes (e.g., Iceland) can be studied without having to work under water. However, in spite of this tectonic history, the geochemical characteristics of Macquarie Island peridotites do not resemble those of abyssal peridotites, but instead resemble ophiolites. Additionally, major elements in spinel and pyroxene revealed high degrees of melting similar to those seen in abyssal peridotites at fast spreading ridges (i.e., the EPR at Hess Deep), which does not fit with the tectonic model for the evolution of the Australian-Pacific plate boundary. Not only are the spreading rates recorded by the magnetic anomalies in the surrounding seafloor in the slow to intermediate range, it is highly unlikely that the rates were fast causing a high

degree of melting just prior to cessation of magmatism, as discussed previously. Below I explore other tectonic models and evaluate whether they could produce the geochemistry of the Macquarie Island peridotites.

One possible explanation for the higher degree of melting that would fit with the tectonic situations, is that the constantly changing spreading direction, during the transition to transform motion, lead to the repeated melting of the same mantle source (Figure 2.9). Nonetheless, melting alone cannot produce the enrichment of LREEs and strontium seen in the Macquarie Island peridotites. In this scenario, fluids might be introduced along the fracture zones and very short spreading segments, although hydrothermal circulation is not thought to penetrate deeply enough to interact with melting.

Melting under hydrous conditions appears to be the only explanation for generating the observed trace element patterns (and Sr enrichment in some samples). Generally, enriched fluids are thought to be introduced during subduction, with dewatering of the subducted slab facilitating melting (Peacock, 1990). However, in the vicinity of Macquarie Island, there is no geophysical evidence to suggest that subduction occurred at any point during the >40 million year history of spreading and transpression along the Australian-Pacific Plate boundary.

We cannot eliminate the possibility that the geochemical signature in the peridotites is the result of an ancient subduction event that contaminated the mantle (e.g., Moores, 2000) and for which the surface evidence of this occurring has subsequently been erased from the rock record. Some plate reconstructions

have indicated that subduction occurred in the vicinity ~96 Ma, which moved eastward (Li and Powell, 2001) (Figure 2.10). This subduction may have abandoned a slab which would have contaminated the mantle, providing the hydrous melting signature of the Macquarie Island peridotites. But this requires the contaminated mantle signature to persist for 90 Ma, through >40 Ma of rifting of the paleo-Macquarie spreading ridge, which may be unlikely. A second possibility is that subduction occurred along the curving fracture zones when they were put under compression during transpression (Figure 2.11). However, excellent sidescan, bathymetric, and gravity data (Massell et al., 2000; Meckel, 2003; Meckel et al., in press) show no evidence of even incipient subduction along these curved fracture zones, let alone enough underthrusting to result in melting (i.e., no topographic expression, deformation of the seafloor structures, or remnant of subduction-related magmatism).

Another possible cause for this signature may be melting caused by rifting of crust and lithospheric mantle that has been pervasively altered along a transform. A hypothetical transform has been suggested to have acted as a preexisting weakness causing the localization of rifting as the plate motions changed (Wood et al., 1996), perhaps enabling the rifting that began on the paleo-Australia-Pacific plate boundary. In addition, plate reconstructions of Marks and Stock (1997) for 60 Ma show the Southeast Indian Ridge propagating toward the Tasman Ridge, with the two ridges offset by a transform that is thought to be future MRC (Figure 2.12). However, if alteration along this preexisting transform that was subsequently rifted is the cause of this signature, then again, the hydrated

lithospheric mantle would need to remain as the source through many tens of millions of years of magmatism, which does not seem likely.

In summary, the well-constrained tectonic setting of Macquarie Island is not easily compatible with scenarios discussed above and/or those typically invoked to explain these geochemical patterns usually observed in ophiolites, suggesting that the factors that contribute to ophiolite-style peridotite geochemistry may be more complicated than previously thought.

## **2.6 CONCLUSIONS**

Macquarie Island peridotites, rocks that represent oceanic peridotites uplifted in situ, are similar but distinct from abyssal peridotites. The peridotites are uniformly depleted harzburgites with low modal cpx, high spinel Cr-numbers close to 0.5 and low HREE contents in cpx. Geochemically, the depletion indicates a high degree of melting that is more similar to depleted residual mantle rocks from the fast spreading EPR exposed at Hess Deep, than mantle rocks exposed at slow-to intermediate- spreading ridges similar to the paleo-Macquarie spreading center.

All Macquarie Island peridotites have LREE-enriched cpx and some samples have a pronounced positive Sr anomaly. Such chemical signatures are not found in any abyssal peridotite, but have been reported in mantle sections of ophiolites. This similarity suggests that these fluid-mobile elements may have been contributed to the Macquarie Island peridotites through contamination by ancient subduction.

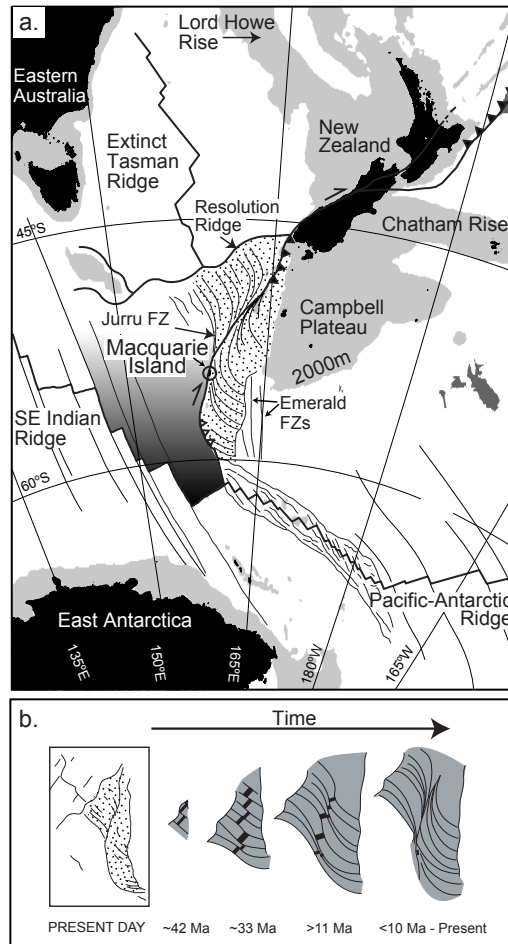


Figure 2.1. a) location map of Macquarie Island and the Australian-Pacific transform plate boundary (after Daczko et al., 2003). Crust formed by Australian-Pacific spreading along the Macquarie spreading ridge between  $\sim 40$  and  $\sim 10$  Ma is stippled. Gradient shaded crust is the Macquarie plate that formed and began moving independently of the rest of the Australian plate at  $\sim 6$  Ma (Cande and Stock, in review.) Filled triangles along the plate boundary are subduction zones; open triangles in the Hjort region represent incipient subduction (Meckel et al., in review). Light gray illustrates regions of seafloor shallower than 2000 m. Past and present plate boundaries are shown as thick black lines. Fracture zones (FZ) are shown as thin black lines. Azimuthal equidistant projection centered at  $60^{\circ}\text{S}$ ,  $180^{\circ}\text{E}$ . b) Between  $\sim 42$  and  $<10$  Ma, the Macquarie spreading became increasingly oblique as the spreading ridge rotated, with volcanism ceasing at  $= 6$  Ma. The rocks of Macquarie Island formed at the end of spreading, with the MRC and the island uplifted via transpression after the cessation of spreading.

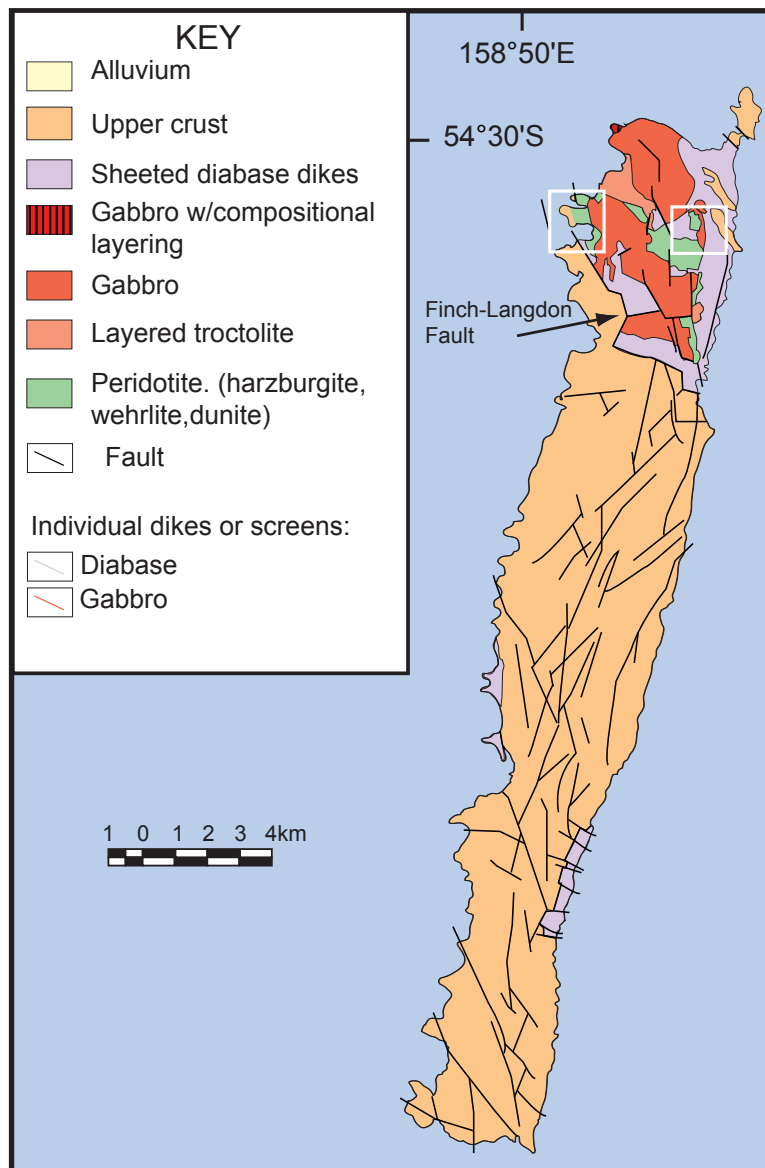


Figure 2.2. Geologic map of Macquarie Island (Goscombe and Everard, 2001). All levels of ocean crust are represented. Upper crust includes pillow basalt, massive basalt flows, hyaloclastite and rare sedimentary rock. Lower crust and upper mantle rocks were juxtaposed by motion on the submarine Finch-Langdon fault. White boxes show sample sites, detail maps shown in Figure 2.3.

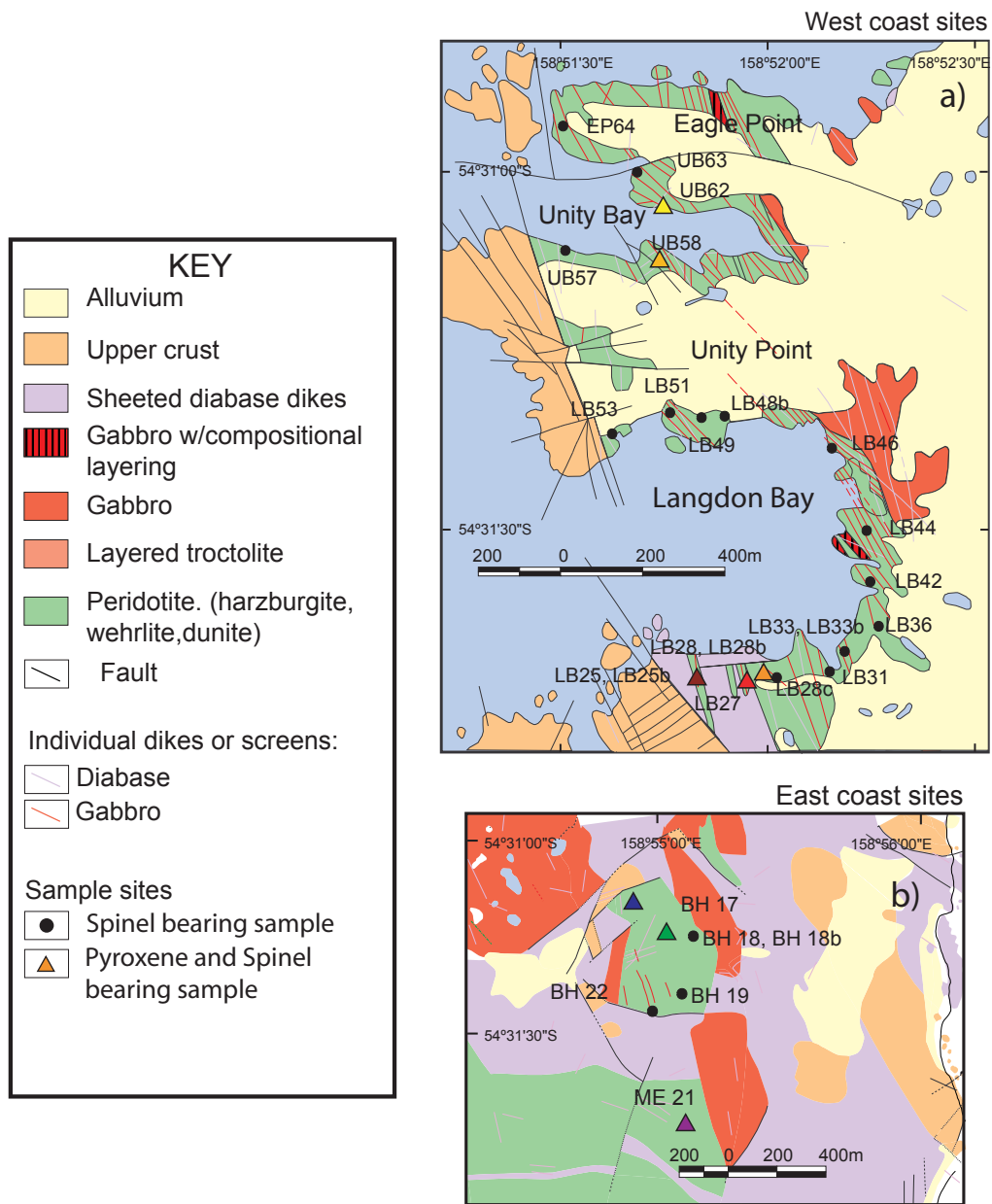


Figure 2.3. Detailed geologic maps (Goscombe and Everad, 1998) for areas sampled (see figure 2.2 for locations). Residual harzburgites were sampled on the west (a) and east (b) sides of the island for geochemical analyses.

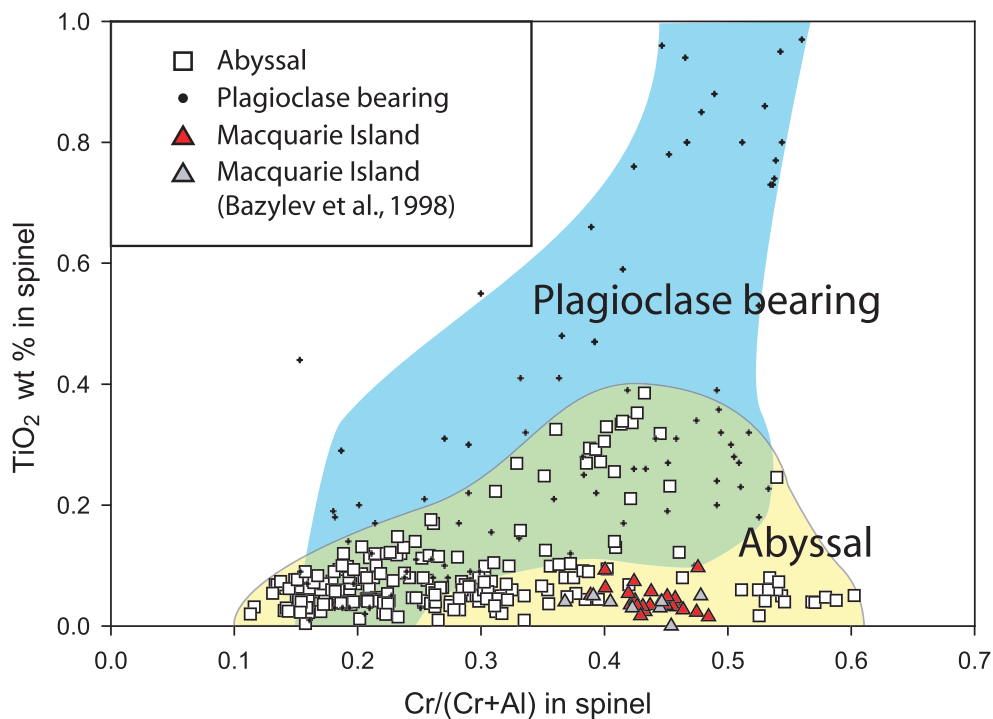


Figure 2.4. Cr-number vs. TiO<sub>2</sub> in spinel. Spinel Cr-numbers (= molar Cr/(Cr+Al)) in the Macquarie Island peridotites range from 0.39 to 0.48, corresponding to 15-16% fractional melting. TiO<sub>2</sub> contents are low (0.02-0.1), attesting to the residual nature of MI peridotites. All samples fall within the range of abyssal peridotites, and none are plagioclase-bearing. Additional data from (Bazylev and Kamenetsky, 1998; Cannat and Seyler, 1995; Charpentier, 2000; Dick, 1989; Dick and Bullen, 1984; Dick and Natland, 1996; Ghose et al., 1996; Hamlyn and Bonatti, 1980; Hellebrand et al., 2001; Hellebrand et al., 2002a; Hellebrand et al., 2002b; Kornprobst and Tabit, 1988; Pearce et al., 2000; Ross and Elthon, 1997; Seyler and Bonatti, 1997) and our unpublished data. Note: most abyssal peridotite samples are from slow to intermediate spreading ridges.

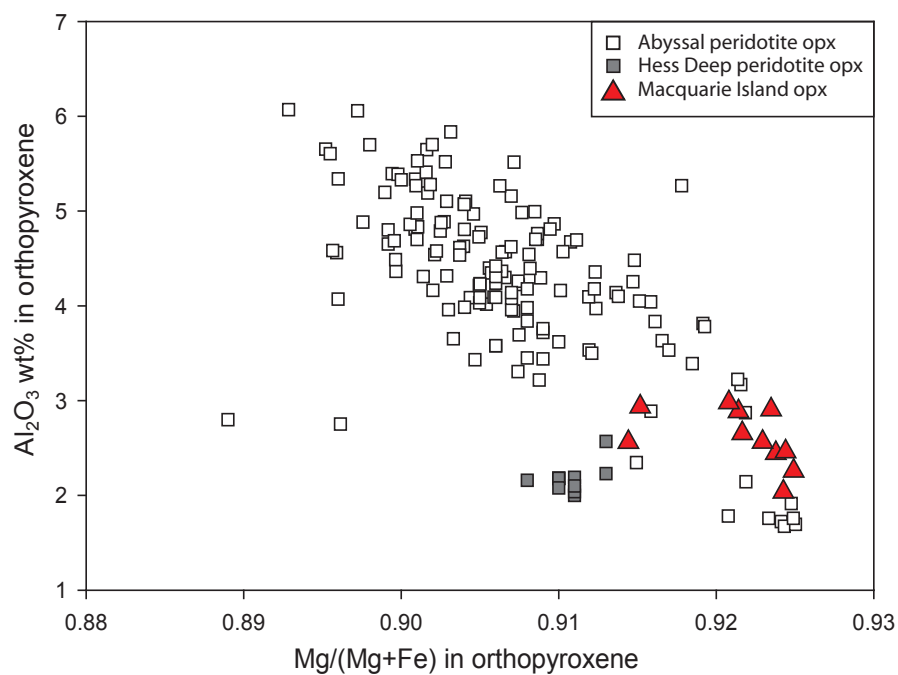


Figure 2.5. Al<sub>2</sub>O<sub>3</sub> vs. Mg-number (= molar Mg/(Mg+Fe<sup>2+</sup>) in opx porphyroclast cores. Values range from 2.05-2.99 wt % Al<sub>2</sub>O<sub>3</sub> with high Mg-numbers (0.92 on average) (Table 2.2). Both indicate a high degree of melting, corresponding to the high Cr-numbers in spinel. These values are low for Al<sub>2</sub>O<sub>3</sub> and high for Mg-numbers compared to most abyssal peridotites. Rocks recovered from Hess Deep (HD) have similarly low Al<sub>2</sub>O<sub>3</sub> contents, although Mg-numbers are lower than Macquarie Island. Data from Dick and Natland 1996, Ross and Elthon 1997, Johnson et al 1990, Johnson and Dick 1992, Hellebrand et al 2002.

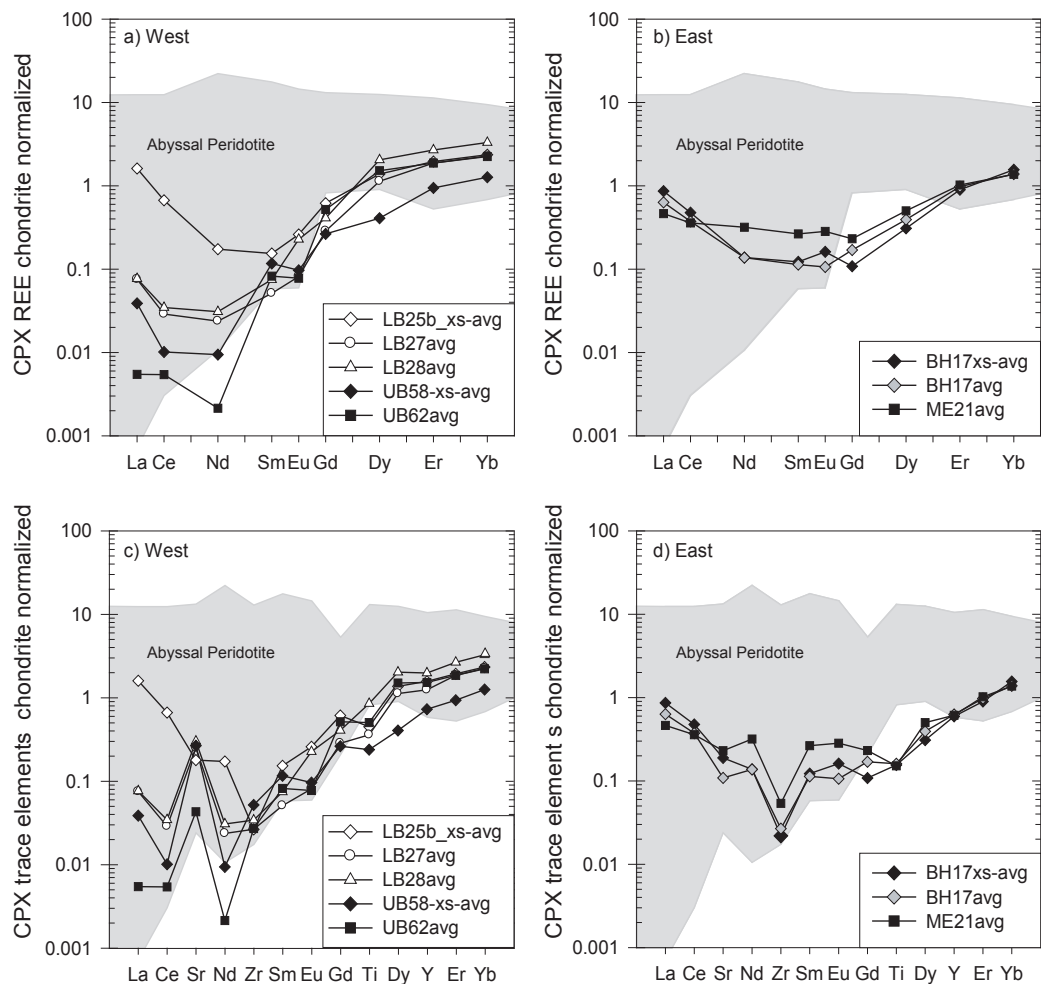


Figure 2.6. Rare earth elements and trace elements in MI peridotites. Abyssal peridotite patterns are typically flat or more depleted in LREE and highly incompatible elements. a,b) Rare earth elements in clinopyroxene, normalized to chondrite. East and west sections have been plotted separately for clarity. All samples are depleted in HREEs, enriched in LREEs, producing a "spoon-shaped" rare earth pattern common in ophiolites, unknown in abyssal peridotites. It has been proposed that this pattern is caused by hydrous partial melting. c,d) Trace elements in cpx, normalized to chondrite. All samples display a uniform depletion of less incompatible elements, and variable enrichment of highly incompatible elements. Four western samples have a strong positive strontium anomaly, suggesting fluid-derived enrichment during melting. Abyssal peridotite cpx fields from Max Planck institute database. Abyssal peridotite cpx data from Dick and Natland 1996, Ross and Elthon 1997, Johnson et al 1990, Johnson and Dick 1992, Hellebrand et al 2002, Chondrite values from (Anders and Grevesse, 1989).

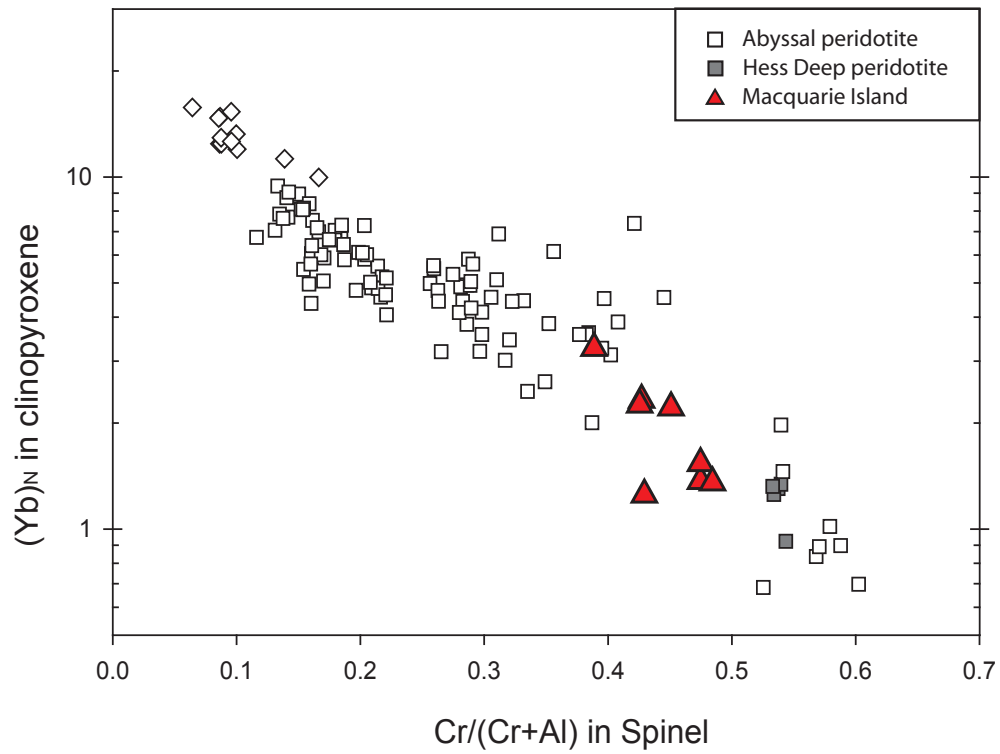


Figure 2.7. Yb vs. Cr-number. Despite variable LREE enrichment, Macquarie Island samples plotted with abyssal peridotite Yb (chondrite normalized) vs. Cr-numbers fall within a linear trend, filling in a gap where no abyssal data has been measured. Data from (Charpentier, 2000; Dick and Natland, 1996; Hellebrand et al., 2001; Hellebrand et al., 2002a; Hellebrand et al., 2002b; Ross and Elthon, 1997). Chondrite values from (Anders and Grevesse, 1989).

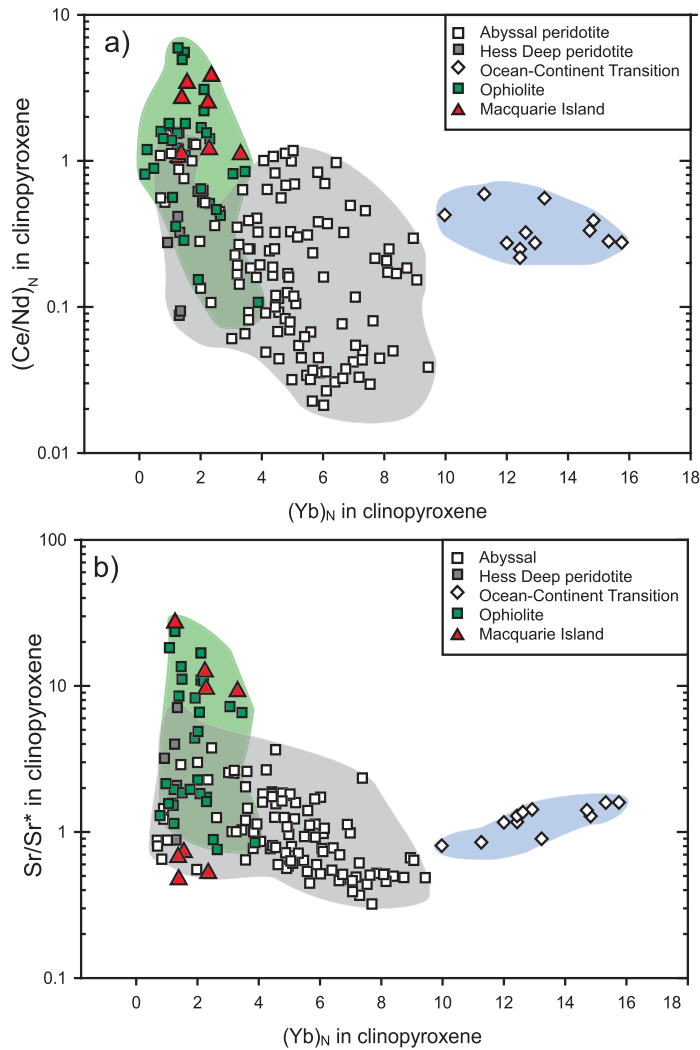


Figure 2.8. Ce/Nd, Sr/Sr\* vs. Yb. a) Ce/Nd vs. Yb (chondrite normalized) for Macquarie Island, abyssal peridotites and ophiolites. This shows a clear difference between Macquarie Island and abyssal peridotites, with Macquarie Island cpx possessing higher Ce/Nd at a given Yb concentration, similar to ophiolites. b) Macquarie Island cpx Sr/Sr\* vs. Yb fall into two groups, those that have a pronounced positive Sr anomaly and those that do not. Enrichment of this kind is often seen in ophiolites, but not in abyssal peridotites. Ophiolite data from (Batanova et al., 1998; Bizimis et al., 2000; Morishita et al., 2003), Coogan, unpublished data, Suhr, unpublished data. Abyssal peridotite data from (Charpentier, 2000; Dick and Natland, 1996; Hellebrand et al., 2001; Hellebrand et al., 2002a; Hellebrand et al., 2002b; Ross and Elthon, 1997). Chondrite values from (Anders and Grevesse, 1989).

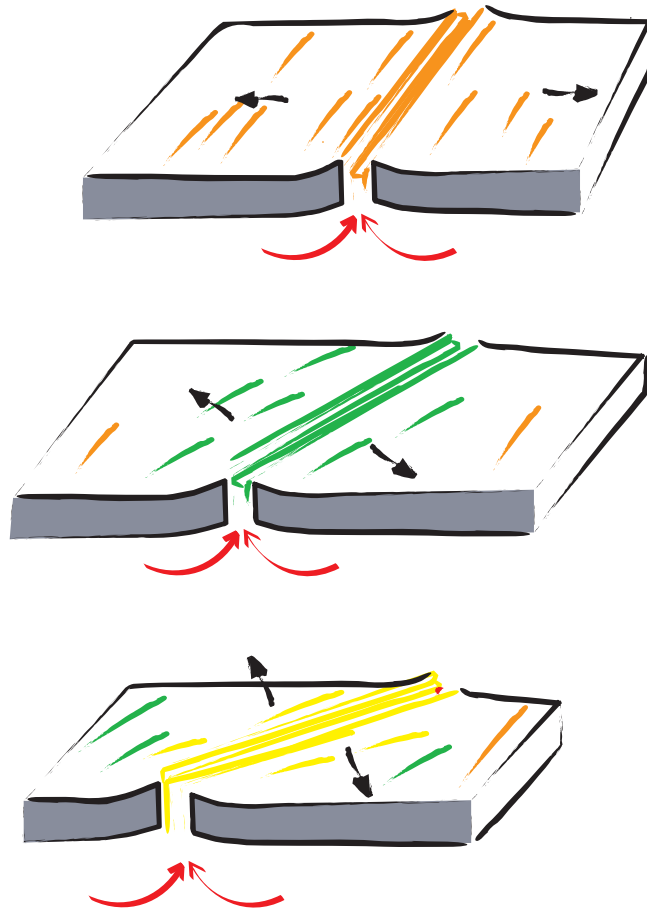


Figure 2.9. Changing spreading direction could have caused repeated melting of same mantle source resulting in the depletion and low Cr-numbers seen in the Macquarie Island peridotites.

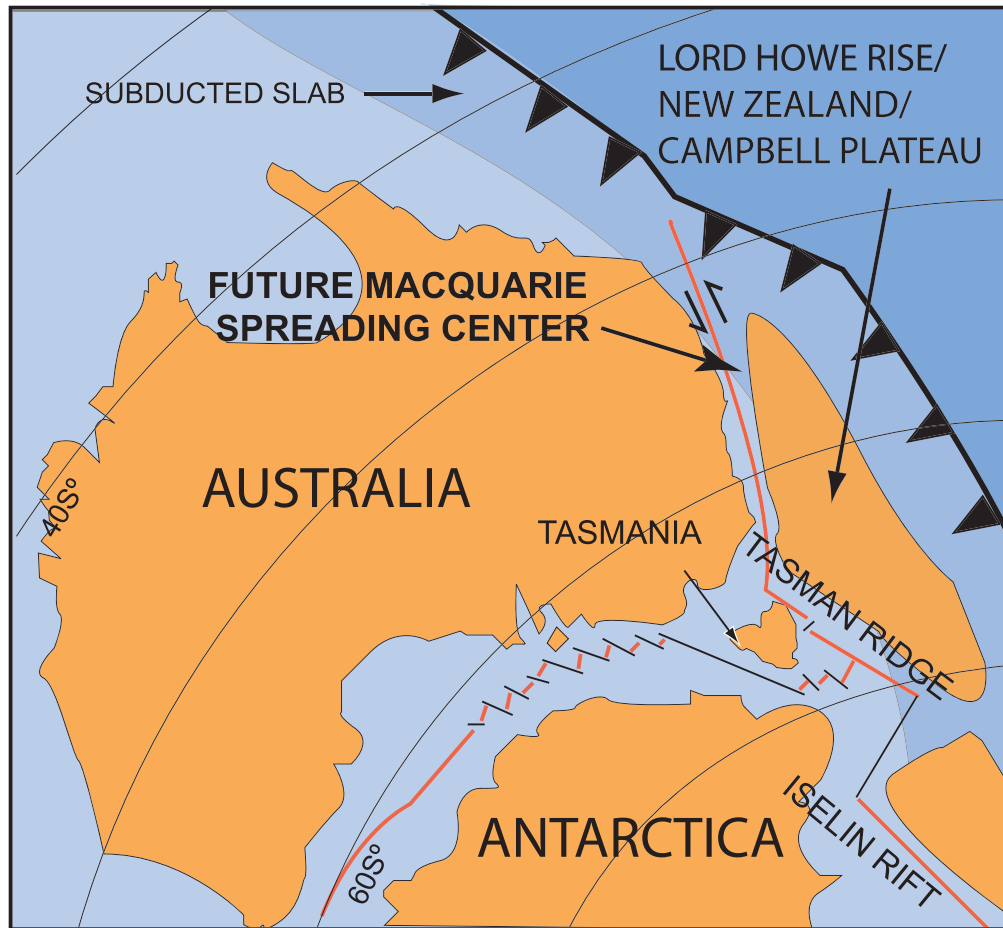


Figure 2.10. Slab contamination of the mantle. Plate reconstruction after Li and Powell, 2000. Subduction may have been occurring beneath the Lord Howe Rise/New Zealand region approximately 96 MYA. Subduction moved eastward, possibly abandoning the subducted slab, the dehydration of which could have later enhanced melting during Macquarie Ridge spreading.

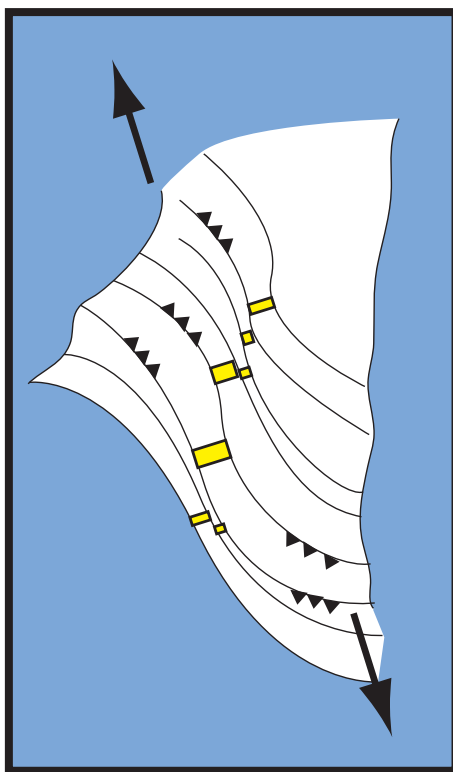


Figure 2.11. Small-scale subduction along curved fracture zones could introduce fluids to enhance melting and cause fluid-mobile element enrichment. Black triangles symbolize subduction, arrows indicate spreading direction. Figure shows configuration ca. 10 Ma after Massell et al (2000).

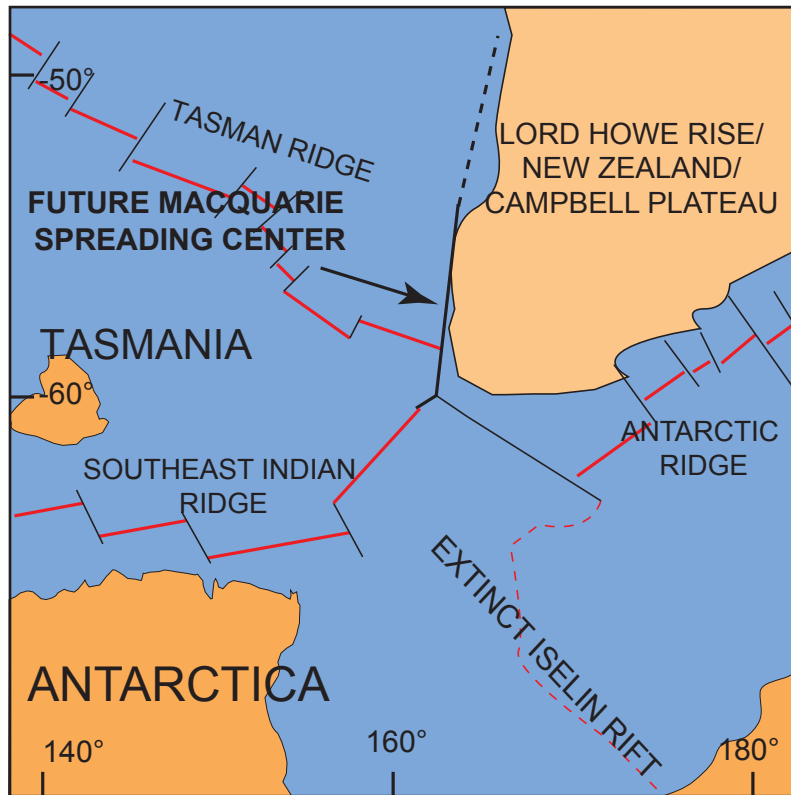


Figure 2.12. Rifting of pre-existing transform. Plate reconstructions after Marks and Stock, 1997. At approximately 60 Ma, the Southwest Indian ridge is propagating into the Tasman Ridge. A hypothetical transform has been suggested as a weakness that would be susceptible to rifting if favored by plate motions (Wood et al., 1996). Such a transform would facilitate alteration of the crust and lithospheric mantle that could later be incorporated by upwelling mantle.

Table 2.1a Average major element compositions of spinel of Macquarie Island peridotites measured by electron microprobe. Gr= grain, n = spot numbers. Cr-no = (Cr/(Cr+Al)), Mg-no = (Mg/(Mg+Fe)).

SAMPLE	gr	n	TiO <sub>2</sub>	Al <sub>2</sub> O <sub>3</sub>	Cr <sub>2</sub> O <sub>3</sub>	V <sub>2</sub> O <sub>3</sub>	FeO	MgO	MnO	CaO	NiO	CoO	ZnO	Total	Cr-no.	Mg-no.
s-LB25	5	15	0.04	31.23	37.38	0.21	15.71	14.93	0.17	0.01	0.13	0.03	0.15	100.03	0.445	0.659
s-LB25b	5	19	0.03	32.08	35.64	0.22	17.55	14.07	0.17	0.01	0.10	0.04	0.26	100.26	0.427	0.620
s-LB27	4	16	0.03	32.58	35.95	0.19	15.59	15.07	0.16	0.01	0.13	0.04	0.18	100.11	0.425	0.663
s-LB28	4	14	0.05	35.04	33.20	0.17	15.56	15.21	0.13	0.00	0.13	0.04	0.20	99.80	0.389	0.665
s-LB28b	4	16	0.03	31.89	36.90	0.21	15.33	15.03	0.15	0.00	0.13	0.04	0.16	99.96	0.437	0.666
s-LB28c	4	16	0.04	32.48	35.20	0.21	16.52	14.82	0.15	0.00	0.13	0.04	0.20	99.88	0.421	0.646
s-LB31	3	9	0.18	28.41	38.87	0.24	17.90	13.50	0.21	0.00	0.12	0.03	0.17	99.70	0.479	0.605
s-LB33	3	9	0.06	33.98	33.89	0.18	15.64	15.43	0.16	0.01	0.16	0.03	0.16	99.76	0.401	0.667
s-LB33b	3	9	0.04	32.08	35.33	0.19	16.29	14.93	0.14	0.01	0.14	0.04	0.18	99.46	0.425	0.651
s-LB36	2	8	0.02	29.23	33.48	0.20	16.35	15.78	0.17	0.02	0.13	0.03	0.19	98.10	0.433	0.655
s-LB42	4	15	0.04	30.04	37.31	0.23	18.06	14.18	0.18	0.01	0.13	0.02	0.19	100.48	0.455	0.615
s-LB44	3	12	0.03	31.64	35.74	0.21	16.70	14.65	0.15	0.01	0.12	0.04	0.17	99.54	0.431	0.641
s-LB46	4	16	0.05	32.48	34.96	0.20	17.03	14.71	0.17	0.00	0.14	0.03	0.20	100.06	0.419	0.637
s-LB48b	2	8	0.03	32.38	35.90	0.20	15.59	15.18	0.15	0.00	0.13	0.03	0.19	99.87	0.426	0.665
s-LB49	3	9	0.06	31.62	36.70	0.18	14.98	15.30	0.14	0.01	0.14	0.04	0.13	99.35	0.438	0.675
s-LB51	4	12	0.03	30.94	37.75	0.20	15.84	14.79	0.17	0.01	0.15	0.03	0.15	100.14	0.450	0.655

Table 2.1b Average major element compositions of spinel of Macquarie Island peridotites measured by electron microprobe. Gr= grain, n = spot numbers. Cr-no = (Cr/(Cr+Al)), Mg-no = (Mg/(Mg+Fe)).

SAMPLE	gr	n	TiO <sub>2</sub>	Al <sub>2</sub> O <sub>3</sub>	Cr <sub>2</sub> O <sub>3</sub>	V <sub>2</sub> O <sub>3</sub>	FeO	MgO	MnO	CaO	NiO	CoO	ZnO	Total	Cr-no.	Mg-no.
s-LB25	5	15	0.04	31.23	37.38	0.21	15.71	14.93	0.17	0.01	0.13	0.03	0.15	100.03	0.445	0.659
s-LB25b	5	19	0.03	32.08	35.64	0.22	17.55	14.07	0.17	0.01	0.10	0.04	0.26	100.26	0.427	0.620
s-LB27	4	16	0.03	32.58	35.95	0.19	15.59	15.07	0.16	0.01	0.13	0.04	0.18	100.11	0.425	0.663
s-LB28	4	14	0.05	35.04	33.20	0.17	15.56	15.21	0.13	0.00	0.13	0.04	0.20	99.80	0.389	0.665
s-LB28b	4	16	0.03	31.89	36.90	0.21	15.33	15.03	0.15	0.00	0.13	0.04	0.16	99.96	0.437	0.666
s-LB28c	4	16	0.04	32.48	35.20	0.21	16.52	14.82	0.15	0.00	0.13	0.04	0.20	99.88	0.421	0.646
s-LB31	3	9	0.18	28.41	38.87	0.24	17.90	13.50	0.21	0.00	0.12	0.03	0.17	99.70	0.479	0.605
s-LB33	3	9	0.06	33.98	33.89	0.18	15.64	15.43	0.16	0.01	0.16	0.03	0.16	99.76	0.401	0.667
s-LB33b	3	9	0.04	32.08	35.33	0.19	16.29	14.93	0.14	0.01	0.14	0.04	0.18	99.46	0.425	0.651
s-LB36	2	8	0.02	29.23	33.48	0.20	16.35	15.78	0.17	0.02	0.13	0.03	0.19	98.10	0.433	0.655
s-LB42	4	15	0.04	30.04	37.31	0.23	18.06	14.18	0.18	0.01	0.13	0.02	0.19	100.48	0.455	0.615
s-LB44	3	12	0.03	31.64	35.74	0.21	16.70	14.65	0.15	0.01	0.12	0.04	0.17	99.54	0.431	0.641
s-LB46	4	16	0.05	32.48	34.96	0.20	17.03	14.71	0.17	0.00	0.14	0.03	0.20	100.06	0.419	0.637
s-LB48b	2	8	0.03	32.38	35.90	0.20	15.59	15.18	0.15	0.00	0.13	0.03	0.19	99.87	0.426	0.665
s-LB49	3	9	0.06	31.62	36.70	0.18	14.98	15.30	0.14	0.01	0.14	0.04	0.13	99.35	0.438	0.675
s-LB51	4	12	0.03	30.94	37.75	0.20	15.84	14.79	0.17	0.01	0.15	0.03	0.15	100.14	0.450	0.655

Table 2.2. Average major element compositions of orthopyroxene of Macquarie Island peridotites measured by electron microprobe. Gr= grain, n = spot numbers. Cr-no = (Cr/(Cr+Al)), Mg-no = (Mg/(Mg+Fe)).

Sample	gr	n	SiO <sub>2</sub>	TiO <sub>2</sub>	Al <sub>2</sub> O <sub>3</sub>	Cr <sub>2</sub> O <sub>3</sub>	FeO	MnO	MgO	CaO	NiO	Na <sub>2</sub> O	K <sub>2</sub> O	Total	Cr-no.	Mg-no
o-LB27	6	19	52.93	0.01	2.95	0.96	6.26	0.15	33.12	1.62	0.10	0.02	0.00	98.12	0.179	0.915
o-LB28b	3	9	55.26	0.00	2.90	0.92	5.69	0.14	32.78	2.32	0.09	0.01	0.01	100.12	0.176	0.921
o-LB36	2	6	54.88	0.01	2.67	0.82	5.70	0.13	32.89	2.48	0.08	0.02	0.00	99.66	0.170	0.922
o-LB42	3	12	54.64	0.03	2.58	0.81	6.31	0.15	33.14	1.71	0.10	0.01	0.00	99.49	0.175	0.914
o-LB48b	3	11	55.15	0.02	2.99	0.95	5.81	0.14	33.19	2.02	0.12	0.01	0.01	100.41	0.175	0.921
o-UB62	1	4	55.15	0.01	2.92	0.95	5.69	0.14	33.76	1.67	0.10	0.02	0.00	100.40	0.179	0.923
o-BH17	2	5	55.48	0.01	2.48	0.77	5.51	0.11	33.12	2.14	0.09	0.01	0.01	99.72	0.172	0.924
o-BH18	2	8	55.46	0.02	2.58	0.80	5.70	0.12	33.53	1.54	0.09	0.03	0.01	99.86	0.172	0.923
o-BH18b	2	8	54.59	0.05	2.05	0.78	5.70	0.13	34.19	1.54	0.08	0.04	0.00	99.17	0.204	0.924
o-BH19	2	8	55.77	0.01	2.46	0.75	5.70	0.13	33.98	1.51	0.12	0.03	0.01	100.47	0.169	0.924
o-ME21	5	20	55.30	0.02	2.27	0.74	5.59	0.13	33.83	1.72	0.09	0.02	0.00	99.71	0.179	0.925

Table 2.3a. Average major and trace element compositions of clinopyroxenes of Macquarie Island peridotites measured by electron microprobe, west section. Gr = grain, n = numbers of analyzed spots. Cr-no = (Cr/(Cr+Al)), Mg-no = (Mg/(Mg+Fe)).

Major wt%	c-LB25b	c-LB27	c-LB28	c-LB28b	c-LB36	c-LB42	c-LB48b
gr	1	2	5	2	1	7	4
n	2	8	19	7	2	22	16
SiO <sub>2</sub>	51.00	51.75	51.57	52.22	52.44	52.17	51.93
TiO <sub>2</sub>	0.06	0.02	0.07	0.04	0.00	0.05	0.03
Al <sub>2</sub> O <sub>3</sub>	2.83	3.60	3.92	3.20	2.97	2.91	3.48
Cr <sub>2</sub> O <sub>3</sub>	1.20	1.40	1.40	1.28	1.27	1.21	1.34
FeO	2.18	2.29	2.27	2.43	2.14	2.25	2.36
MnO	0.07	0.08	0.08	0.10	0.10	0.09	0.09
MgO	16.89	17.32	17.25	17.64	17.02	17.17	17.62
CaO	23.74	22.60	22.48	22.69	24.08	23.14	22.89
NiO	0.02	0.08	0.05	0.08	0.05	0.05	0.06
Na <sub>2</sub> O	0.02	0.06	0.08	0.04	0.03	0.18	0.04
K <sub>2</sub> O	0.00	0.00	0.00	0.00	0.00	0.00	0.01
Total	98.00	99.21	99.16	99.71	100.09	99.22	99.85
Cr-no	0.218	0.207	0.193	0.211	0.224	0.219	0.205
Mg-no	0.940	0.939	0.939	0.937	0.942	0.940	0.938
Trace (ppm)	c-LB25b	c-LB27	c-LB28				
n	3	4	2				
Ti	202	161	382				
Sr	1.31	1.84	2.20				
Y	2.50	1.97	3.14				
Zr	0.10	0.10	0.13				
La	0.38	0.02	0.02				
Ce	0.41	0.02	0.02				
Nd	0.08	0.01	0.01				
Sm	0.02	0.01	0.01				
Eu	0.01	0.00	0.01				
Gd	0.12	0.06	0.08				
Dy	0.34	0.28	0.50				
Er	0.32	0.30	0.44				
Yb	0.39	0.38	0.55				

Table 2.3b. Average major and trace element compositions of clinopyroxenes of Macquarie Island peridotites measured by electron microprobe, east section. Gr = grain, n = numbers of analyzed spots. Cr-no =  $(Cr/(Cr+Al))$ , Mg-no =  $(Mg/(Mg+Fe))$ .

Major wt%	c-UB58	c-UB62	c-BH17	c-BH19	c-ME21
gr	1	2	5	1	1
n	4	6	18	4	3
SiO <sub>2</sub>	51.36	52.36	52.64	51.94	52.43
TiO <sub>2</sub>	0.03	0.04	0.02	0.03	0.03
Al <sub>2</sub> O <sub>3</sub>	3.48	3.18	2.49	3.09	2.70
Cr <sub>2</sub> O <sub>3</sub>	1.56	1.28	0.99	1.39	1.21
FeO	2.14	2.17	2.25	2.24	2.40
MnO	0.07	0.09	0.09	0.10	0.08
MgO	17.08	17.65	17.47	17.09	17.74
CaO	22.84	23.31	23.45	22.56	23.01
NiO	0.06	0.05	0.04	0.04	0.03
Na <sub>2</sub> O	0.26	0.13	0.11	0.27	0.15
K <sub>2</sub> O	0.01	0.00	0.00	0.00	0.00
Total	98.90	100.26	99.57	98.74	99.78
Cr-no	0.231	0.212	0.211	0.232	0.231
Mg-no	0.942	0.943	0.940	0.939	0.938

Trace (ppm)	c-UB58	c-UB62	c-BH17	c-xs-BH17	ME21
n	3	2	3	2	3
Ti	107	226	72	69	67
Sr	1.95	0.31	0.79	1.37	1.67
Y	1.15	2.42	0.99	0.93	0.96
Zr	0.20	0.11	0.10	0.08	0.21
La	0.01	0.00	0.15	0.20	0.11
Ce	0.01	0.00	0.23	0.29	0.22
Nd	0.00	0.00	0.06	0.06	0.15
Sm	0.02	0.01	0.02	0.02	0.04
Eu	0.01	0.00	0.01	0.01	0.02
Gd	0.05	0.10	0.03	0.02	0.05
Dy	0.10	0.37	0.10	0.08	0.12
Er	0.15	0.30	0.16	0.14	0.17
Yb	0.21	0.37	0.23	0.26	0.23

## **Chapter 3: Temporal patterns of incompatible-element enrichment in Macquarie Island basalts**

### **3.1 ABSTRACT**

Volcanic stratigraphic sections of basalts of Macquarie Island, an uplifted section of ocean crust and upper mantle, were studied to evaluate major and trace element geochemical changes with time. The basalts formed during the final stages of magmatism on the paleo-Macquarie spreading ridge between ~12 and 6 Ma (Duncan and Varne, 1988, my data), thus, their chemistry may provide information about processes that occurred at the end of spreading. Structural and stratigraphic relationships were used to determine age relationships within the sections; radiometric ages and degrees of alteration (Duncan and Varne, 1988) and plate tectonic reconstructions (Massell et al., 2000) were used to determine relative age between the sections. A series of different patterns of enrichment in incompatible trace elements and REEs emerged from my analyses that may reflect different eruption episodes. The oldest stratigraphic section is characterized by a steady decline in incompatible trace element enrichment with time and may have formed during volcanism that is unrelated to the younger eruptions. One younger section is characterized by high variability in enrichment, whereas the three youngest sections show relatively constant levels of enrichment. Overall, these final four sections show a decrease in enrichment with time.

I have interpreted this variability and subsequent decline in enrichment to be the result of eruption of initially isolated melt fractions that were later able to

mix as the eruption cycle progressed, coupled with an increase of melt production as the magmatic system developed. This pattern may be the expression of sporadic volcanism at the end of spreading. Alternately, it may be caused by progressive ridge propagation rifting older crust, with early eruptions characterized by diverse compositions and later characterized by more constant compositions. In both cases the overall decrease in enrichment may be linked to an effective increase in spreading rate that increased melting.

### **3.2 INTRODUCTION**

Variations in oceanic basalt geochemistry are common worldwide, yet few studies have examined the relationship between variations in chemistry and structural/stratigraphic position within continuous sections in either submarine rocks (Meurer et al., 2001), intra-plate volcanoes (Reiners, 2002), or ophiolites (Einaudi et al., 2003). Studies of this kind provide valuable information about the evolution of magma chambers and, ultimately, tectonic processes; unfortunately, detailed stratigraphic work can be difficult within an oceanic setting. Macquarie Island, located on the Australian-Pacific plate boundary between New Zealand and Antarctica (Figure 3.1), is unique in that it is a complete section of oceanic crust and upper mantle peridotite uplifted (Griffin and Varne, 1978; Varne et al., 1969) in situ during transpression (Daczko et al., 2003; Meckel et al., in press). Therefore, the rocks of the island have not been influenced by either subduction or obduction as seen in other ophiolites. This history, combined with 1) many well-exposed undisturbed sections of volcanic rocks in which detailed spatial relationships can be determined and 2) wide variations in incompatible trace

element contents in basalts (Kamenetsky, 2000), make Macquarie Island an excellent location to investigate changes in geochemistry with time. Moreover, the rocks of the island formed in the final stages of spreading on the paleo-Macquarie spreading ridge that was active between ~40 and 6 Ma (Cande et al., 2000; Massell et al., 2000). The goal of this study was to obtain information about the geochemical and tectonic processes occurring when volcanism shuts down.

The geology and tectonic setting of the island and the Australian-Pacific plate boundary have been described in detail elsewhere (Daczko et al., 2003; Goscombe and Everard, 2001; Varne et al., 2000). In brief, rifting began at ~40 Ma along what is now the modern Australian-Pacific plate boundary (Cande et al., 2000). Over the next ~35 my, the spreading direction progressively rotated in response to changes in Australian-Pacific relative plate motion, resulting in the cessation of spreading and the onset of transpression <6 Ma (Lamarche et al., 1997; Massell et al., 2000). All levels of ocean crust including upper mantle rocks are found on the island (Figure 3.1), and faults that juxtapose the upper crust and lower crust/upper mantle sections are interpreted to have formed near the intersection of a ridge and a transform (Wertz et al., 2000a, 2000b). More than two-thirds of the island is composed of basalt; this study is the first on Macquarie Island to relate the basalt geochemistry to their structural and stratigraphic position.

## **3.2 METHODS**

### **3.2.1 Field techniques**

Six localities on Macquarie Island were selected, covering areas from north to south on both the east and west coasts (Figure 3.1). Four of the sites are extensive coastal cross sections, with up to 100% exposure, ranging in length from 500 to 1500 meters (Aerial Cove, Bauer Bay, Hurd Point, and Green Gorge, henceforth referred to as AC, BB, HP, and GG respectively - GG comprised of northern and southern sections (GN and GS)). Two sites (Pyramid Peak, PP, and Major Lake, ML) are on the plateau of the island, approximately 250 meters topographically above the stratigraphic sections.

A 1:1000 geologic map and corresponding stratigraphic column was made in each section, using spatial relationships to determine relative ages between the units. Volcanic units were distinguished based on the following physical characteristics: phenocryst type, size, shape and number; habit (pillows, dikes, flows or hyaloclastite) and vesicularity. Orientations of different units were measured using evident tails and flattened tops of pillows and flows with obvious contacts; dikes were measured along chilled margins. Both basaltic glass and associated basalt rock were collected for chemical analysis (glass) and petrography (both glass and rock). Glass was found forming pillow rims and hyaloclastite matrix. Both fresh and altered glass, where available, were collected to monitor chemical changes due to alteration. In the field, altered glass is often green and dull in color instead of glassy black. In the laboratory, altered glass

shows de-vitrification and has a tendency to disintegrate during sample preparation. No glass was found associated with sheet flows of basalt.

### **3.2.2 Analytical techniques**

Basaltic glass was crushed and fresh chips were handpicked. Double-sided polished sections were made to ensure all analyses were made with clear, microphenocryst free glass.

H<sub>2</sub>O contents of the glasses were measured via Fourier-transform infrared spectroscopy in the University of Tasmania Central Science Laboratory (CSL), using a Digilab FTS-20E spectrometer, following the protocol of (Danyushevsky et al., 2000). Major elements, S and Cl were measured in the same chips using the Cameca SX100 electron microprobe in the CSL using USNM 111240/52 (VG-2) as a standard. A 15kv beam accelerating voltage and 20 nA beam current was used, and four spots per chip were analyzed. Trace elements were measured on the same spots by laser ablation using a UP213 New Wave Research laser probe attached to an Agilent HP 4500 ICP-MS at the Centre for Ore Deposit Research, University of Tasmania. NIST 612 and BCR-2 were used as primary and secondary standards, respectively. Each analysis for each element was confirmed to be within detection limits (except for some elements in sample H76, due to alteration of the glass), and precision and error were verified for each analysis. Errors were insufficient to affect the final values. P and K were compared to microprobe analyses as an external check.

### **3.3 RESULTS**

#### **3.3.1 Geology**

Each section has a succession (Figure 3.2) of plagioclase phyric and aphyric, pillow basalt (Figure 3.4a) and sheeted basalt flows (Figure 1.10a), interspersed with hyaloclastite (Figure 3.4b), representing eruption packages alternating between less voluminous (pillows) and more voluminous (flows), often topped by hyaloclastite breccia. All of the phyric basalts have partially resorbed plagioclase phenocrysts in apparent disequilibrium with the melt; these units range 1-35% phenocrysts, and phenocrysts range in size from 1-15 mm. Two sections (HP and GG) represent single complete eruptive events that begin with phyric pillow basalts. HP transitions to mixed aphyric and phyric pillows and flows, then to vesicular aphyric pillows and associated feeder dikes, ending with a hyaloclastite breccia with clasts of the preceding aphyric basalt (Figure 3.2). GG begins with phyric pillows and transitions to vesicular aphyric pillows, then to a pillow rich hyaloclastite (Figure 3.5), ending with a hyaloclastite breccia (Figure 3.2).

BB is a thicker, more complicated section, with sequences of eruptions that change from flows, transition to pillows, to pillow-rich hyaloclastite, then to hyaloclastite (Fig. 3.2). One lava flow contains magmatic amphibole. This section also has extensive evidence of syn-volcanic sedimentation (Wertz et al., 2000a, 2000b), with talus breccias, sandstones and mudstones containing clasts of basalt, diabase and gabbro (Figs. 1.10). This package is topped by a very thick unit of talus breccia (~140m thick), which is overlain by a volcanic flow.

AC is the northernmost section and begins with a hyaloclastite, continuing to aphyric pillows, then to pillow rich hyaloclastite, then hyaloclastite (Figure 3.2). The top two units are phyric vesicular pillows topped by aphyric pillows.

The final two sections (ML and PP) are from the top of the plateau between HP and GG. Basalts at PP are phyric and vesicular, and preserved volcanoes (Figure 3.6) have hyaloclastite plugs at their tops. Glass samples were collected from four peaks in the area. Two peaks have well-preserved elongate pillow basalts that radiate from their summits, and are assumed to be the youngest because of this morphology. The other two peaks have retained their conical shape but do not have outer radial pillows, and appear to be related, but slightly older. Both locations have rare outcrops of unusual plagioclase-rich, amphibole-bearing sills and picritic basalts that are either flows or sills. These units are mostly restricted to the higher elevations in the center of the island. In this study, only one amphibole-bearing unit was found on the coast, within the Bauer Bay section, although one such unit is mapped (Goscombe and Everard, 1998) west of PP, on the coast in an area that was inaccessible during my field seasons.

The ML sample analyzed for glass geochemistry is from aphyric pillow basalt; the contact between the pillow basalt and a plagioclase-bearing picrite unit is not exposed. However, they are < 10 m apart, and it appears that the picrites are either inter-bedded with or intruding the pillows, so they are either roughly the same age or they are younger than the pillows. No glass was found associated with either the picrites or the amphibole-bearing rocks and therefore these were

not analyzed for this study. Their association with analyzed pillow basalts displays at least one period of exceptionally diverse volcanism, however, which will be addressed in the geochemistry discussion.

### ***3.3.1.1 Relative stratigraphic position***

Stratigraphic position within each of the six sections was determined by direct field relationships as shown in Figure 3.2. Relative age between the sections from the six locations was estimated using a combination of age data where available, location, and degree of alteration. Some age relationships were constrained using  $^{40}\text{Ar}/^{39}\text{Ar}$  ages whole rock (Duncan and Varne, 1988) and glass ages (my preliminary data) and K-Ar ages (Duncan and Varne, 1988). These dates are used with caution, however, because they are a mixture of whole rock, glass and mineral ages, from basalt flows and dikes, and therefore, they may not be comparable. For example, the previous whole rock and mineral separate ages may record or be influenced by the time of crystal growth, whereas the glass ages should record the time of eruptions when the glasses were quenched. They were also analyzed in different labs, which makes comparison less reliable. For these reasons, additional glass samples that are tied to the measured stratigraphic sections are currently being dated by Terry Spell at the University of Nevada Las Vegas (UNLV) and will provide further age constraints, but these ages are not available at this time. Another age constraint was location. Rocks on the top of the plateau are assumed to be younger than those on the coasts at similar latitudes because the coastal exposures are hundreds of meters topographically lower than the current day plateau, and the island was for the most part uplifted as a unit

(Adamson et al., 1996). Also, the Massell et al. (2000) model predicts that the oldest rocks will be at the south end of the island and the youngest in the north. Lastly, the degree of alteration representing crustal depth exposed (Goscombe and Everard, 2001; Griffin and Varne, 1978) was considered as another constraint. Below I describe the rationale for the arrangement of the sections in Figure 3.3 from oldest to youngest:

HP: Hurd Point is the southernmost site, and plate tectonic reconstructions suggest that the oldest rocks should be in the south (Massell et al., 2000). These rocks have experienced a higher degree of alteration and have been interpreted as the deepest rocks of the upper crust on the island (Goscombe and Everard, 2001; Griffin and Varne, 1978), suggesting that they are the oldest. Furthermore, a dike that cuts the pillows at HP has an  $^{40}\text{Ar}/^{39}\text{Ar}$  age of  $7.3\pm 0.6\text{Ma}$  (whole rock), which has been reported to represent the end of greenschist metamorphism (Duncan and Varne, 1988), indicating that the pillows are older than this age. The southern rocks have the poorest radiometric age control, however, and their alteration prevents accurate age dating.

ML: Major Lake is north of HP, and the analyzed basalt at ML is topographically higher than the nearby HP section. It consists of altered pillows that make up the flat, eroded surface of the plateau, and is south of the rest of the sections. Thus it is assumed to younger than the HP section but older than the rest.

BB: Bauer Bay is placed next because a flow on Mawson Point has been dated at  $11.5 \pm 0.3 \text{ Ma}$  ( $^{40}\text{Ar}/^{39}\text{Ar}$ , whole rock) (Duncan and Varne, 1988). The measured section at BB is older than this dated sample.

GG: Green Gorge is placed next even though it is south of BB. An  $^{40}\text{Ar}/^{39}\text{Ar}$  age of  $6.1 \pm 0.09 \text{ Ma}$  was determined for volcanic glass from one of my samples by Terry Spell at UNLV. This date is interpreted as the age of eruption when the glass was quenched. The basalts also have less extensive alteration than at BB

PP: Pyramid Peak appears to have some of the youngest volcanism on the island, as it is the only site with preserved submarine volcanoes (Figure 3.6); all other basalts have been faulted and tilted. The glass associated with the volcanoes is also very fresh. An amphibole separate from within the basalt section structurally beneath the volcanoes at PP yielded a K-Ar age of  $11.5 \pm 0.3 \text{ Ma}$  (Duncan and Varne, 1988). Because the volcanic edifices were built on top of these amphibole-bearing units, the volcanoes, and glasses sampled from them, are assumed to be younger.

AC: Aerial Cove is at the northern-most tip of the island. A volcanic flow was dated here at  $9.7 \pm 0.3 \text{ Ma}$  ( $^{40}\text{Ar}/^{39}\text{Ar}$ , whole rock Duncan and Varne, 1988), however the exceptionally fresh glass in this location and plate tectonic models (Massell et al., 2000) suggest it may be younger. If it were instead placed between BB and GG on the basis of its age, the interpretation below would not change.

### 3.3.2 Geochemistry

Major elements, Cl, S and H<sub>2</sub>O and trace elements are presented in Tables 3.1a-3.1b and 3.2a-3.2d, respectively and are plotted on Figures 3.7-3.12. Analyses from this study are similar to those of Kamenetsky et al (2000, 2001) (Figures 3.7, 3.10, 3.12). Selected major elements (relative to MgO) are plotted in Figure 3.7, with comparison fields for E-MORB and N-MORB (Niu, 1997, 2000) and for MORB from the Mohns Ridge, a slowly spreading, propagating ridge in the North Atlantic (Haase, 1997). Samples have a broad range of major element concentrations, but they generally fall in the E-MORB field, although they have very low FeO contents (Figure 3.7), similar to the Mohns Ridge. In Figures 3.7, 3.8 and 3.10, all major element data (MI and MORB) are normalized to 100%, anhydrous and without Cl, S, and Cr<sub>2</sub>O<sub>3</sub> for more accurate comparison. All basalts analyzed are alkali basalts (Figure 3.12) that are relatively primitive, with 7 to 8 wt% MgO glasses common throughout the section.

Trace elements are plotted in Figures 3.8 and 3.9. All samples are enriched in highly incompatible elements, relative to N-MORB, and many are highly enriched for E-MORB (Figure 3.9; see also Kamenetsky et al., 2000). Some sections (HP, BB, AC) show variability in enrichments within the individual section, whereas GG and PP have relatively constant compositions. The most overall enriched sample is ML 112, and the least enriched is sample AC26b (Figures 3.8, 3.9).

Incompatible element ratios are plotted on Figure 3.10, again with fields for E-MORB, N-MORB (Niu 1997, 2000) and Mohns Ridge (Haase, 1997). The

$K_2O/TiO_2$  and  $(La/Sm)_N$  ratios fall mostly within the E-MORB field, with some more enriched samples, whereas most of the Macquarie Island Nb/Zr ratios are higher than both average N-MORB and E-MORB.

Selected incompatible elements have been plotted in stratigraphic order to better illustrate variance between samples. Figure 3.3 shows the Nb/Zr ratio and Figure 3.11 shows enrichment in other immobile incompatible elements:  $TiO_2$  (at two different scales to include the very different HP samples), Ta, La, Yb, and  $K_2O/TiO_2$ . These plots show that ML and BB have a high variability in enrichment, which decreases in GG and PP. AC has one sample (AC26b) that has lower values. From ML to AC, the sections decrease in the magnitude of variability as well as in overall enrichment (Figure 3.3, 3.11). One sample (GN103c) appears have an anomalously low  $K_2O/TiO_2$  ratio in Figure 3.11; this is due to alteration, which is discussed in the following section.

### ***3.3.2.1 Effects of alteration test***

The geochemistry of oceanic basalts can be affected by hydrothermal activity. The major elements are strongly affected; the rare earth elements, however, are usually assumed to be unaffected by alteration. I tested this assumption and the effects of alteration on the Macquarie Island glasses, by analyzing both fresh and altered glasses from GG. For the same unit (GN103) I analyzed fresh glass (GN103b, GN103d) and glass sampled from alteration haloes around dikes that intruded basalt pillows and hyaloclastites (GN103c). These analyses were compared, and if the variance of an element was within error between the samples, the element was considered to be unaffected by alteration.

Altered samples have very high water content, have lost SiO<sub>2</sub>, Al<sub>2</sub>O<sub>3</sub>, Na<sub>2</sub>O, K<sub>2</sub>O, and P<sub>2</sub>O<sub>5</sub>, and gained FeO CaO, and MgO (Table 3.1b, Figure 3.7), all consistent with alteration under high temperatures (150-200°C) and elevated water to rock ratios (~50-100), followed by retrograde zeolitization reactions (Alt, 1999). For example, the oldest section, HP, shows anomalously high MgO contents (14.6 to 19.38%; Table 3.1b), which is commonly associated with hydrothermal seafloor alteration. TiO<sub>2</sub> remained constant (Table 3.1b, Figure 3.11). Th, Nb, La, Pb, Zr, Hf, Yb, Lu, (Table 3.2i, Figures 3.3, 3.11) also remain constant in both the altered and fresh samples; all other trace elements appeared to have some mobility under these alteration conditions (Table 3.2i). It was therefore assumed that the same incompatible elements, trace elements and REEs that remained immobile in the GG section would also be unaffected at HP (where all glass samples were altered), and only the elements that remained immobile in this setting were considered below.

### **3.4 DISCUSSION**

#### **3.4.1 Geochemical trends**

Kamenetsky et al (2000) have reported more evolved (fractionated) compositions, with MgO as low as 5.6 wt% (Figures 3.7, 3.10), but none this low were measured in this study. This is a very wide range of MgO for a single suite of basalts (Kamenetsky et al., 2000). Macquarie Island volcanics are also characterized by a broad range of incompatible element enrichment, with (La/Sm)<sub>N</sub> (N=chondrite normalized) varying between 1.4 and 5.8 (Kamenetsky, 2000; Kamenetsky and Maas, 2002, Figure 3.10). My data are consistent with

previous studies; however, I also found more primitive (higher-MgO), strongly enriched glasses (Figure. 3.10). In the published database (Kamenetsky, 2000), there is an apparent relationship between MgO contents in the glass (index of fractionation) and the degree of enrichment in incompatible elements (e.g. (La/Sm)<sub>N</sub>, Figure 3.10) raising the possibility that the enriched characteristic of the basalts could have been caused during magma evolution within the lithosphere (via assimilation) rather than reflecting the composition of the asthenosphere (where magmas form). My data show that there are more primitive, but highly enriched basalts than previously recognized. Thus the correlation between the degrees of enrichment and fractionation that could be inferred from the data set of Kamenetsky et al. (2000) is eliminated, indicating that it is likely that the compositions of the glasses are reflecting original source melt compositions (Danyushevsky, pers. com.).

The data reveal a systematic relationship between incompatible element enrichment of the studied samples and their relative age as determined from structural and stratigraphic positions (Figure 3.3, 3.11) and described in section 3.3.1.1. In Figure 3.3, individual coherent sections have been arranged according to age (incorporating field and radiometric age data as described in section 3.3.1.1) and the incompatible element enrichment is shown by Nb/Zr. This ratio is commonly used to illustrate enrichment in the highly incompatible elements, as Nb is more highly incompatible than Zr. Thus a higher Nb/Zr indicates a higher enrichment in highly incompatible elements. (Average values for this ratio in primitive mantle, N-MORB and E-MORB are 0.06, 0.03, and 0.11, respectively,

from Sun and McDonough (1989), (Figure 3.10). In addition, these elements are thought to not be affected by fractionation or alteration (Einaudi et al., 2003; Pearce, 1983). I have used this ratio for these reasons, and because they both remained immobile in my altered samples whereas other commonly used incompatible element ratios did not. The same trends shown in Figure 3.3 are seen in almost all of the other incompatible trace elements measured in the Macquarie Island samples (Figure 3.11). Others could be used for illustrative purposes as well, but the known altered samples in the HP section would have to be excluded.

The oldest section, HP, shows a steady decline in incompatible element enrichment from youngest to oldest, as commonly seen in single eruptive cycles in Hawaii (Reiners, 2002) and the Costa Rica Ridge DSDP/ODP hole 504b (Einaudi et al., 2003), for example. Beginning with ML and BB, there is a period of striking variability in petrology and enrichment. At this time, both primitive picrites and evolved amphibole-bearing units were erupted and/or intruded with basalts of variable incompatible element enrichments, with Nb/Zr ratios ranging from 0.14 to 0.55. In contrast, the younger sections with more constant enrichment (GG, PP and AC) only range in Nb/Zr from 0.33-0.44, 0.25-0.35 and 0.16-0.27, respectively. Note that this trend toward less variability is coupled with a gradual decrease in the extent of enrichment in highly incompatible trace elements with age (Figure 3.3), with each successively younger section having a less enriched character than the previous.

### **3.4.2 Incompatible element enrichment**

Magnetic anomalies in the seafloor surrounding Macquarie Island (Wood et al., 1996, T. Meckel, C. G. Massell and W.R. Keller pers. comm.) indicate that spreading rates were slow to intermediate on the Macquarie spreading ridge prior to the transition to transform motion. E-MORBs on slow spreading ridges are believed to form by a low degree of melting of a mantle source that is deeper than the melt source predicted at fast spreading ridges; this degree of melting is controlled by the proportional relationship between mantle upwelling and conductive cooling (Niu and Hekinian, 1997). The Macquarie Island basalts are E-MORBs similar in composition to those observed at other slow to intermediate spreading ridges (Haase, 1996; Niu and Hekinian, 1997), which is consistent with published spreading rates. In contrast, peridotites on the island have high Cr-numbers, indicating that they have experienced a high degree of melting (Dick and Bullen, 1984; Hellebrand et al., 2001), which is not expected in slow- to medium spreading ridge environments. Thus, the E-MORBs exposed on the island were not generated by the same melting episode that created the peridotites (chapter 2). The relationship between the two units juxtaposed by the Finch-Langdon fault is addressed in the Summary and Model.

Structures on the island suggest that volcanism may have been sporadic, with spreading accommodated by alternating episodes of extensional faulting and volcanism. Evidence for periods with extensive faulting and lower magmatism include the exposure of the lower crust and upper mantle section in the northern part of the island that was exposed on the seafloor, and the associated thick talus

sequences at Bauer Bay which appear to have formed by shedding of rock from the uplifted fault scarp (chapter 1, Wertz et al., 2000a). Thus, discontinuous volcanism could be the sole explanation for the pattern of enrichment observed on Macquarie Island, caused by changes in the magmatic system in response to the changing tectonic regime; changes which could disrupt magma production, resulting in magmatism and extensional faulting alternating as the primary accommodation mechanisms for extension. For example, at times in this dynamic environment, conditions within the magmatic system might have enabled higher melt volume volcanism which would be less enriched in incompatible elements, alternating with periods of lower melt volume volcanism which would produce eruptions with higher incompatible trace element enrichment. Associated eruptions of variable enrichments like this have been sampled from the seafloor in areas of discontinuous volcanism (le Roex et al., 1992) and in the vicinity of seamounts (Niu and Batiza, 1997; Niu et al., 2002) where the discontinuity in melt production may cause small batches of individual melts to form under different conditions, giving them their diverse compositions, in contrast to the high volume, evolved melts produced in robust, long-lived magmatic systems.

On Macquarie Island, the HP eruption could represent a period of higher-volume volcanism, with its relatively less-enriched compositions, that show a steady decrease in incompatible element enrichment with time. Beginning with eruption of the ML and BB sections, the eruption pattern changes, with lavas of variable compositions erupted. This variability suggests that at this time, small melt batches with diverse incompatible element enrichment were developed that

did not mix with each other in the magmatic system, retaining their initial compositions. Alternately, small melt fractions could have been sampled from different levels within a chemically stratified magma chamber; however, well-developed magma chambers are not generally believed to be associated with E-MORB volcanism. The isolation of different melt fractions in both cases would lead to eruptions of relatively enriched basalts alternating with less enriched basalts (Kamenetsky and Maas, 2002). As the magmatic system matured, more melt was produced, the magmatic chambers became more complex, and the residence time of these melts increased, allowing the individual primary melts to mix, leading to more constant basalt compositions and/or decreased enrichment in incompatible trace elements (Reiners, 2002) as observed in the youngest sections, GG, PP and AC. AC still has slightly more variable compositions with one anomalously depleted sample, and may represent a new cycle (similar to ML and BB) in this dynamic eruptive system. New age dates may show this eruptive sequence is more similar in age to the BB sequence, as mentioned in the Geology section. Regardless, the interpretation would not be altered appreciably. The overall decrease in enrichment from ML to AC is also consistent with an increase in melt production. This increase is commonly interpreted to be related to an acceleration of spreading rate (Niu and Hekinian, 1997).

### **3.4.3 Evidence of ridge propagation?**

Although sporadic volcanism and changing spreading rates can explain the diversity in the basaltic glass compositions, they do not address the unusual association of picrites and amphibole-bearing basalts. A more specific tectonic

explanation for the diversity in the Macquarie Island basalt composition that does include these two unusual rock types may be magmatism related to ridge propagation. Volcanism within propagating ridges varies with distance from the propagating ridge (PR) tip, variability caused by the inter-related tectonic, temperature and pressure regimes along the axis. The following presents the model proposed by Christie and Sinton, (1981) that explains the variability of basalt compositions in this environment. Stage 1: In front of the PR tip, deep earthquakes have been recorded that suggest that melting and deep intrusion begins in this region. Stage 2: Rifting progresses and the isotherms rise, initiating the first eruptions at the ridge tip, which are primitive in composition, produced from a deep source. Within 2-3 km from the PR tip, a shallow region develops that may allow rapid fractionation of magmas in small isolated batches, which are erupted alongside the primitive magmas, resulting in bimodal volcanism. Melts are produced in small, ephemeral magma bodies. Stage 3: Between 5-30 km behind the tip, there is a transition from the few small, ephemeral magma bodies to multiple magma bodies, which increase the residence time of the melts and the opportunity for fractionation. Melt production increases at this point, and the greatest variety of compositions are seen, from most to least fractionated. In the beginning of this stage, the individual magma bodies are isolated, preserving the diversity of magma compositions, but with time they become more connected, reducing the diversity, allowing the individual melts to mix. Stage 4: As the magma bodies become increasingly interconnected, fewer highly fractionated magmas are developed, as the higher volume of magma production would

encourage mixing with other melts and/or rapid eruption (Christie and Sinton, 1981). Overall, the increasing melt production would result in a decrease in incompatible element enrichment with time.

Bimodal eruptions with highly evolved lavas associated with highly primitive lavas (such as the association of evolved amphibole-bearing units that are associated with primitive picrites on Macquarie Island) are not usually found in normal spreading environments. Amphibole-bearing basalts sampled at mid-ocean ridges are very rare, but have been recovered from the Jan Mayen platform in the Norwegian-Greenland Sea. In that location, it has been proposed that volcanism has been caused by a northward propagating spreading axis (Haase, 1994); however, the relationship between volcanism and tectonism in this area are still not well understood (Haase, 1996). Extreme cases of bimodal eruptions, like those on Macquarie Island, occur in the vicinity of propagating ridge tips (Christie and Sinton, 1981, 1986) and early rift zones (Lahitte, 2003; Thompson, 1994). With distance from the ridge tip as propagation progresses, basalt compositions approach compositions similar to the main ridge (Sinton et al., 1983) as discussed in the previous paragraph. Thus another possible explanation for the variable enrichments in the basaltic glass on Macquarie Island, which also explains the presence of unusual picrites and amphibole-bearing basalts, is propagation of a ridge tip into preexisting oceanic lithosphere as ridge segments become unstable during plate reorganization.

To explain the complex enrichment pattern of the Macquarie Island basalts and bimodal volcanism, I propose the following model: The oldest section (HP) is

the most altered and has a very different enrichment pattern from the rest of the sections, suggesting that it may be the expression of steady-state, older magmatism. At a later time, the changing spreading direction could have caused individual spreading segments to become unstable and to begin to propagate into neighboring older crust to alleviate this instability. The initial phase of propagation would be recorded in the ML section, the associated picrites and amphibole bearing units, and the BB and possibly the AC sections of variable compositions. The more constant compositions of lavas (GG and PP) would have been erupted as the propagating tip continued to migrate, the magmatic system developed and individual magma bodies became more interconnected, allowing them to mix, similar to the transition zone in propagating rift settings (Christie and Sinton, 1981; Haase et al., 2000). This increase in mixing would also explain the decrease in variance of incompatible element enrichment with time over the entire basalt collection. In addition, more melt is produced in this later period, which would cause an overall decrease in incompatible elements with time.

### **3.5 CONCLUSIONS**

This study combines basalt geochemistry with spatial and temporal information provided by the stratigraphic/structural positions of the basalts analyzed and builds on previous studies of the Macquarie Island basalts (Kamenetsky, 2000; Kamenetsky and Maas, 2002). The basalts were erupted in the final stages of seafloor spreading at ~6 Ma. Enriched basalts show incompatible element trends indicating periods of alternating enriched and less-enriched eruptions followed by periods of relatively constant compositions. The

entire series shows a progressive decrease in enrichment with age. These patterns of enrichment and diversity of basalt types (including picrites and amphibole-bearing basalts) may be evidence of ridge propagation caused by adjustments to accommodate a changing spreading direction.

Seafloor geophysical data around Macquarie Island show that the individual spreading segments became shorter and their numbers became fewer in the later stages of spreading, evidenced by the associated fracture zones becoming closer together as they approach the plate boundary (Figure 1.2, Massell et al., 2000; Massell and Mosher, in press). This pattern could have been produced by propagation of individual ridges/segment tips in response to the changing spreading direction. Thus, from the seafloor structures, it would be expected that ridge propagation was active near the end of spreading on the Australian-Pacific plate boundary; the geochemistry of the basalts is compatible with this prediction.

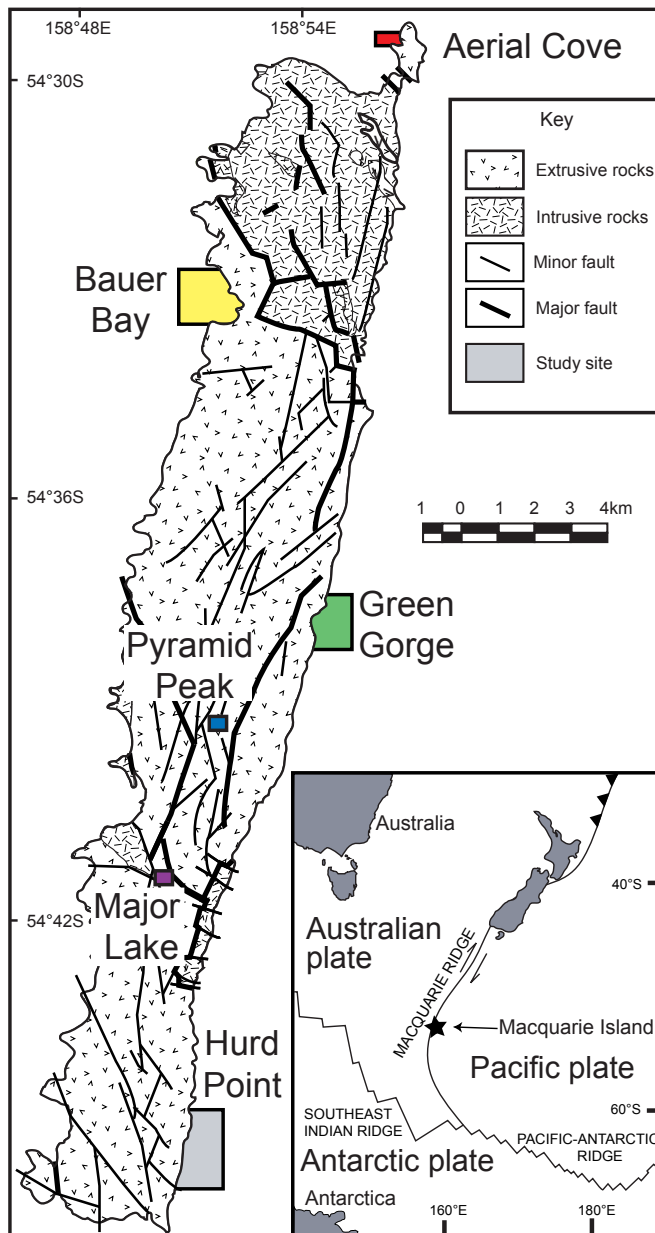


Figure 3.1. Simplified geologic map of Macquarie Island after Goscombe and Everard (1998). The island is a complete section of ocean crust that formed near the end of spreading on the paleo-Macquarie spreading ridge. Colored shaded boxes mark six sites included in this study to determine geochemical changes in erupted lavas with time, colors correspond to color groups in the following figures. Inset- Macquarie Island location on the Australian-Pacific Plate boundary.

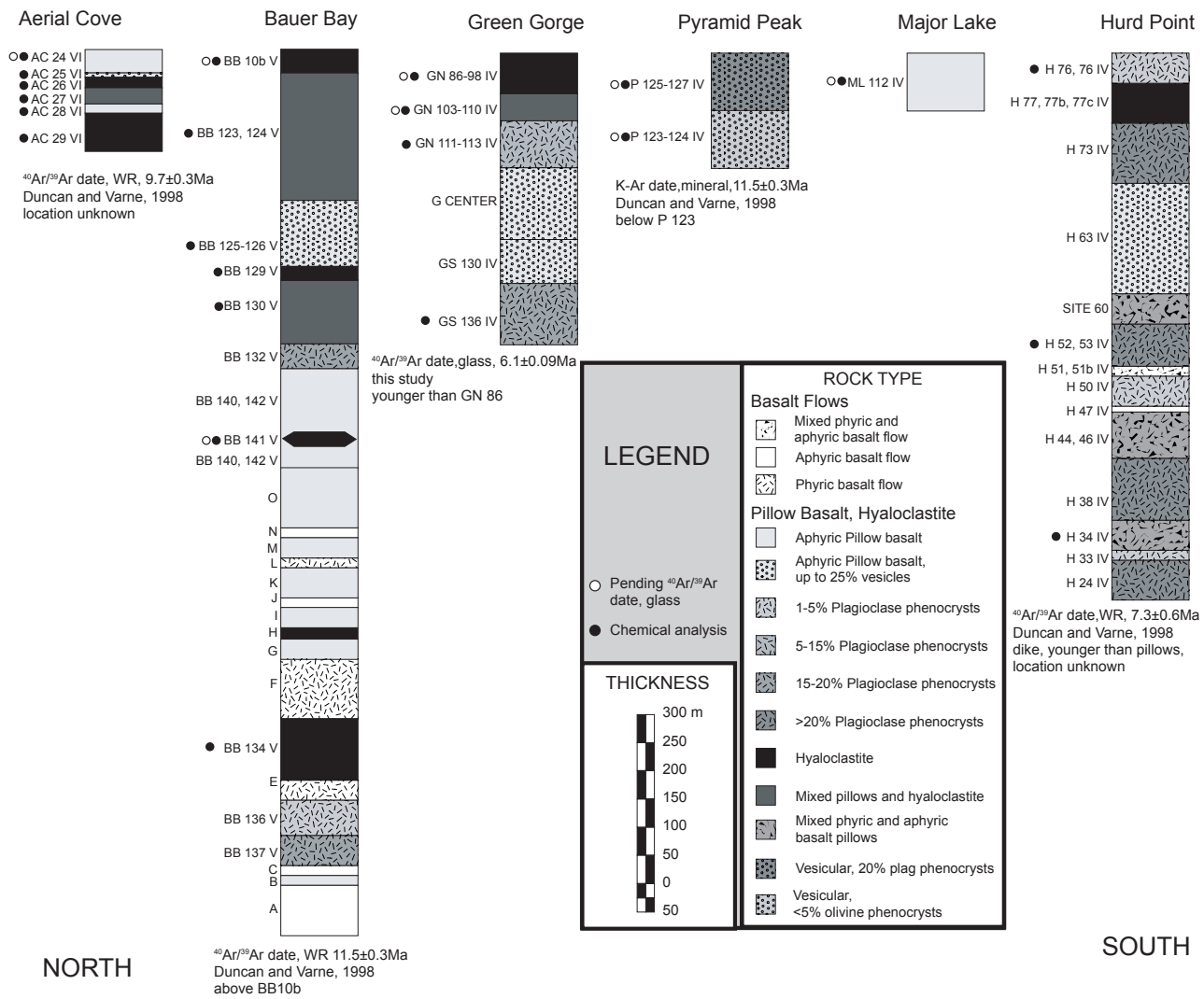


Figure 3.2. Stratigraphic columns of Macquarie Island basalts based on field work (this study). Age was determined within each section (e.g., BB, HP, etc.) using direct field relationships.

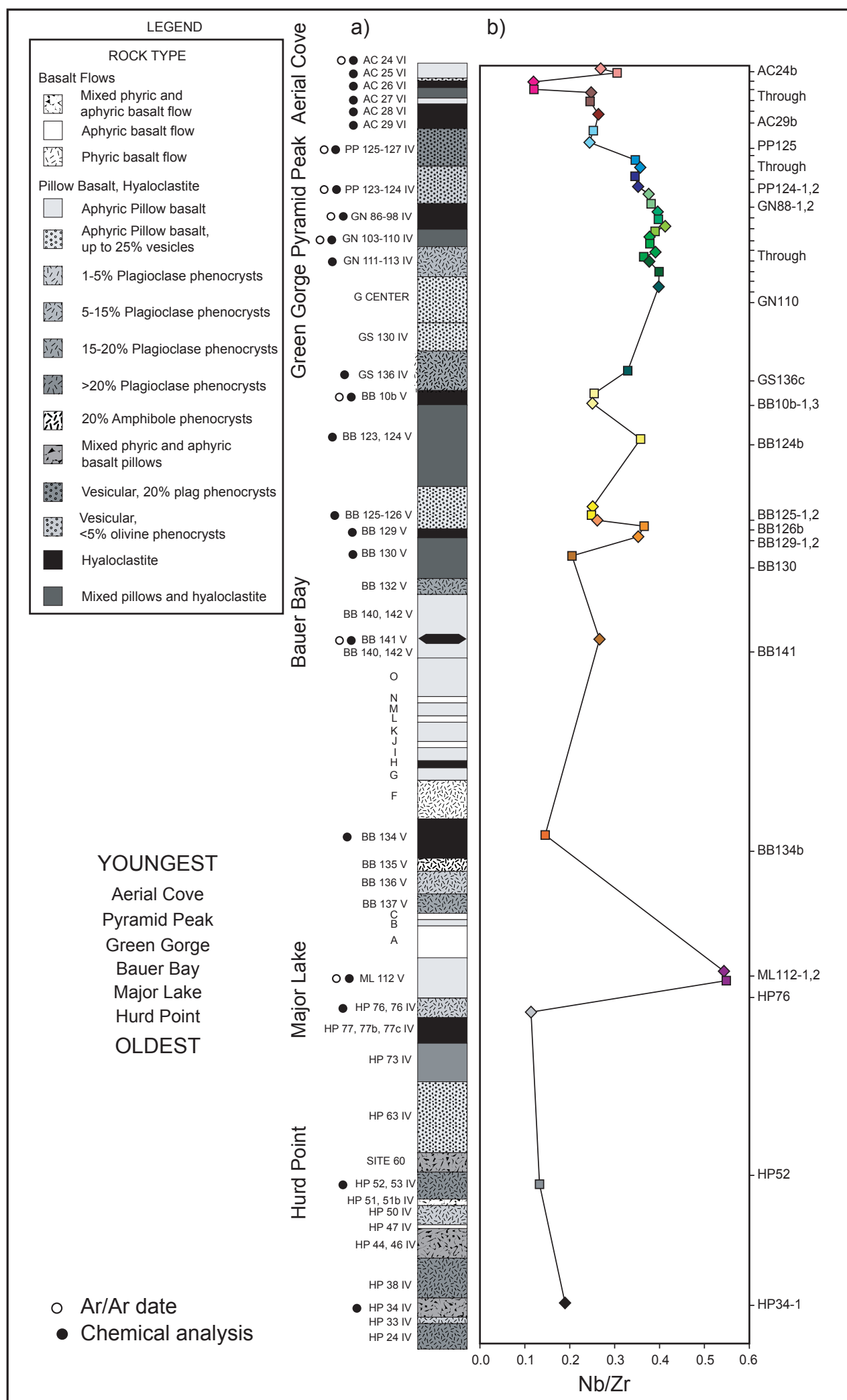


Figure 3.3. Stratigraphic columns. Relative age between sections determined using radiometric ages, plate tectonic reconstructions and geographic locations, degrees of alteration and topographic position (see Figure 3.2 and text for discussion). Relative enrichment in highly incompatible elements Nb/Zr in the Macquarie Island basalts. Column shows individual samples arranged according to apparent age, youngest at the top. The oldest section shows a steady decline in incompatible element concentration with time. The next section has variable compositions, with the youngest sections showing less variability. The magnitude of variability and overall enrichment decreases with time from ML to AC.

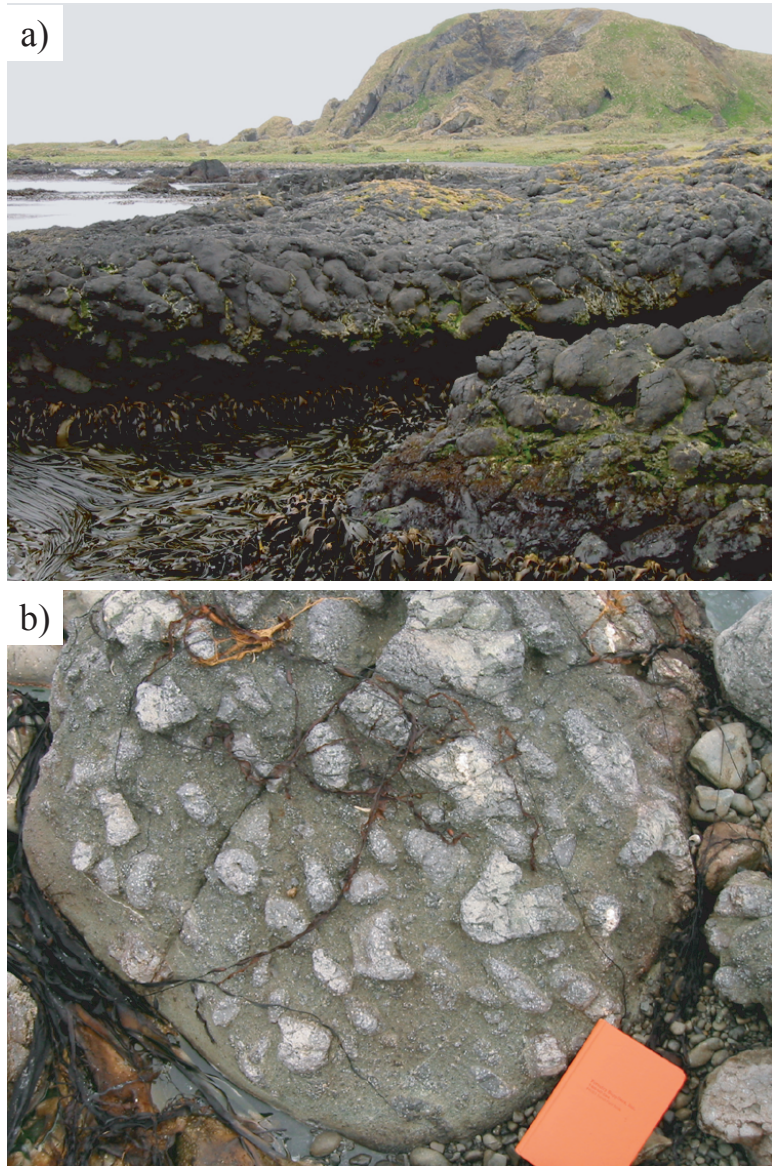


Figure 3.4. Pillow basalt, hyaloclastite a) Well-formed pillow basalts on Douglas Point. View to north. b) Weathered hyaloclastite surface, north side of Bauer Bay, view to NW. Basalt clasts are surrounded by glass matrix.



Figure 3.5. Pillow-rich hyaloclastite at south side of Bauer Bay.

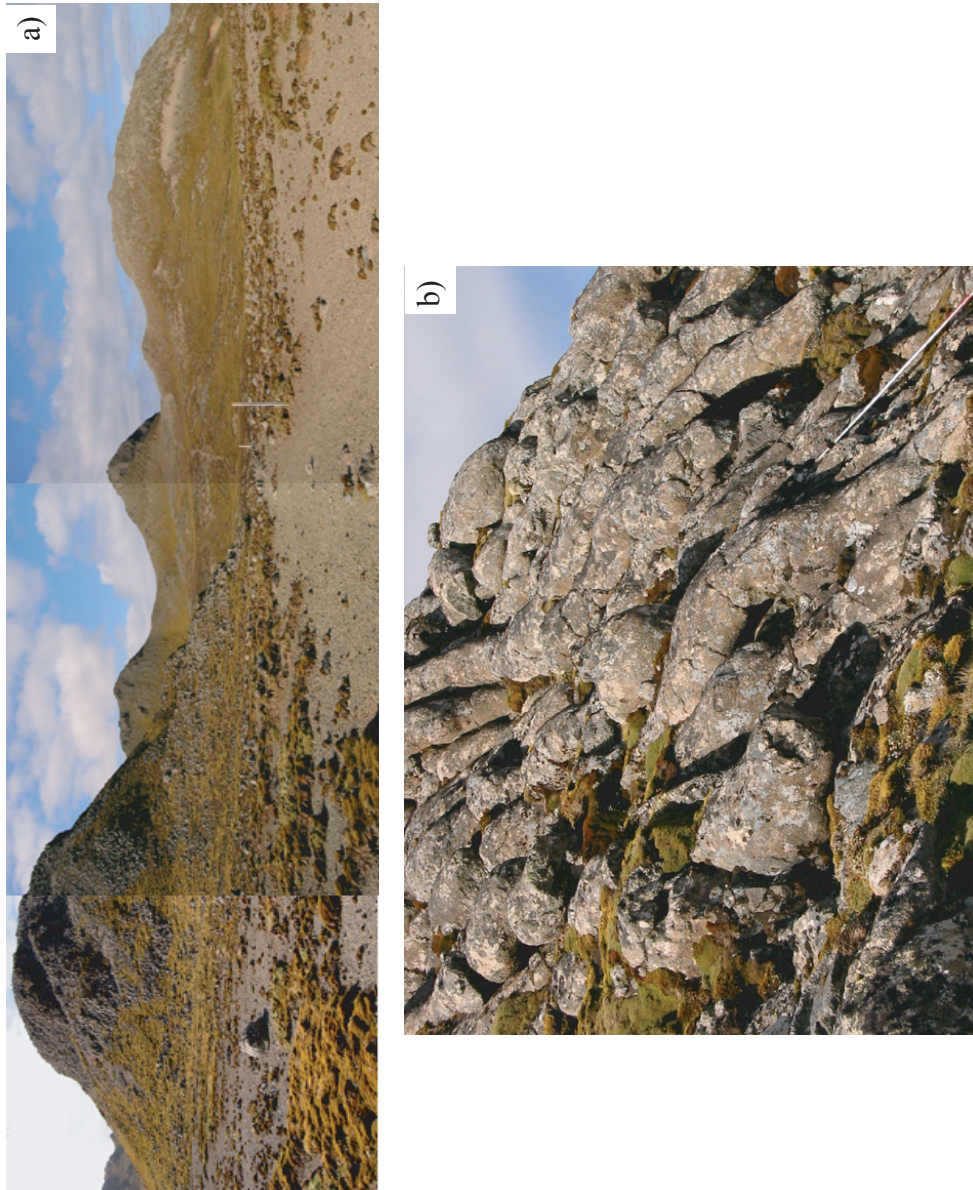


Figure 3.6. a) Preserved submarine volcanoes at Pyramid Peak. Track-mark stakes are ~1 m tall. Pyramid Peak is the second mountain from right. View to north. b) Close-up view of radial pillow tubes on the south side of the first peak from left. View to northeast.

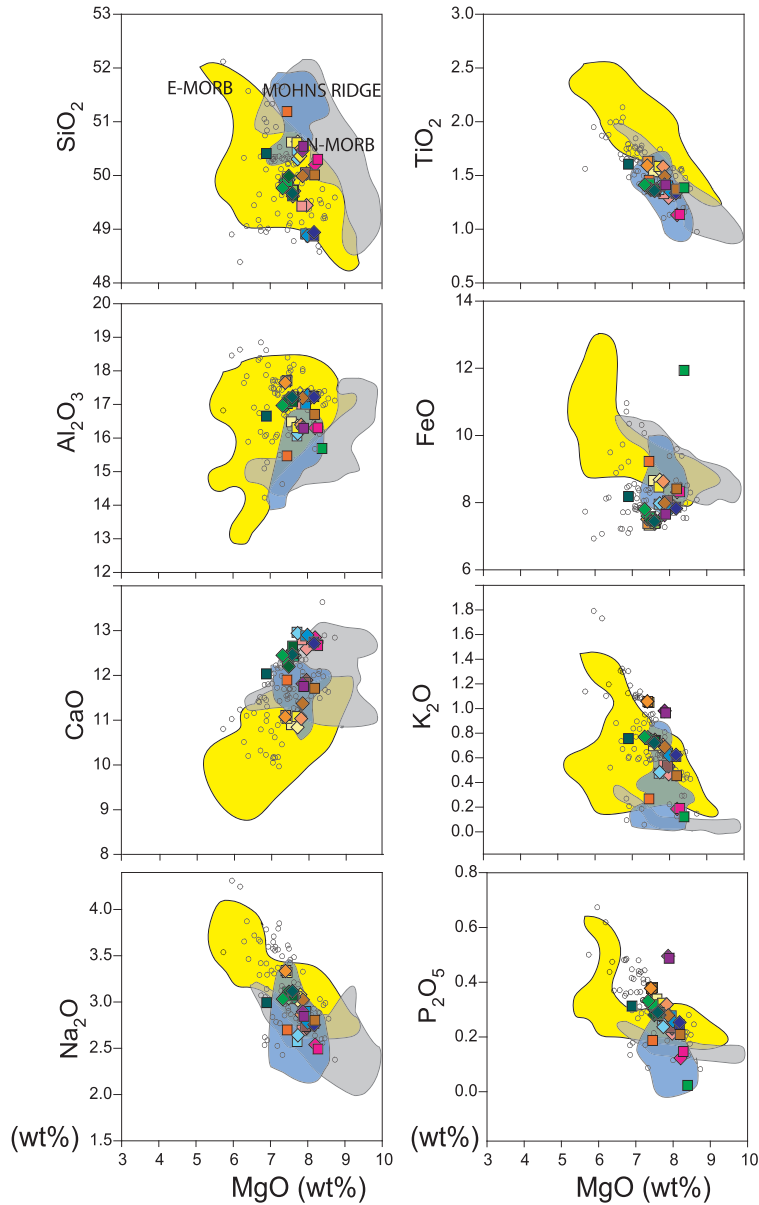


Figure 3.7. Major element vs. MgO variation diagrams (wt%) for MI basaltic glass. Colored symbols correspond to Figure 3.3. Open circles are MI data, Kamenetsky et al., 2000. Grey field is range of N-MORB, yellow is range of E-MORB, (from the EPR). Data from Niu (1997, 2000). Blue field is range of Mohns Ridge (Haase, 1996). All data are normalized to 100%, anhydrous. Anomalous green square is altered GN103c sample, which plots off the shown scale for CaO, SiO<sub>2</sub>, Na<sub>2</sub>O. See Table 3.1b for original analysis values.

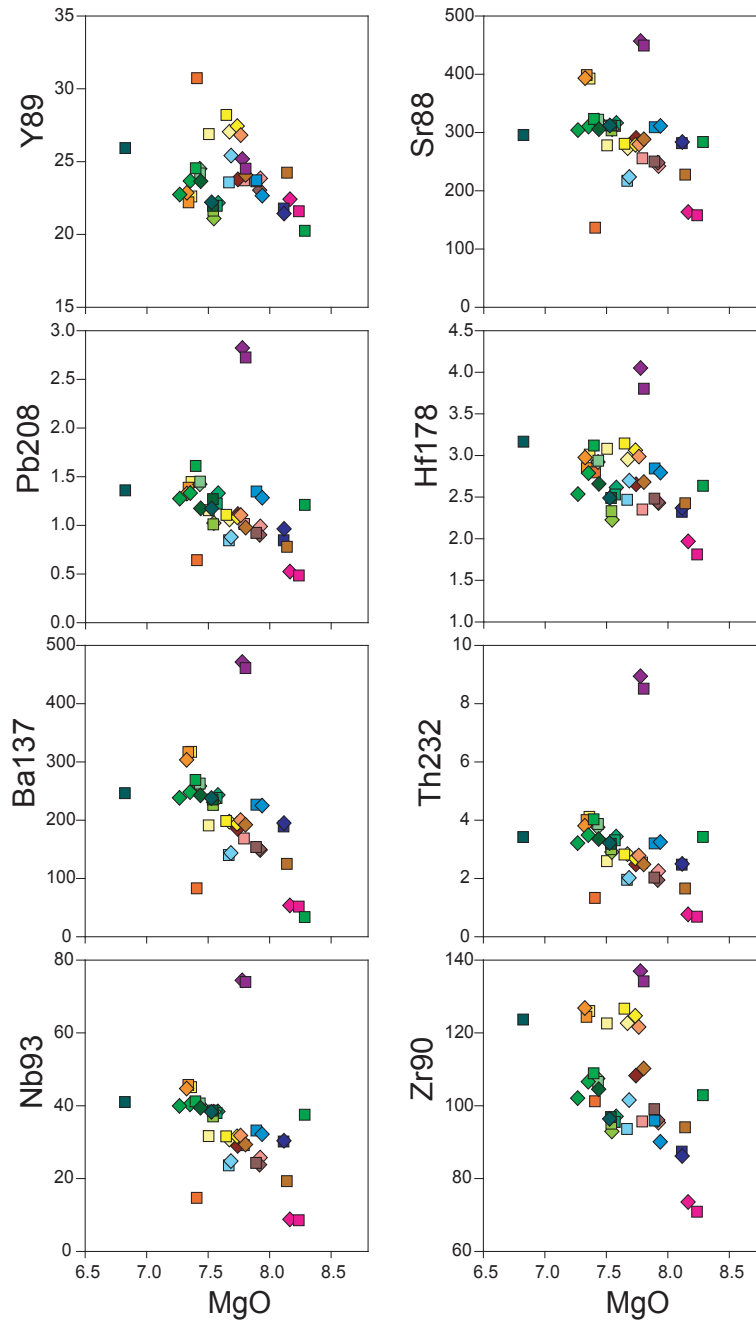


Figure 3.8. Trace element (ppm) vs. MgO (wt%) variation diagrams for MI basaltic glass. Colored symbols correspond to Figure 3.3. Anomalous green square is altered GN103c sample with high MgO, value should be disregarded in elements that are affected by alteration; see text for discussion.

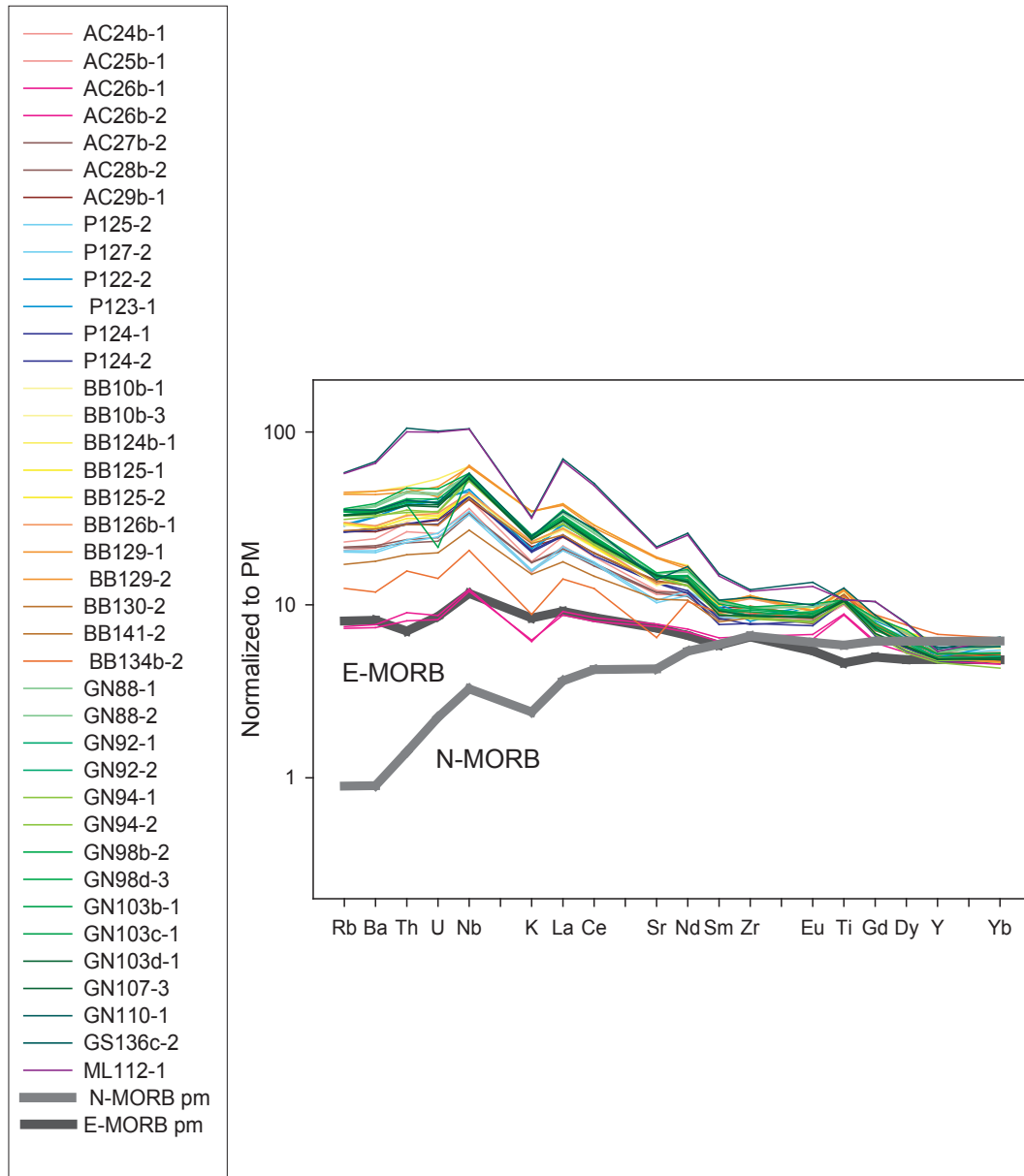


Figure 3.9. Macquarie Island trace element analyses. Normalized to primitive mantle (PM). All samples are enriched in highly incompatible elements relative to N-MORB, and are highly enriched for E-MORB. Sample colors correspond to Figure 3.3. PM, N-MORB and E-MORB values from Sun and McDonough (1989).

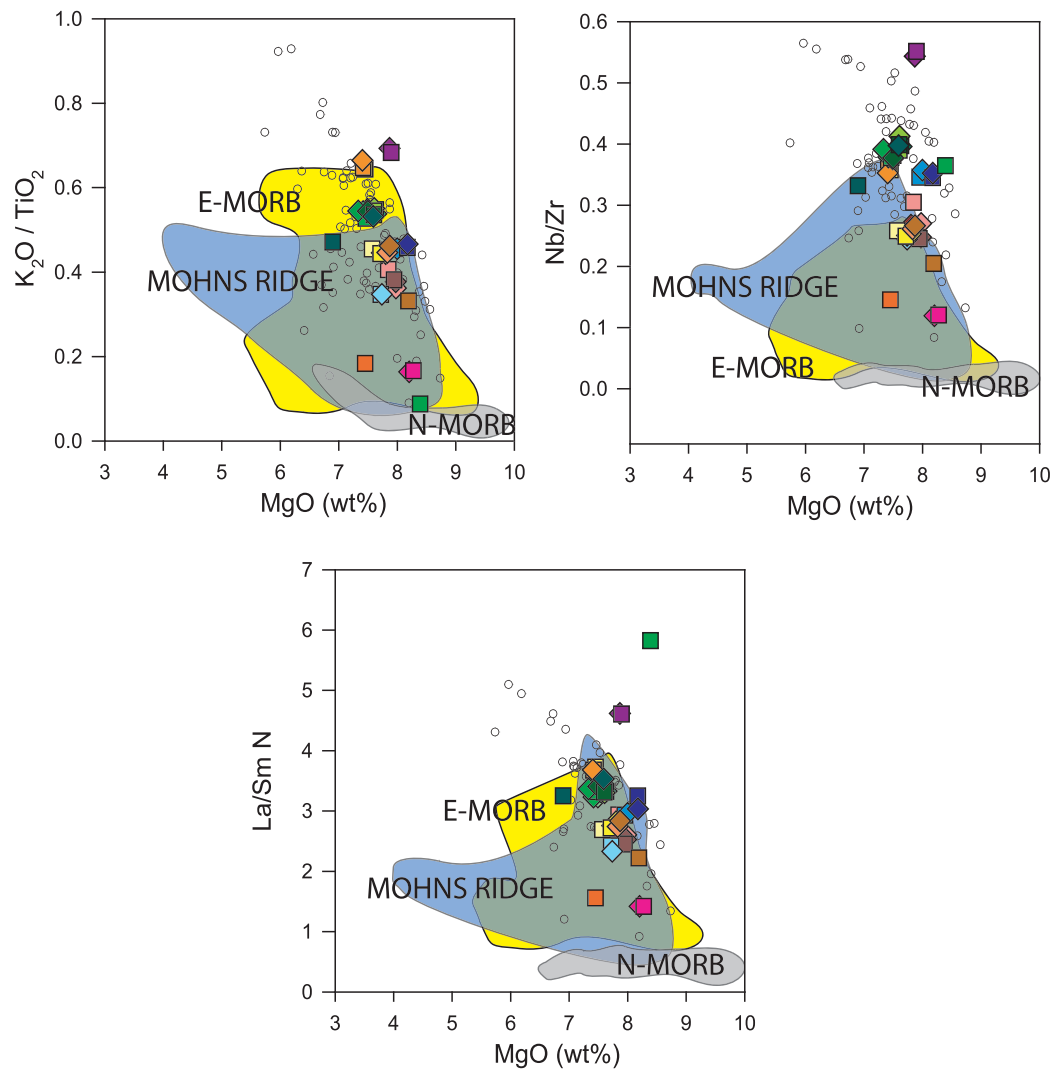
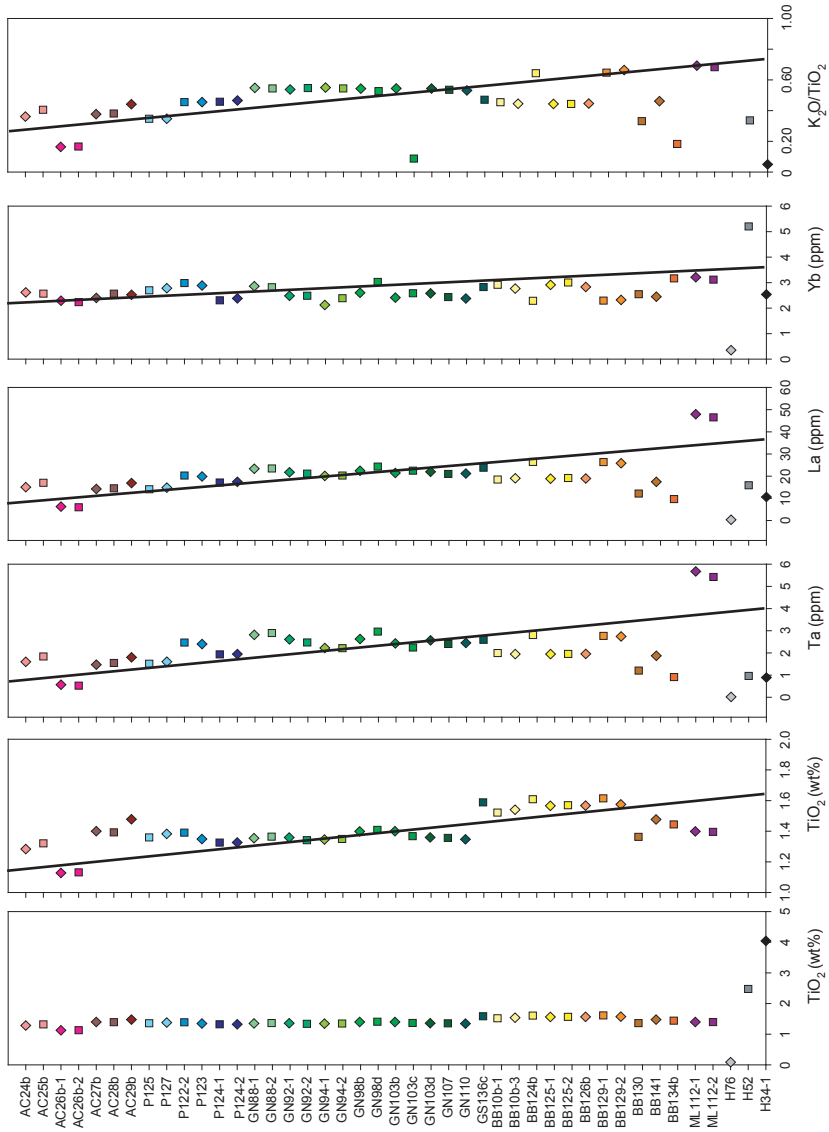


Figure 3.10. Degree of fractionation vs. degree of enrichment in incompatible elements. Open circles are Macquarie Island data from Kamenetsky et al. (2000) colored symbols correspond to Figure 3.2. N-MORB is gray field, Yellow is E-MORB. MORB data from Niu (1997, 2000). Blue field is range of Mohns Ridge (Haase, 1996). All Macquarie Island basalts are relatively primitive and enriched in incompatible elements. This study found more primitive, highly enriched basalts than Kamenetsky et al, (2000) eliminating the relationship between fractionation and enrichment. Colored symbols correspond to Figure 3.3. Anomalous green square is altered GN103c sample, value should be disregarded.

Figure 3.11. Selected incompatible element columns. Titanium is shown at two scales to include H samples in view, and also show variability in other sections. Variability patterns similar to Figure 3.3 are seen in other incompatible elements. Note  $K_2O$  is affected by alteration, thus anomalous values for H and GN103c samples in the  $K_2O/TiO_2$  plot should be disregarded. Black lines illustrate decrease in enrichment trends.



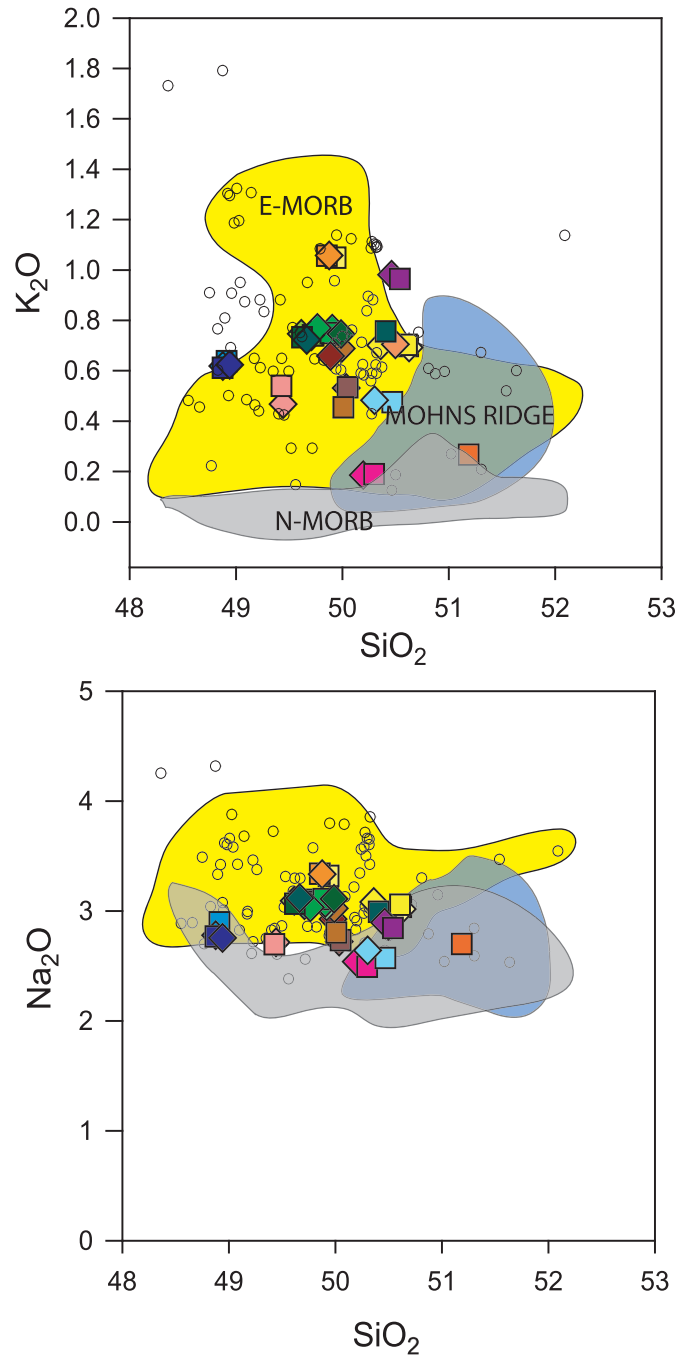


Figure 3.12. Alkali and silica contents (wt%) of Macquarie Island basalts. All basalts have alkalic compositions.

Table 3.1a Electron microprobe major element data, S, Cl, H<sub>2</sub>O (wt%) of Macquarie Island basaltic glass.

Sample	SiO <sub>2</sub>	TiO <sub>2</sub>	Al <sub>2</sub> O <sub>3</sub>	FEO	MnO	MgO	CaO	Na <sub>2</sub> O	K <sub>2</sub> O	P <sub>2</sub> O <sub>5</sub>	Cr <sub>2</sub> O <sub>3</sub>	S	Cl	H <sub>2</sub> O	Total	Mg#
AC24b-1	49.3	1.29	17.09	8.00	0.14	7.96	12.57	2.71	0.47	0.21	0.05	0.09	0.03	0.51	100.5	0.67
AC25b-1	49.2	1.33	16.95	7.92	0.16	7.82	12.75	2.69	0.54	0.25	0.04	0.09	0.04	0.54	100.3	0.67
AC26b-1	50.1	1.13	16.27	8.30	0.16	8.19	12.82	2.53	0.19	0.12	0.06	0.10	0.01	0.28	100.3	0.67
AC26b-2	50.3	1.14	16.31	8.32	0.17	8.27	12.67	2.49	0.19	0.15	0.05	0.11	0.01	0.28	100.5	0.67
AC27b-2	49.9	1.41	17.01	7.93	0.18	7.95	11.85	2.71	0.53	0.23	0.05	0.10	0.03	0.53	100.4	0.67
AC28b-2	50.0	1.40	17.03	8.05	0.16	7.94	11.84	2.73	0.53	0.24	0.04	0.10	0.03	0.52	100.6	0.67
AC29b-2	49.7	1.48	17.34	7.96	0.14	7.76	11.24	2.91	0.65	0.25	0.06	0.09	0.04	0.60	100.2	0.66
ML112-1	50.3	1.41	16.24	7.60	0.13	7.83	11.76	2.88	0.98	0.49	0.05	0.09	0.10	0.97	100.8	0.68
ML112-2	50.3	1.40	16.21	7.62	0.16	7.85	11.69	2.83	0.96	0.49	0.04	0.08	0.10	0.99	100.7	0.68
P122-2	48.8	1.40	16.99	7.85	0.17	7.94	12.86	2.89	0.64	0.28	0.06	0.10	0.04	0.56	100.6	0.67
P123-1	48.8	1.36	17.24	7.77	0.15	7.98	12.87	2.77	0.62	0.26	0.05	0.10	0.04	0.55	100.5	0.68
P124-1	48.9	1.34	17.24	7.87	0.15	8.17	12.75	2.77	0.61	0.24	0.05	0.09	0.04	0.55	100.8	0.68
P124-2	48.8	1.33	17.18	7.81	0.16	8.16	12.68	2.75	0.62	0.25	0.05	0.10	0.04	0.55	100.5	0.68
P125-2	50.4	1.37	16.04	7.94	0.17	7.70	12.94	2.57	0.47	0.25	0.05	0.09	0.03	0.48	100.5	0.66
P127-2	50.3	1.39	16.15	7.98	0.16	7.74	12.95	2.64	0.48	0.24	0.04	0.10	0.03	0.51	100.7	0.66
BB10b-1	50.3	1.52	16.37	8.60	0.16	7.52	10.83	3.02	0.69	0.34	0.05	0.10	0.05	0.70	100.2	0.64
BB10b-3	50.4	1.55	16.28	8.64	0.19	7.70	10.79	3.00	0.69	0.30	0.04	0.10	0.05	0.70	100.4	0.64
BB124b-1	49.6	1.62	17.58	7.28	0.15	7.39	10.96	3.29	1.04	0.38	0.02	0.09	0.07	1.06	100.5	0.67
BB125-1	49.9	1.56	16.19	8.48	0.16	7.73	10.98	3.05	0.69	0.31	0.04	0.11	0.05	0.71	99.9	0.65
BB125-2	50.2	1.57	16.17	8.39	0.15	7.65	10.98	3.03	0.70	0.32	0.05	0.10	0.05	0.73	100.1	0.65
BB126b-1	50.2	1.57	16.31	8.58	0.15	7.79	10.98	2.85	0.70	0.32	0.04	0.10	0.05	0.69	100.4	0.65
BB129-1	49.4	1.62	17.52	7.32	0.16	7.35	11.01	3.31	1.05	0.37	0.03	0.08	0.07	0.91	100.2	0.67
BB129-2	49.5	1.58	17.51	7.44	0.13	7.34	10.98	3.31	1.05	0.37	0.03	0.08	0.07	0.91	100.3	0.67
BB130-2	50.0	1.37	16.70	8.41	0.14	8.19	11.71	2.80	0.45	0.21	0.04	0.10	0.03	0.48	100.6	0.66
BB141-2	49.7	1.48	17.09	7.94	0.11	7.82	11.30	3.00	0.68	0.28	0.05	0.09	0.04	0.68	100.3	0.67
BB134b-2	51.2	1.45	15.47	9.23	0.16	7.45	11.90	2.70	0.27	0.19	0.05	0.12	0.02	0.44	100.6	0.62

Table 3.1b Electron microprobe major element data, S, Cl, H<sub>2</sub>O (wt%) of Macquarie Island basaltic glass. Note: blanks indicate altered samples with H<sub>2</sub>O contents too high to be recalculated accurately.

Sample	SiO <sub>2</sub>	TiO <sub>2</sub>	Al <sub>2</sub> O <sub>3</sub>	FeO	MnO	MgO	CaO	Na <sub>2</sub> O	K <sub>2</sub> O	P <sub>2</sub> O <sub>5</sub>	Cr <sub>2</sub> O <sub>3</sub>	S	Cl	H <sub>2</sub> O	Total	Mg#
GN88-1	49.5	1.36	16.95	7.40	0.14	7.43	12.35	3.02	0.74	0.30	0.03	0.07	0.05	0.67	100.0	0.67
GN88-2	49.6	1.37	17.06	7.56	0.13	7.47	12.33	3.09	0.75	0.30	0.04	0.09	0.05	0.69	100.6	0.67
GN92-1	49.6	1.37	17.11	7.44	0.16	7.63	12.43	3.05	0.74	0.28	0.04	0.08	0.05	0.67	100.6	0.68
GN92-2	49.4	1.35	17.13	7.36	0.13	7.59	12.36	3.06	0.74	0.29	0.03	0.09	0.05	0.67	100.3	0.68
GN98b-1	49.4	1.40	16.80	7.52	0.16	7.34	12.26	3.04	0.76	0.31	0.04	0.08	0.06	0.70	99.9	0.67
GN98d-3	49.5	1.41	16.90	7.51	0.11	7.41	12.25	3.08	0.74	0.32	0.05	0.08	0.05	0.71	100.2	0.67
GN103b-1	48.1	1.38	16.41	7.47	0.17	7.11	12.31	2.90	0.75	0.31	0.04	0.08	0.05	0.70	97.8	0.66
GN103b-1b	48.3	1.37	16.47	7.57	0.14	7.11	12.08	2.94	0.75	0.32	0.06	0.08	0.05	0.70	97.9	0.66
GN103d-1	50.1	1.37	17.22	7.49	0.16	7.52	12.23	3.12	0.75	0.28	0.03	0.08	0.05	0.68	101.1	0.67
GN107-3	49.2	1.36	16.94	7.40	0.13	7.54	12.55	3.04	0.73	0.28	0.04	0.08	0.05	0.66	100.0	0.67
GN110-1	49.7	1.36	17.22	7.44	0.14	7.59	12.46	3.12	0.72	0.29	0.04	0.09	0.05	0.69	100.9	0.67
GS136c-2	50.0	1.59	16.50	8.11	0.16	6.83	11.93	2.97	0.75	0.31	0.04	0.10	0.05	0.89	100.2	0.63
ALTERED																
Sample	SiO <sub>2</sub>	TiO <sub>2</sub>	Al <sub>2</sub> O <sub>3</sub>	FeO	MnO	MgO	CaO	Na <sub>2</sub> O	K <sub>2</sub> O	P <sub>2</sub> O <sub>5</sub>	Cr <sub>2</sub> O <sub>3</sub>	S	Cl	H <sub>2</sub> O	Total	Mg#
H34-1	42.3	1.54	11.83	12.60	0.42	19.83	3.46	0.06	0.15	0.24	0.06	0.02	0.01		92.5	0.63
H34-1	40.6	3.80	11.92	11.96	0.40	17.24	6.12	0.11	0.19	0.53	0.07	0.03	0.01		93.0	0.63
H76	38.4	0.08	13.39	18.76	0.14	18.01	0.85	0.03	0.26	0.02	0.04	0.03	0.02		90.0	0.63
H52	41.5	2.32	12.68	15.25	0.16	14.60	4.64	0.16	0.78	0.47	0.06	0.04	0.02		92.7	0.63
GN94-1	49.3	1.35	17.14	7.33	0.13	7.56	12.48	3.07	0.74	0.29	0.04	0.09	0.05		99.6	0.63
GN94-2	49.2	1.35	17.04	7.30	0.13	7.52	12.36	3.05	0.73	0.28	0.05	0.09	0.05		99.1	0.63
GN103c-1	40.4	1.27	14.42	10.97	0.09	7.71	16.80	0.10	0.11	0.02	0.03	0.10	0.02		92.1	0.63
GN103c-2	41.0	0.82	14.75	11.42	0.11	7.89	16.13	0.14	0.07	0.01	0.03	0.10	0.01		92.5	0.63
GN88-1	49.5	1.36	16.95	7.40	0.14	7.43	12.35	3.02	0.74	0.30	0.03	0.07	0.05	0.67	100.0	0.67
GN88-2	49.6	1.37	17.06	7.56	0.13	7.47	12.33	3.09	0.75	0.30	0.04	0.09	0.05	0.69	100.6	0.67
GN92-1	49.6	1.37	17.11	7.44	0.16	7.63	12.43	3.05	0.74	0.28	0.04	0.08	0.05	0.67	100.6	0.68
GN92-2	49.4	1.35	17.13	7.36	0.13	7.59	12.36	3.06	0.74	0.29	0.03	0.09	0.05	0.67	100.3	0.68

Table 3.2a ICP-MS trace element data (ppm) of Macquarie Island basaltic glass.

	AC24b- 1	±	AC25b- 1	±	AC26b- 1	±	AC26b- 2	±
Rb85	13.0	0.10	14.4	0.12	4.7	0.06	4.6	0.06
Ba137	148.8	0.99	168.7	1.27	53.7	0.50	51.6	0.59
Th232	2.3	0.04	2.5	0.04	0.8	0.02	0.7	0.02
U238	0.5	0.01	0.6	0.02	0.2	0.01	0.2	0.01
Nb93	25.8	0.18	29.2	0.19	8.8	0.09	8.5	0.08
Ta181	1.6	0.03	1.8	0.03	0.6	0.02	0.5	0.01
La139	15.0	0.11	17.0	0.12	6.3	0.07	6.0	0.07
Ce140	30.9	0.17	33.6	0.20	14.9	0.12	14.2	0.11
Pb208	1.0	0.03	1.0	0.03	0.5	0.02	0.5	0.02
Sr88	242.3	1.26	255.6	1.64	163.5	1.13	157.9	1.16
Nd146	15.5	0.18	15.8	0.22	9.8	0.15	9.4	0.16
Sm147	3.7	0.10	3.7	0.09	2.9	0.08	2.7	0.07
Zr90	95.4	0.68	95.7	0.61	73.6	0.44	70.9	0.48
Hf178	2.4	0.05	2.4	0.06	2.0	0.06	1.8	0.04
Eu151	1.3	0.03	1.4	0.03	1.1	0.03	1.1	0.03
Gd157	4.2	0.10	4.3	0.09	3.7	0.10	3.6	0.11
Dy163	4.5	0.08	4.4	0.08	4.2	0.07	3.9	0.08
Li	4.9	0.04	4.8	0.04	4.5	0.04	4.4	0.04
Y89	23.8	0.16	23.7	0.17	22.4	0.16	21.6	0.16
Er166	2.7	0.04	2.6	0.05	2.5	0.05	2.4	0.06
Yb173	2.6	0.08	2.6	0.07	2.3	0.07	2.2	0.06
Lu175	0.4	0.01	0.4	0.01	0.4	0.01	0.3	0.01
Sc45	35.4	0.26	37.3	0.27	40.2	0.31	39.3	0.24
Be9	0.7	0.05	0.7	0.05	0.5	0.03	0.5	0.04
B10	9.9	0.27	8.6	0.26	8.1	0.31	9.7	0.30
B11	9.7	0.14	8.4	0.13	7.8	0.14	9.9	0.16
Ca43	12.5	0.06	12.7	0.08	12.8	0.08	12.6	0.08
Co59	39.6	0.29	38.7	0.25	42.8	0.30	43.0	0.30
Ni60	120.2	1.03	107.8	0.86	122.3	1.17	124.5	1.02
Cu65	115.4	1.00	119.4	1.03	132.3	1.20	134.3	1.22
Zn66	54.5	0.58	52.0	0.66	54.3	0.66	54.6	0.57

Table 3.2b ICP-MS trace element data (ppm) of Macquarie Island basaltic glass.

	AC27b- 2	±	AC28b- 2	±	AC29b- 1	±	P125-2	±
Rb85	13.3	0.13	13.5	0.15	16.6	0.14	12.6	0.11
Ba137	150.4	1.44	153.8	1.47	184.9	1.39	140.2	1.39
Th232	1.9	0.03	2.0	0.04	2.5	0.04	2.0	0.04
U238	0.5	0.01	0.5	0.02	0.6	0.02	0.5	0.01
Nb93	23.8	0.22	24.3	0.22	29.0	0.27	23.6	0.19
Ta181	1.5	0.03	1.5	0.03	1.8	0.03	1.5	0.03
La139	14.2	0.12	14.5	0.15	16.9	0.17	14.1	0.12
Ce140	29.8	0.25	30.9	0.24	35.5	0.27	30.6	0.26
Pb208	0.9	0.03	0.9	0.03	1.1	0.03	0.8	0.03
Sr88	248.0	1.98	250.1	1.85	290.5	2.25	216.9	1.47
Nd146	15.1	0.21	15.9	0.20	17.5	0.22	15.4	0.17
Sm147	3.6	0.09	3.8	0.10	4.3	0.10	3.8	0.09
Zr90	96.1	0.73	99.1	0.81	108.3	1.18	93.6	0.66
Hf178	2.4	0.06	2.5	0.06	2.7	0.07	2.5	0.06
Eu151	1.3	0.03	1.4	0.03	1.5	0.03	1.4	0.03
Gd157	4.3	0.12	4.3	0.11	4.6	0.13	4.3	0.11
Dy163	4.4	0.08	4.6	0.08	4.5	0.09	4.6	0.09
Li	4.7	0.05	5.0	0.05	5.2	0.06	4.9	0.05
Y89	23.0	0.20	23.6	0.22	23.8	0.28	23.6	0.17
Er166	2.6	0.06	2.7	0.06	2.7	0.05	2.6	0.06
Yb173	2.4	0.07	2.6	0.08	2.5	0.08	2.7	0.08
Lu175	0.4	0.01	0.4	0.01	0.4	0.01	0.4	0.01
Sc45	32.8	0.35	33.0	0.28	30.2	0.37	38.5	0.30
Be9	0.7	0.04	0.7	0.05	0.8	0.06	0.8	0.05
B10	8.3	0.25	8.7	0.29	10.2	0.30	7.5	0.25
B11	7.6	0.12	8.9	0.14	10.5	0.15	7.1	0.13
Ca43	11.8	0.11	11.8	0.10	11.2	0.09	12.9	0.10
Co59	38.9	0.40	38.8	0.36	38.9	0.35	39.5	0.31
Ni60	131.5	1.47	126.2	1.16	135.1	1.04	92.4	0.92
Cu65	90.9	0.91	89.6	1.15	79.9	0.92	130.4	1.09
Zn66	53.9	0.68	54.5	0.81	55.2	0.61	57.9	0.72

Table 3.2c ICP-MS trace element data (ppm) of Macquarie Island basaltic glass.

	P127-2	±	P122-2	±	P123-1	±	P124-1	±
Rb85	12.8	0.13	18.2	0.17	17.9	0.15	16.5	0.14
Ba137	143.6	1.42	226.5	1.93	225.0	1.66	189.2	1.96
Th232	2.0	0.04	3.2	0.04	3.3	0.05	2.5	0.04
U238	0.5	0.02	0.8	0.02	0.9	0.02	0.6	0.02
Nb93	24.8	0.24	33.2	0.27	32.2	0.21	30.2	0.27
Ta181	1.6	0.03	2.5	0.03	2.4	0.04	1.9	0.03
La139	14.9	0.13	20.3	0.14	19.9	0.13	17.2	0.17
Ce140	31.4	0.26	41.1	0.31	40.5	0.25	34.1	0.33
Pb208	0.9	0.03	1.3	0.03	1.3	0.03	0.8	0.03
Sr88	223.6	1.51	309.0	2.47	311.3	1.78	281.6	2.18
Nd146	16.4	0.21	19.7	0.27	19.0	0.17	15.8	0.23
Sm147	4.1	0.11	4.5	0.09	4.3	0.10	3.4	0.10
Zr90	101.5	0.76	95.9	0.55	90.1	0.47	87.4	0.75
Hf178	2.7	0.08	2.8	0.05	2.8	0.06	2.3	0.06
Eu151	1.4	0.03	1.7	0.03	1.6	0.03	1.3	0.03
Gd157	4.6	0.13	5.0	0.09	4.8	0.10	3.9	0.09
Dy163	4.8	0.09	5.1	0.08	5.0	0.08	4.0	0.07
Li	5.0	0.06	5.4	0.05	5.2	0.05	4.7	0.05
Y89	25.4	0.19	23.7	0.14	22.7	0.16	21.8	0.17
Er166	2.9	0.07	3.0	0.05	3.0	0.05	2.4	0.05
Yb173	2.8	0.11	3.0	0.07	2.9	0.07	2.3	0.06
Lu175	0.4	0.02	0.4	0.01	0.4	0.01	0.3	0.01
Sc45	39.3	0.28	35.5	0.26	34.2	0.23	35.3	0.28
Be9	0.8	0.06	0.9	0.05	0.8	0.06	0.8	0.05
B10	9.8	0.38	6.8	0.20	6.8	0.22	5.1	0.24
B11	9.3	0.18	6.8	0.11	7.0	0.12	5.4	0.11
Ca43	12.9	0.08	12.9	0.11	12.9	0.08	12.7	0.11
Co59	39.8	0.27	40.3	0.29	40.5	0.27	40.0	0.34
Ni60	94.7	1.01	109.0	1.04	116.6	0.86	121.3	1.08
Cu65	133.0	1.37	114.2	0.77	117.8	0.93	113.6	1.06
Zn66	59.7	0.78	60.4	0.84	60.6	0.85	50.7	0.71

Table 3.2d ICP-MS trace element data (ppm) of Macquarie Island basaltic glass.

	P124-2	±	BB10b-1	±	BB10b-3	±	BB124b-1	±
Rb85	16.5	0.18	18.3	0.19	18.0	0.19	27.3	0.21
Ba137	195.0	1.61	191.0	1.60	197.4	1.75	317.1	2.49
Th232	2.5	0.04	2.6	0.04	2.8	0.04	4.1	0.05
U238	0.7	0.02	0.7	0.02	0.7	0.02	1.1	0.02
Nb93	30.4	0.28	31.7	0.25	30.7	0.21	45.1	0.38
Ta181	1.9	0.03	2.0	0.03	1.9	0.03	2.8	0.04
La139	17.4	0.15	18.5	0.14	19.0	0.13	26.4	0.21
Ce140	35.2	0.25	38.0	0.29	38.6	0.31	51.6	0.35
Pb208	1.0	0.03	1.2	0.03	1.1	0.03	1.4	0.04
Sr88	283.7	2.31	277.8	1.87	273.0	1.82	392.6	2.87
Nd146	16.4	0.23	18.4	0.25	19.4	0.24	22.9	0.29
Sm147	3.7	0.10	4.4	0.09	4.5	0.11	4.6	0.11
Zr90	86.2	0.67	122.6	0.80	122.7	0.85	126.0	1.29
Hf178	2.4	0.05	3.1	0.05	3.0	0.06	3.0	0.07
Eu151	1.4	0.03	1.6	0.04	1.5	0.03	1.6	0.04
Gd157	4.0	0.11	5.0	0.10	5.1	0.11	4.7	0.13
Dy163	4.1	0.07	5.1	0.08	4.9	0.09	4.4	0.08
Li	4.8	0.04	5.7	0.05	5.7	0.05	3.3	0.05
Y89	21.4	0.20	26.9	0.22	27.0	0.20	22.6	0.25
Er166	2.5	0.06	3.1	0.06	3.0	0.05	2.5	0.05
Yb173	2.4	0.07	2.9	0.09	2.8	0.06	2.3	0.07
Lu175	0.4	0.01	0.4	0.01	0.4	0.01	0.4	0.01
Sc45	34.3	0.27	32.0	0.25	32.0	0.26	28.2	0.23
Be9	0.7	0.05	1.0	0.06	0.9	0.07	1.3	0.06
B10	6.4	0.25	12.7	0.34	7.2	0.29	5.6	0.24
B11	6.1	0.13	11.8	0.17	6.8	0.11	6.3	0.13
Ca43	12.7	0.10	10.8	0.08	10.7	0.07	10.9	0.08
Co59	40.0	0.35	39.8	0.34	40.1	0.37	36.9	0.29
Ni60	122.3	1.11	121.1	1.28	124.9	1.24	112.0	1.12
Cu65	111.4	1.02	86.3	0.95	87.7	0.87	86.8	0.98
Zn66	52.2	0.83	61.3	0.74	62.4	0.81	50.2	0.72

Table 3.2e ICP-MS trace element data (ppm) of Macquarie Island basaltic glass.

	BB125-1	±	BB125-2	±	BB126b- 1	±	BB129- 1	±
Rb85	18.4	0.15	18.5	0.16	18.7	0.26	27.9	0.20
Ba137	193.9	1.70	198.6	1.76	200.1	2.35	316.9	2.45
Th232	2.7	0.03	2.8	0.04	2.8	0.03	4.0	0.06
U238	0.7	0.02	0.7	0.01	0.7	0.02	0.9	0.02
Nb93	31.6	0.25	31.6	0.27	31.8	0.35	45.7	0.31
Ta181	1.9	0.03	2.0	0.03	2.0	0.03	2.8	0.04
La139	18.9	0.14	19.2	0.15	19.0	0.18	26.4	0.23
Ce140	38.4	0.29	38.9	0.29	39.6	0.39	51.3	0.38
Pb208	1.1	0.03	1.1	0.03	1.1	0.03	1.4	0.04
Sr88	278.9	2.19	280.6	2.14	279.7	2.47	398.5	3.47
Nd146	19.1	0.26	19.1	0.22	19.5	0.27	22.5	0.25
Sm147	4.5	0.10	4.4	0.09	4.5	0.11	4.6	0.10
Zr90	124.7	0.89	126.7	0.89	121.6	1.05	124.4	0.86
Hf178	3.1	0.05	3.1	0.07	3.0	0.06	2.8	0.05
Eu151	1.6	0.03	1.6	0.03	1.6	0.04	1.6	0.04
Gd157	5.0	0.12	5.2	0.11	5.1	0.12	4.5	0.11
Dy163	5.1	0.10	5.1	0.08	5.0	0.10	4.2	0.09
Li	5.8	0.06	5.7	0.06	5.9	0.06	5.0	0.05
Y89	27.4	0.23	28.2	0.21	26.8	0.25	22.2	0.18
Er166	3.0	0.06	3.0	0.06	2.9	0.05	2.4	0.05
Yb173	2.9	0.08	3.0	0.07	2.8	0.08	2.3	0.07
Lu175	0.4	0.01	0.4	0.01	0.4	0.01	0.3	0.01
Sc45	32.8	0.29	32.9	0.26	32.1	0.32	28.6	0.19
Be9	0.9	0.06	1.0	0.06	1.0	0.07	1.3	0.08
B10	8.7	0.26	7.9	0.29	6.7	0.23	8.0	0.35
B11	8.6	0.15	8.2	0.14	7.0	0.11	7.9	0.13
Ca43	11.0	0.09	11.0	0.07	10.9	0.10	11.0	0.08
Co59	40.8	0.33	40.6	0.36	41.2	0.43	37.5	0.31
Ni60	128.0	1.12	123.1	1.14	127.3	1.37	113.8	1.11
Cu65	88.6	0.99	86.8	1.49	87.2	0.93	85.6	1.16
Zn66	62.9	0.88	62.6	0.84	63.9	0.86	51.1	0.72

Table 3.2f ICP-MS trace element data (ppm) of Macquarie Island basaltic glass.

	BB129-2	±	BB130-2	±	BB141-2	±	BB134b- 2	±
Rb85	27.3	0.20	10.7	0.11	16.8	0.26	7.8	0.08
Ba137	303.5	2.66	124.9	0.97	192.1	3.14	82.9	0.78
Th232	3.8	0.06	1.7	0.03	2.5	0.06	1.3	0.02
U238	1.0	0.02	0.4	0.01	0.6	0.02	0.3	0.01
Nb93	44.7	0.38	19.3	0.18	29.4	0.51	14.7	0.11
Ta181	2.7	0.04	1.2	0.02	1.9	0.04	0.9	0.02
La139	25.9	0.22	12.2	0.08	17.5	0.30	9.7	0.09
Ce140	49.5	0.40	26.0	0.20	35.3	0.65	22.1	0.16
Pb208	1.3	0.03	0.8	0.03	1.0	0.03	0.6	0.02
Sr88	393.2	2.47	227.7	1.45	288.3	4.67	136.6	1.02
Nd146	21.8	0.26	14.4	0.17	17.6	0.38	14.1	0.18
Sm147	4.5	0.12	3.5	0.08	4.0	0.12	4.0	0.11
Zr90	126.8	0.85	94.1	0.75	110.2	1.68	101.2	0.76
Hf178	3.0	0.07	2.4	0.06	2.7	0.08	2.8	0.06
Eu151	1.5	0.04	1.4	0.03	1.4	0.04	1.4	0.03
Gd157	4.6	0.11	4.2	0.10	4.6	0.13	5.2	0.12
Dy163	4.3	0.08	4.6	0.08	4.6	0.11	5.6	0.11
Li	5.1	0.05	4.9	0.05	4.9	0.08	6.4	0.06
Y89	22.9	0.13	24.2	0.18	24.1	0.36	30.7	0.22
Er166	2.5	0.05	2.8	0.06	2.7	0.07	3.5	0.05
Yb173	2.3	0.07	2.5	0.07	2.5	0.08	3.2	0.08
Lu175	0.3	0.01	0.4	0.01	0.4	0.01	0.5	0.01
Sc45	29.2	0.22	33.9	0.31	31.9	0.51	38.6	0.35
Be9	1.3	0.06	0.7	0.05	0.8	0.07	0.6	0.04
B10	9.4	0.30	6.1	0.26	7.5	0.31	6.6	0.28
B11	9.8	0.14	6.7	0.14	7.9	0.17	6.8	0.14
Ca43	11.0	0.07	11.6	0.09	11.3	0.19	11.8	0.08
Co59	37.0	0.34	41.5	0.30	38.1	0.61	39.5	0.31
Ni60	114.5	1.21	132.5	1.27	125.5	2.04	96.7	0.83
Cu65	83.6	1.08	92.1	1.07	84.1	1.39	100.4	1.08
Zn66	50.8	0.51	57.7	0.73	48.6	1.71	67.3	0.80

Table 3.2g ICP-MS trace element data (ppm) of Macquarie Island basaltic glass.

	GN88-1	±	GN88-2	±	GN92-1	±	GN92-2	±
Rb85	21.8	0.14	22.0	0.16	20.8	0.19	20.7	0.16
Ba137	258.6	1.41	262.8	1.80	243.2	2.15	238.0	1.52
Th232	3.8	0.05	3.9	0.05	3.4	0.04	3.3	0.04
U238	0.9	0.02	0.9	0.02	0.8	0.02	0.8	0.02
Nb93	40.4	0.21	40.6	0.29	38.4	0.33	38.0	0.30
Ta181	2.8	0.03	2.9	0.03	2.6	0.03	2.5	0.03
La139	23.3	0.12	23.5	0.14	21.8	0.17	21.2	0.14
Ce140	45.9	0.22	46.5	0.26	42.8	0.39	41.7	0.31
Pb208	1.4	0.03	1.4	0.04	1.3	0.03	1.2	0.03
Sr88	320.5	1.51	321.9	2.07	316.4	2.62	311.1	1.92
Nd146	20.9	0.19	21.2	0.24	19.0	0.24	18.6	0.19
Sm147	4.7	0.10	4.6	0.08	4.2	0.10	4.1	0.10
Zr90	107.4	0.49	106.5	0.76	97.1	0.64	95.6	0.72
Hf178	2.9	0.06	2.9	0.06	2.6	0.06	2.5	0.04
Eu151	1.6	0.03	1.6	0.03	1.5	0.03	1.4	0.03
Gd157	4.9	0.10	4.9	0.11	4.5	0.10	4.3	0.08
Dy163	5.1	0.07	5.0	0.07	4.6	0.09	4.4	0.07
Li	5.3	0.04	5.4	0.04	5.2	0.05	5.0	0.05
Y89	24.5	0.16	24.2	0.17	22.2	0.17	22.0	0.14
Er166	3.0	0.05	3.0	0.06	2.7	0.05	2.5	0.05
Yb173	2.9	0.07	2.8	0.07	2.5	0.07	2.5	0.06
Lu175	0.4	0.01	0.4	0.01	0.4	0.01	0.4	0.01
Sc45	34.4	0.18	33.9	0.23	33.7	0.31	33.6	0.23
Be9	1.0	0.05	1.0	0.05	0.9	0.05	0.9	0.06
B10	6.7	0.24	6.8	0.22	7.4	0.21	8.1	0.28
B11	7.4	0.12	7.2	0.14	7.1	0.13	8.1	0.11
Ca43	12.3	0.06	12.3	0.08	12.4	0.12	12.4	0.08
Co59	35.9	0.23	35.9	0.26	36.4	0.28	36.5	0.28
Ni60	98.9	0.84	98.4	0.79	104.9	1.09	105.0	0.80
Cu65	100.6	0.93	100.2	0.83	105.1	0.88	105.9	1.08
Zn66	54.0	0.56	55.0	0.60	51.4	0.69	49.1	0.57

Table 3.2h ICP-MS trace element data (ppm) of Macquarie Island basaltic glass.

	GN94-1	±	GN94-2	±	GN98b- 2	±	GN98d- 3	±
Rb85	20.4	0.20	19.5	0.16	22.1	0.14	22.5	0.18
Ba137	230.7	2.50	226.1	1.70	248.0	1.47	269.1	1.76
Th232	2.9	0.05	3.0	0.06	3.5	0.04	4.0	0.05
U238	0.7	0.02	0.7	0.02	0.9	0.02	1.0	0.02
Nb93	38.3	0.48	37.1	0.35	40.4	0.24	41.2	0.25
Ta181	2.2	0.05	2.2	0.04	2.6	0.03	3.0	0.05
La139	20.1	0.32	20.3	0.16	22.4	0.14	24.3	0.16
Ce140	40.4	0.40	39.4	0.28	44.0	0.24	47.9	0.31
Pb208	1.0	0.04	1.0	0.03	1.3	0.02	1.6	0.03
Sr88	305.6	3.48	303.7	2.19	310.2	1.60	323.2	2.33
Nd146	17.5	0.31	17.4	0.34	20.0	0.23	21.6	0.20
Sm147	3.9	0.12	3.9	0.12	4.5	0.09	4.7	0.10
Zr90	92.9	1.61	95.1	0.81	106.6	0.59	108.9	0.64
Hf178	2.2	0.07	2.3	0.08	2.8	0.05	3.1	0.06
Eu151	1.3	0.04	1.3	0.04	1.5	0.03	1.7	0.03
Gd157	4.0	0.12	4.1	0.12	4.7	0.09	5.0	0.11
Dy163	3.9	0.11	4.0	0.10	4.7	0.08	5.3	0.09
Li	5.1	0.05	4.8	0.07	5.3	0.04	5.6	0.06
Y89	21.1	0.36	21.6	0.21	23.7	0.10	24.5	0.15
Er166	2.2	0.07	2.4	0.06	2.8	0.05	3.1	0.06
Yb173	2.1	0.08	2.4	0.07	2.6	0.07	3.0	0.08
Lu175	0.3	0.01	0.3	0.01	0.4	0.01	0.4	0.01
Sc45	33.3	0.57	33.7	0.33	33.7	0.20	33.5	0.27
Be9	0.8	0.06	0.8	0.06	0.9	0.05	1.0	0.06
B10	7.5	0.27	6.8	0.32	7.5	0.21	6.8	0.21
B11	7.7	0.18	7.2	0.15	8.1	0.11	7.1	0.14
Ca43	12.5	0.16	12.4	0.11	12.3	0.08	12.3	0.11
Co59	37.5	0.45	35.0	0.27	36.0	0.21	35.8	0.32
Ni60	106.6	1.27	99.4	0.97	98.2	0.61	99.6	0.84
Cu65	105.9	1.35	100.8	1.27	102.3	0.81	99.8	0.85
Zn66	45.7	0.83	46.5	0.76	52.6	0.59	55.7	0.69

Table 3.2i ICP-MS trace element data (ppm) of Macquarie Island basaltic glass.

	GN103b- 1	±	GN103c- 1	±	GN103d- 1	±	GN107- 3	±
Rb85	21.5	0.16	1.8	0.08	21.7	0.15	20.5	0.18
Ba137	238.4	1.49	33.7	1.25	242.5	1.49	235.5	1.31
Th232	1.8	0.27	3.4	0.07	3.4	0.05	3.2	0.05
U238	0.5	0.07	0.4	0.05	0.8	0.02	0.8	0.02
Nb93	39.9	0.28	37.5	1.55	39.4	0.21	38.7	0.21
Ta181	2.4	0.03	2.2	0.07	2.6	0.04	2.4	0.03
La139	21.4	0.13	22.5	0.79	22.0	0.14	21.0	0.13
Ce140	42.4	0.29	32.3	1.15	43.5	0.26	40.9	0.23
Pb208	1.3	0.03	1.2	0.06	1.2	0.03	1.3	0.03
Sr88	304.1	1.92	283.6	9.34	305.8	1.81	311.9	1.54
Nd146	18.9	0.19	11.3	0.60	19.7	0.20	18.2	0.21
Sm147	4.1	0.09	2.5	0.22	4.2	0.09	4.1	0.09
Zr90	102.1	0.64	102.9	3.78	104.6	0.58	96.9	0.56
Hf178	2.5	0.05	2.6	0.12	2.7	0.05	2.5	0.04
Eu151	1.5	0.02	0.9	0.11	1.5	0.03	1.4	0.03
Gd157	4.3	0.09	2.8	0.24	4.5	0.12	4.1	0.10
Dy163	4.2	0.06	3.0	0.19	4.6	0.08	4.2	0.07
Li	5.2	0.05	3.5	0.12	5.2	0.05	5.1	0.04
Y89	22.7	0.18	20.3	0.69	23.7	0.14	22.0	0.13
Er166	2.5	0.04	2.3	0.17	2.7	0.06	2.5	0.04
Yb173	2.4	0.06	2.6	0.17	2.6	0.07	2.4	0.06
Lu175	0.3	0.01	0.4	0.04	0.4	0.01	0.4	0.01
Sc45	33.1	0.21	32.2	0.77	34.0	0.22	34.2	0.17
Be9	0.9	0.05	2.1	0.21	0.9	0.05	0.9	0.05
B10	8.1	0.22	156.1	6.52	6.0	0.22	8.7	0.27
B11	9.1	0.14	160.8	4.93	5.9	0.11	8.6	0.11
Ca43	12.2	0.08	16.5	0.48	12.2	0.09	12.5	0.06
Co59	36.4	0.28	32.4	0.99	35.9	0.25	37.0	0.22
Ni60	101.2	1.03	95.7	2.49	103.6	0.94	106.7	0.72
Cu65	103.3	1.11	96.0	2.54	101.7	0.92	107.9	0.83
Zn66	50.9	0.66	45.5	2.05	53.2	0.61	49.7	0.54

Table 3.2j ICP-MS trace element data (ppm) of Macquarie Island basaltic glass.

	GN110- 1	±	GS136c- 2	±	ML122- 1	±	ML122- 2	±
Rb85	20.7	0.19	22.2	0.19	36.3	0.25	36.0	0.26
Ba137	237.8	2.33	246.3	1.77	471.5	3.83	461.0	3.69
Th232	3.2	0.04	3.4	0.05	8.9	0.11	8.5	0.09
U238	0.8	0.02	0.8	0.02	2.1	0.03	2.1	0.03
Nb93	38.3	0.31	41.0	0.33	74.4	0.53	74.0	0.63
Ta181	2.4	0.04	2.6	0.03	5.7	0.07	5.4	0.07
La139	21.2	0.18	23.8	0.17	47.9	0.37	46.5	0.35
Ce140	41.4	0.35	48.8	0.35	89.4	0.63	86.8	0.65
Pb208	1.2	0.03	1.4	0.04	2.8	0.05	2.7	0.05
Sr88	312.0	2.53	295.6	2.45	457.1	3.73	449.2	3.73
Nd146	18.5	0.20	22.6	0.21	35.1	0.35	34.3	0.37
Sm147	3.9	0.09	4.7	0.10	6.7	0.15	6.5	0.12
Zr90	96.4	0.62	123.7	1.02	136.9	1.08	134.1	0.97
Hf178	2.5	0.05	3.2	0.06	4.1	0.08	3.8	0.07
Eu151	1.4	0.04	1.7	0.03	2.3	0.04	2.1	0.04
Gd157	4.4	0.10	5.2	0.11	6.2	0.14	6.2	0.12
Dy163	4.2	0.08	4.8	0.09	5.8	0.09	5.7	0.10
Li	5.0	0.05	5.4	0.06	5.5	0.05	5.4	0.05
Y89	22.2	0.14	25.9	0.25	25.2	0.20	24.5	0.16
Er166	2.5	0.05	2.9	0.05	3.4	0.07	3.2	0.07
Yb173	2.4	0.07	2.8	0.07	3.2	0.08	3.1	0.09
Lu175	0.3	0.01	0.4	0.01	0.5	0.01	0.5	0.02
Sc45	33.9	0.27	36.2	0.33	32.8	0.26	32.4	0.28
Be9	0.8	0.06	1.0	0.06	1.4	0.08	1.4	0.06
B10	6.0	0.28	5.6	0.24	8.1	0.26	7.6	0.28
B11	5.7	0.12	5.9	0.11	8.6	0.14	7.7	0.13
Ca43	12.5	0.11	11.9	0.10	11.8	0.09	11.7	0.10
Co59	36.1	0.37	35.2	0.31	37.5	0.30	37.3	0.29
Ni60	103.2	0.96	82.7	0.82	117.6	0.92	118.0	1.02
Cu65	106.7	1.08	110.5	1.07	96.6	0.97	95.3	0.93
Zn66	49.7	0.67	57.5	0.71	62.8	0.75	61.0	0.77

Table 3.2k ICP-MS trace element data (ppm) of Macquarie Island basaltic glass.

	H34	±	H52	±	H76	±
Rb85	5.5	0.15	28.9	0.66	8.2	0.18
Ba137	14.9	0.39	70.2	1.43	2.7	0.17
Th232	1.1	0.06	1.1	0.04	0.7	0.03
U238	0.3	0.03	0.4	0.03	0.1	0.01
Nb93	15.7	0.70	17.1	0.39	0.3	0.02
Ta181	0.9	0.05	1.0	0.03	0.0	0.00
La139	10.6	0.38	15.9	0.36	0.3	0.02
Ce140	25.2	1.26	42.6	0.83	0.9	0.05
Pb208	0.8	0.05	1.0	0.12	0.3	0.02
Sr88	107.7	1.69	92.1	1.84	43.3	0.78
Nd146	13.5	0.71	26.0	0.53	0.5	0.03
Sm147	3.8	0.25	7.5	0.26	0.2	0.03
Zr90	82.3	1.81	128.4	2.21	2.4	0.07
Hf178	2.1	0.13	3.3	0.12	0.1	0.01
Eu151	1.2	0.06	2.7	0.08	0.0	0.01
Gd157	4.3	0.24	9.3	0.29	0.2	0.03
Dy163	4.8	0.27	10.2	0.24	0.3	0.02
Li	21.2	0.90	14.7	0.42	41.4	0.72
Y89	26.9	0.86	65.8	1.36	2.4	0.07
Er166	2.8	0.15	6.3	0.15	0.3	0.03
Yb173	2.5	0.12	5.2	0.16	0.4	0.03
Lu175	0.3	0.02	0.6	0.03	0.1	0.01
Sc45	38.4	3.29	37.2	0.81	7.6	0.16
Be9	0.5	0.06	0.4	0.08	0.0	0.00
B10	36.6	1.19	53.0	1.97	12.2	0.48
B11	39.0	0.95	50.7	1.60	11.8	0.28
Ca43	3.5	0.08	4.6	0.11	0.9	0.02
Co59	38.0	1.75	50.0	1.18	59.1	0.95
Ni60	143.4	6.14	147.5	2.86	121.7	2.34
Cu65	29.1	4.16	152.0	10.38	204.9	6.95
Zn66	83.1	3.93	119.3	3.21	120.8	1.87

## **UPLIFT HISTORY OF MACQUARIE ISLAND**

### **Chapter 4: Extension along the Australian-Pacific transpressional transform plate boundary near Macquarie Island**

#### **4.1 INTRODUCTION**

The Australia-Pacific plate boundary south of New Zealand is one the most significant transform plate boundaries in the world. This seismically active boundary has dominantly strike-slip focal mechanisms, including the largest strike-slip earthquake ever recorded (Mw8.1), confirming that motion along the present plate boundary is right lateral, strike-slip (Frohlich et al., 1997). The geology of the ocean floor in this region has been poorly understood until recently. Geophysical surveys along the Australian-Pacific plate boundary in 1993, 1994, 1996, and 2000 have increased our knowledge substantially (e.g., Massell et al. 2000; Meckel, 2003; Meckel et al., in press). Macquarie Island (54°30'S, 158°54'E, Figure 1.1) is the only significant exposure of the ocean crust in this region; thus understanding the geologic history of the island is critical in understanding the history of the plate boundary.

The Macquarie Ridge Complex (MRC) is a series of bathymetric highs and lows that follows the modern day plate boundary (Figure 4.1) and formed as a result of transpression (Meckel, 2003). Massell et al. (2000) identified a ~5-10 km wide “Macquarie Fault Zone” that accommodates the transform motion and lies along the bathymetric highs forming the crest of the MRC. Macquarie Island forms the highest point of the MRC (Figure 4.1). The main plate boundary fault

adjacent to the island trends N10E, and its primary locus lies approximately 4.5 km west of the island (Figures 1.2, 4.1, 4.9). Thus, the island presents a unique opportunity to study structures that form within a major marine transform fault zone on land.

This study presents the results of a structural study of recent faults on Macquarie Island that formed during the current transpressional regime. These data are compared to the results from a seafloor geophysical study of Daczko et al. (2003). It was found that the faults formed due to local extension within the transpressional environment, caused by step-overs accommodating the motion on the plate boundary faults.

#### **4.2 TECTONIC SETTING**

Marine geophysical data collected around Macquarie Island and along the MRC (Massell et al., 2000) show tectonic spreading fabric (faulted abyssal hills) that formed parallel to the spreading axes with associated perpendicular fracture zones (Fig. 1.2). These fracture zones, spreading fabric, and magnetic anomalies demonstrate that spreading, which started in Eocene time (Weissel et al., 1977; Sutherland, 1995; Wood et al., 1996; Lamarche et al., 1997; Cande et al., 2000; Massell et al., 2000), rotated during Tertiary time until extension nearly paralleled the plate boundary. Transform motion became dominant at about 10 Ma (Lamarche et al., 1997; Massell et al., 2000).

The oceanic crust exposed on Macquarie Island formed during the last stages of seafloor spreading (Massell et al., 2000, Figure 1.2). All levels of ocean crust including upper mantle rocks are found on the island (Figure 4.2a), and

faults that juxtaposed the upper crust and lower crust/upper mantle sections formed near the intersection of a ridge and a transform (chapter 1). The geology and tectonic setting of the island and the Australian-Pacific plate boundary have been described in detail elsewhere (e.g., Goscombe and Everard, 2001; Varne, 2000; chapter 1).

### **4.3 MACQUARIE ISLAND FIELD DATA**

Macquarie Island comprises fault-bounded blocks made up of all levels of oceanic crust and upper mantle from extrusive lavas and minor sedimentary rocks to sheeted diabase dikes, gabbros, and serpentinized peridotites (Figure 4.2a) (Christodoulou et al., 1984; Goscombe and Everard, 2001; Varne et al., 1969; Varne et al., 2000; Varne and Rubenach, 1972). Recent faults dissect the entire island but are dominant in the volcanic rocks of the centre third of the island, creating long, linear ridges and basins (Figures 4.2 and 4.3b, profiles C-G). The ultramafic and plutonic rocks of the northern end have a smoother, less rugged topography with broad, flat-topped mountains (Figures 4.2b and 4.3b, profile K). The volcanic rocks of the southern end have formed many sharp craggy peaks with some linear fault scarps (Figures 4.2b and 4.3b, profile K).

I examined the most prominent of the ~150 recent faults and fault scarps identified and mapped by Goscombe and Everard (1998, 2001), excluding faults of limited extent or lacking clear topographic expression or exposure. I measured strike, length, and throw, as well as noting the location, rock types cut and cross-cutting relationships of faults and other prominent features (Table 4.1). Overall, recent faults on the island exhibit almost exclusively normal and oblique normal

motion. The topography of the central portion of the island is dominated by an echelon NE and NNE faults that step to the right and left, forming pull-apart basins or relay faults that link the larger faults. In many cases, faults die out and motion is relayed to a nearby parallel fault. Southward, the primary fault strikes change to NNW and NW. These NW faults truncate the NE ones and are less distinct, but display similar en echelon relationships and normal-oblique motion.

Throughout the island, faults with scarps are linear to curvilinear and extend for hundreds of meters up to ~7 km along strike. Most, however, extend continuously for 500 m to 1 km along strike and terminate at intersections with other recent fault scarps, or their scarps gradually diminish along strike over a distance of a few tens to hundreds of meters. Most recent fault scarps have throws of 5-15 m, but the larger scarps are up to 150 m high (Figure 4.2c). These measurements provide a minimum estimate for total vertical movement, however, as marine wave action would most likely have removed any topography produced on these faults prior to emergence of the island above sea level.

The strike of recent faults ranges from WNW to NE (Figure 4.4a). I have weighted these data for length along strike (Figure 4.4b) and for throw (Figure 4.4c). The NNE- to NE-striking recent faults are by far the most laterally continuous and also show the largest throw, and therefore provide the most significant constraints on the tectonic models as discussed further below. Additionally, the major recent faults change in strike along the length of the island from generally NE- and NNE-striking in the north to N-, NW- and NNW-striking in the south (Figure 4.2c).

Most major recent faults on the island show a dominantly normal sense of motion (Table 4.1). Horsts and grabens are common, and normal displacement is transferred across en echelon faults on relay ramps. Accurate kinematic analysis of these faults is difficult, however, given limited exposure of actual fault planes; most fault planes are eroded or buried by mass wasting debris. Topographic relief clearly constrains estimates of vertical movement. I observed only limited strike-slip displacement on outcrop-scale faults; the similarity of geologic units across major faults precluded using offset of units or marker horizons to determine lateral displacements. Goscombe and Everard (2001) estimate lateral displacements ranging from 80 to 2500 m; however, the only two large displacements (1 km and 2.5 km) are based on apparent offset of seafloor spreading-related faults. My fieldwork has demonstrated that these spreading-related faults formed with this stepped geometry (chapter 1) thus these large lateral displacements are not the result of recent strike-slip faulting. Unlike Goscombe and Everard (2001), this study found no evidence for transpression. The thrust faults they mapped in the northern end of the island show no topographic relief. I reinterpret their faults that place volcanic rocks on diabase dikes as depositional contacts, an interpretation similar to that of other workers (Alt et al., 2003). Faulting and fracturing in this area occurs beneath the actual contact. Their other thrust fault that places ultramafic rocks on dikes was too poorly exposed as a result of mass wasting for verification.

### **4.3.1 Fault rocks**

Recent faults were distinguished from submarine faults by the mineralogy and style of faulting. The fault planes of the major faults were only rarely exposed, but all had dramatic fault scarps with evident recent motion. Smaller scale faults were common. These faults generally had no associated mineralization or low temperature (calcite, zeolites, gypsum) mineralized slickenside striations or steps along fault planes. Most of the faults either contained dry breccias with grooved fault slickenside striations or they formed discrete, sharp planes with no gouge or faulted material. In one case a major fault plane was exposed (the Brothers Fault) due to a recent land slide; here the fault had a grooved dry breccia surface, with the slickenlines indicating normal motion.

The following discusses the recent faults that occur on Macquarie Island from north to south.

### **4.3.2 Northern recent faults**

Few recent faults are observed in the northern third of the island, possibly due to the style of erosion of the plutonic and serpentinitized ultramafic rocks. Near Mt. Elder (Figures 4.3a and 4.3b, profile B), NNE- to NE-striking faults show 5-20 m high scarps, but they are less continuous than those in the central region of the island.

### **4.3.3 Central recent faults**

The Brothers fault is the most extensive recent fault on the island, located along the central east coast (Figures 4.2c, 4.5a and 4.6; Table 4.1a). From Brothers Point to Waterfall Bay (Figure 4.2b, 4.2c), the fault has created a steep

scarp of varying heights. At Brothers Point, the fault shows slickensides and striations with a  $> 80^\circ$  pitch down dip to the south on moderately ( $\sim 50^\circ$ ) W-dipping fault planes (Figure 4.5b). The topographic offset (W-side down, Figure 4.5a) and small steps on fault planes indicate a normal sense of motion (Figure 4.5b). Normal dip-slip lineations surround the southern end of the Alpine Fault segment of the Australian-Pacific plate boundary within 1-100 m of the principal displacement zone, which is also dominantly strike-slip (Sutherland and Norris, 1995). The Brothers fault becomes less defined in two locations, near Red River (Figures 4.2b and 4.6a) and Green Gorge (Figures 4.2b and 4.6b), where displacement is transferred to other fault segments. These transfer zones contain minor, less continuous, faults oblique to the Brothers fault, which have less prominent scarps (Figures 4.6a and 4.6b). In the Red River area, the fault scarp tapers off southward and then picks up displacement on another major segment farther to the east (Figure 4.6a). The intervening transfer zone contains NNE- to NE-striking faults, and the faults are less distinct, lacking the sharp scarps of the Brothers fault. The NE-striking faults appear to act as links between the two major traces of the Brothers fault. One of the NE-striking faults changes the up-thrown side halfway along its length, with the northwest side up at the southern end, and the southeast side up at the northern end, apparently caused by a counter-clockwise rotation. Also in this area, two NNW-striking faults affect the topography, but the NE-striking faults are dominant. In the Green Gorge area, where the fault steps slightly to the right (Figure 4.2a), a series of small grabens and half grabens ( $\sim 20$  m long and 5-41 m wide, bounding fault scarps 2-6 m tall)

with NW strikes are within the transfer zone (Figure 4.6b). The Brothers fault cuts the northern set of grabens, suggesting that the fault propagated north into the pull-apart basin after the grabens formed.

In the central section of the island, en echelon faults form pull-apart basins or half-graben lakes (e.g., Prion Lake, Gratitude Lake, Figure 4.3, profiles D and F). These basins all trend NNE to NE and are generally asymmetric with one dominant bounding fault. Prion Lake is the largest example (Figure 4.3, profile D and Figure 4.7a). The scarps that form this lake range from 5-50 m in height, with the NW scarp more pronounced. The pull-apart basin is formed by a left step, from the fault that forms the SE side of the lake to the fault that forms the NW side (Figure 4.3). At the northern end of the lake, the primary northwest fault tapers off, and the motion is picked up by a parallel fault a few meters to the east, which forms a linear scarp for ~20 m (Figure 4.7a). This type of relay between en echelon faults is common across the island. En echelon faults also form horsts in this part of the island (Figure 4.7b).

#### **4.3.4 Southern recent faults**

South of Pyramid Lake (Figure 4.2a), the Brothers fault and other NE faults have less definition, and more NNW and NW faults are observed. Although NNE and NE faults dissect the southern region, they are frequently truncated (e.g., Mt. Jeffries; Figure 4.3a between profile I and J) or offset (Mt. Blake; Figure 4.3a, fault 3) by the NNW and NW faults. No faults in this region are as continuous as the Brothers fault to the north, and faults frequently die out along strike. A well-developed horst and poorly developed graben pair (327° strike,

Figure 4.2a, faults 35-37) is found near Mt. Jeffryes. Only one half-graben lake is observed in the southern end of the island (Lake Ainsworth, Figure 4.3, profile J); its scarp can be followed for 500 m.

## **4.4 DISCUSSION**

### **4.4.1 Genesis of Macquarie Island recent faults**

Continental transform plate boundaries commonly show a variety of secondary structures such as Riedel and primary shears (R, R' and P), normal faults, and thrust faults (Keller et al., 2002; Naylor et al., 1986; Sylvester and Smith, 1976; Wilcox, 1973) in orientations similar to those produced in analogue materials undergoing wrenching (Casas, 2001; Naylor et al., 1986, Figure 4.4a). For transpressional settings, field observations and analogue modeling, have shown that the secondary structures change orientation, and which secondary features are dominant changes as well (Casas, 2001; Keller et al., 2002) (Figure 4.5a).

Goscombe and Everard (2001) proposed that recent faults on Macquarie Island match predicted geometries for secondary faults. Across the island, however, dominantly normal faults are found, in all orientations, with a minor component of strike-slip motion and no evidence for thrust faulting. Recent fault orientations and those predicted by a right lateral shear couple along a N14°E plate boundary (Figure 4.4a) do not correspond. Few observed faults are in the correct orientation for normal motion, and most are not in any predicted orientation. N- to NNE-striking faults are predicted to be right lateral strike-slip faults; instead they are dominantly normal faults. Transpression rotates the

predicted fault orientations clockwise, which makes any correlation worse. Thus, the recent faults on the island are not compatible with model predictions.

Massell et al (2000) identified a major pull-apart basin in the seafloor where the plate boundary makes a sharp 18° change in orientation between the McDougall and Macquarie segments (Figure 4.1), a structure very similar to the pull apart basins observed on Macquarie Island. The presence of this structure suggests an alternative explanation (i.e. extension in a transfer zone between two strike slip faults) for such unexpected structures within the transpressional regime. In an attempt to understand the discrepancy between the orientations and kinematics of the faults on the island with structural model predictions and to investigate this second option as well as other possible explanations, Nathan Daczko, a postdoctoral scientist at the University of Texas at Austin, as part of a collaborative effort, examined seafloor geophysical data around the island. Details of the geophysical study are given in Daczko et al. (2003) and are summarized below.

#### **4.4.2 Marine geophysical analysis**

Daczko analyzed 1:500,000 scale reflectivity data on the MRC for the McDougall and Macquarie segments and bathymetric profiles interpreted from seismic reflection data across the MRC. He followed Massell et al. (2000) and inferred that lineaments that define a deformed zone along the Australian-Pacific transform plate boundary represent active fault scarps within the fault zone. His key results include (see Daczko et al., 2003 for details):

- In 11 main locations along the McDougall and Macquarie segments (Figure 4.8), the primary transform fault steps to the right forming a series of en echelon faults (Figure 4.8).
- The Australian-Pacific transform fault system forms a ~15 km wide zone of NNE- to NE-trending lineaments north of the island and a ~8-10 km wide zone of NNE to NNW-trending lineaments south of the island (Figure 4.8).
- Macquarie Island is located within these lineament zones (Figure 4.8) and exposes features similar to those mapped from reflectivity data. Daczko et al. (2003) use this similarity to “ground truth” the interpretations of the geophysical data.
- Bathymetric profiles (Figure 4.8) show double ridge crests and central valley depressions associated with right step-overs, and single ridge crests are associated with long linear segments of the plate boundary at a distance from step-overs. The valleys were interpreted as pull-apart basins (Massell et al., 2000; Daczko et al., 2003) associated with right steps in the dextral strike-slip plate boundary as discussed further below.

#### **4.4.3 Comparison of island and marine geophysical data**

Macquarie Island lies within the zone of deformation at the currently active plate boundary. The patterns of faulting on the island and of the lineaments mapped on the seafloor within the ridge crests using reflectivity data by Daczko (Daczko et al., 2003) (Figures 4.8, 4.9) are equivalent, thus validating the

interpretation of these lineaments as recent faults. Faults on the island occur as a series of en echelon faults that step to the right and left, forming pull-apart basins and relay zones (Figure 4.3, 4.8, 4.10). Numerous, differently oriented, smaller faults occur in these transfer zones, accommodating strain where displacement is transferred from one fault segment to another. Although on a different scale, these relationships match Daczko's interpretation of the plate boundary fault zone using marine geophysical data (Figure 4.9). The presence of these finer scale features on Macquarie Island supports the interpretation that the larger basins within the ridge crests are composed of numerous smaller pull-apart basins and extensional relay zones that help accommodate the overall deformation (Daczko et al., 2003).

The dominant fault orientation on the island changes from NE- striking with minor NNE- striking faults in the north to NW- and N-striking with minor NNE-striking faults in the south (Figure 4.2, 4.3). Although the orientation changes, the faults form a similar en echelon pattern, indicating similar processes formed them. It appears that the NNE-striking faults formed first, and were truncated or offset by later NW-striking faults. This change in orientation records the change in orientation observed between the plate boundary faults and associated lineaments to the north and south of the island (Figure 4.8).

Most recent faults on the island show primarily normal motion (with a minor component of oblique right lateral motion), in apparent contrast to the island's right lateral transpressional tectonic setting and recent history of uplift. I interpret the recent faults on Macquarie Island as forming in response to local

extensional stresses associated with right steps in the Australian-Pacific plate boundary located ~4.5 km west of the island (Figure 4.9).

Petrological analysis of the recent faults on Macquarie Island suggests that the mode of deformation within the faults has most likely changed with time and emergence of the island. The earlier generation of recent faults most likely formed in young oceanic crust with a higher geothermal gradient, when the island was still submerged with remnants of hydrothermal fluid circulation. The most recent generation of faults on Macquarie Island possibly reflect a lower geothermal gradient along the plate boundary and different stress fields at the convergent margin may have been inhibited fluid flow.

#### **4.4.4 Model for formation of plate boundary faults**

Integration of the field data presented above and the geophysical data of Daczko et al. (2003) provides an explanation for the formation of plate boundary faults and the development of local extension across a zone which is clearly experiencing transpression.

The present-day curvature of the plate boundary is inherited from the pre-existing divergent plate boundary and has been modified very little since seafloor spreading stopped at ~10 Ma (Meckel, 2003; Figure 4.10a). It is proposed that when faults related to the right lateral transform formed, their orientation was controlled by the concave east curvature of the plate boundary, resulting in a series of straight, en echelon faults that step to the right to conform to the pre-existing geometry (Figure 4.10). The en echelon steps may develop as many small steps on a broad curve or as one big step at a significant change in orientation.

The right steps in the plate boundary faults result in local extension in the transfer zone between fault segments.

The degree of curvature in the plate boundary would control the length of fault segments and the number of en echelon steps. For example, Daczko et al. (2003) noted that the plate boundary, along the McDougall segment, shows minor curvature with a small change in strike (3-4°) distributed over the total length of the segment (Figure 4.8), which results four relatively long en echelon faults linked by small extensional relay zones or pull-apart basins. The sharp change in strike of the plate boundary at the transition between the McDougall and Macquarie segments (~18° change in strike over < 50 km distance) results in a major step-over and large pull-apart basin. The large curvature in the plate boundary along the Macquarie and contiguous Hjort segments (Figure 4.10) results in many short fault segments and a higher density of stopovers. Macquarie Island is located adjacent to a large extensional basin (Figure 4.9) that marks a change in overall orientation of plate boundary faults. Faults on the island change in orientation along its length recording the change in overall plate boundary fault orientation, and the dominantly extensional structures, including pull-apart basins and relay zones, result from the island's position adjacent to a larger scale pull-apart basin.

#### **4.5 CONCLUSION**

Recent faulting on Macquarie Island reflects dominantly extensional tectonics, apparently in conflict with the island's transpressional tectonic setting and history of uplift. The island is interpreted to be located within an extensional

local stress field related to right steps in the plate boundary located ~4.5 km to the west, and fault geometries and kinematics are not directly related to current transpression at the plate boundary.

The results of my field investigation coupled with analysis of marine geophysical data for the surrounding seafloor (Dackzo et al., 2003) indicate that the modern plate boundary inherited its curving geometry from the older spreading system, and the new transpressional faults have formed a right-stepping en echelon pattern while following this curve.

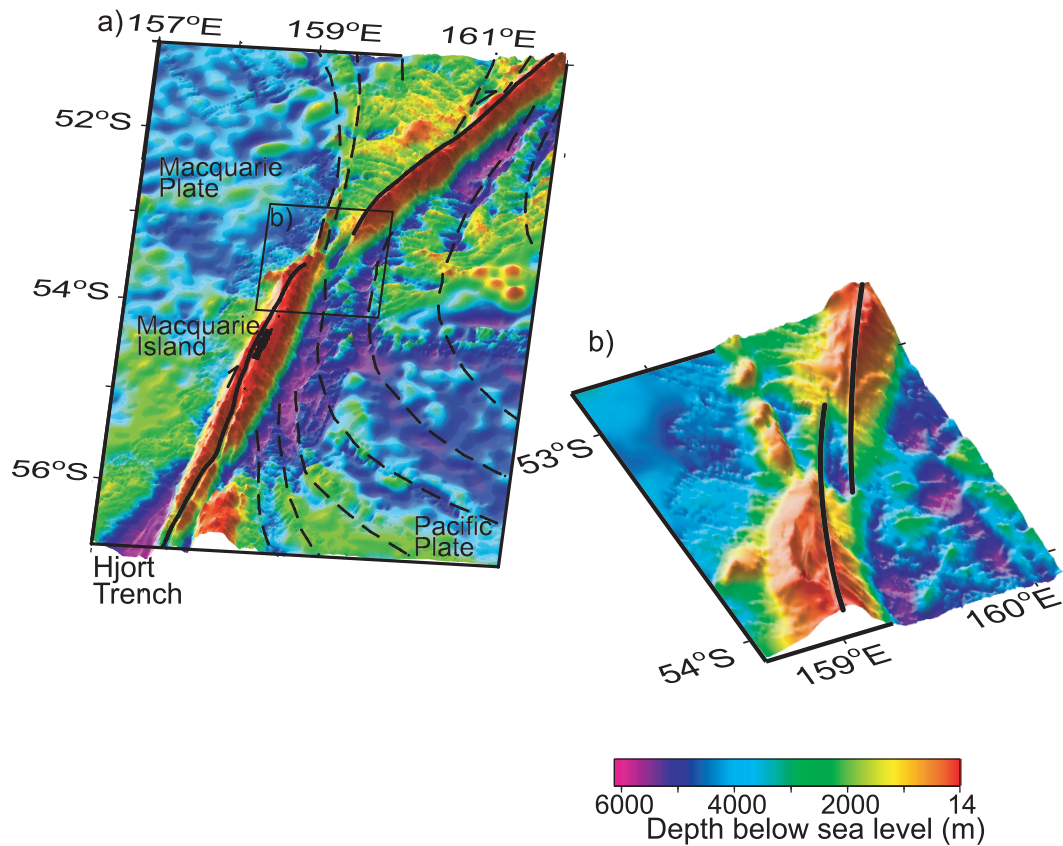


Figure 4.1. a) 3D perspective view of the MRC modified from Daczko et al. (2003) showing the McDougall segment in the north (above  $\sim 53^{\circ}20'$  S), the Macquarie segment in the south (between  $\sim 53^{\circ}20'$  S and  $\sim 56^{\circ}40'$  S) with the northern tip of the Hjort segment in the base of the diagram (after Bernardel and Symonds, 2001). Macquarie Island is at the apex of the Macquarie segment and is shown in black. Mercator projection viewed from  $175^{\circ}$  at an elevation of  $40^{\circ}$ . b) Figure 2a overlain with regional tectonic features. Thick black line is the main Australian-Pacific plate boundary and dashed black lines are fracture zones (from Massell et al. (2000) with one new fracture zone identified by magnetic anomaly picks from Keller et al. (2002)). c) 3D perspective view of the transition between the McDougall and Macquarie segments of the MRC. Mercator projection viewed from  $200^{\circ}$  at an elevation of  $40^{\circ}$ . d) Interpretation of an en echelon right step-over in the Australian-Pacific plate boundary. Note the bathymetric low in the pull-apart basin located between the right step-over.

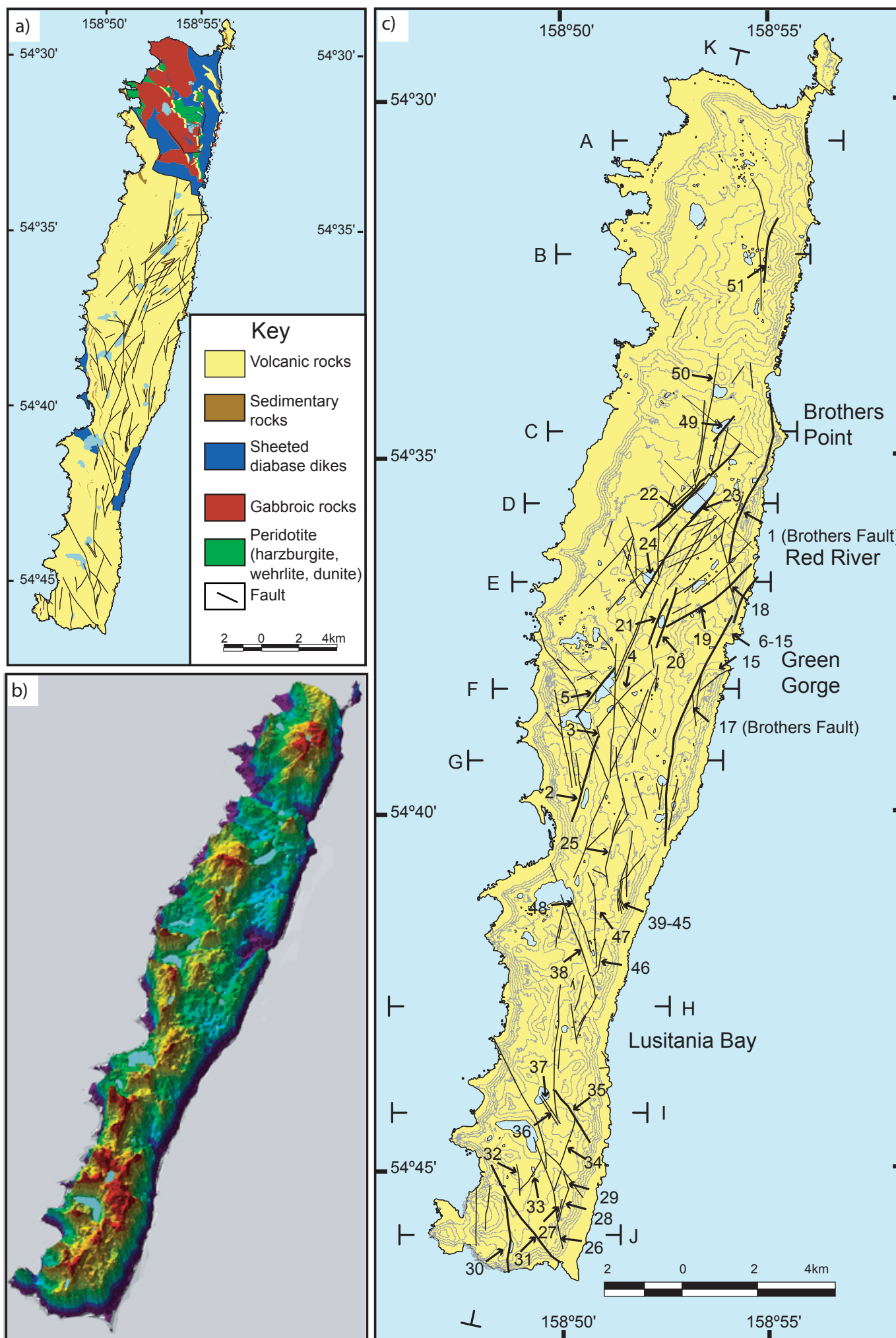


Figure 4.2. Field data from Macquarie Island. a) Geologic map of Macquarie Island, (after Goscombe and Everard, 1998). The island has a complete suite of oceanic rocks, from upper mantle to upper crustal rocks. Map shows both the recent faults examined in this study, as well as faults that formed during seafloor spreading. b) Shaded relief topography image of Macquarie Island. The Brothers fault and related faults create linear valleys along the central- and north-eastern coast. Other faults form pull-apart basins that contain lakes. Geographic locations mentioned in the text are labelled. c) Recent faults on Macquarie Island superposed on topographic contours. Bold lines are major faults with significant fault scarps; other lines are smaller recent faults. Numbered faults correspond to those in Table 4.1. T-bars mark cross section lines in Figure 4.4b. Three shorter cross sections (detail profiles in Figure 4.4b) are marked with lines.

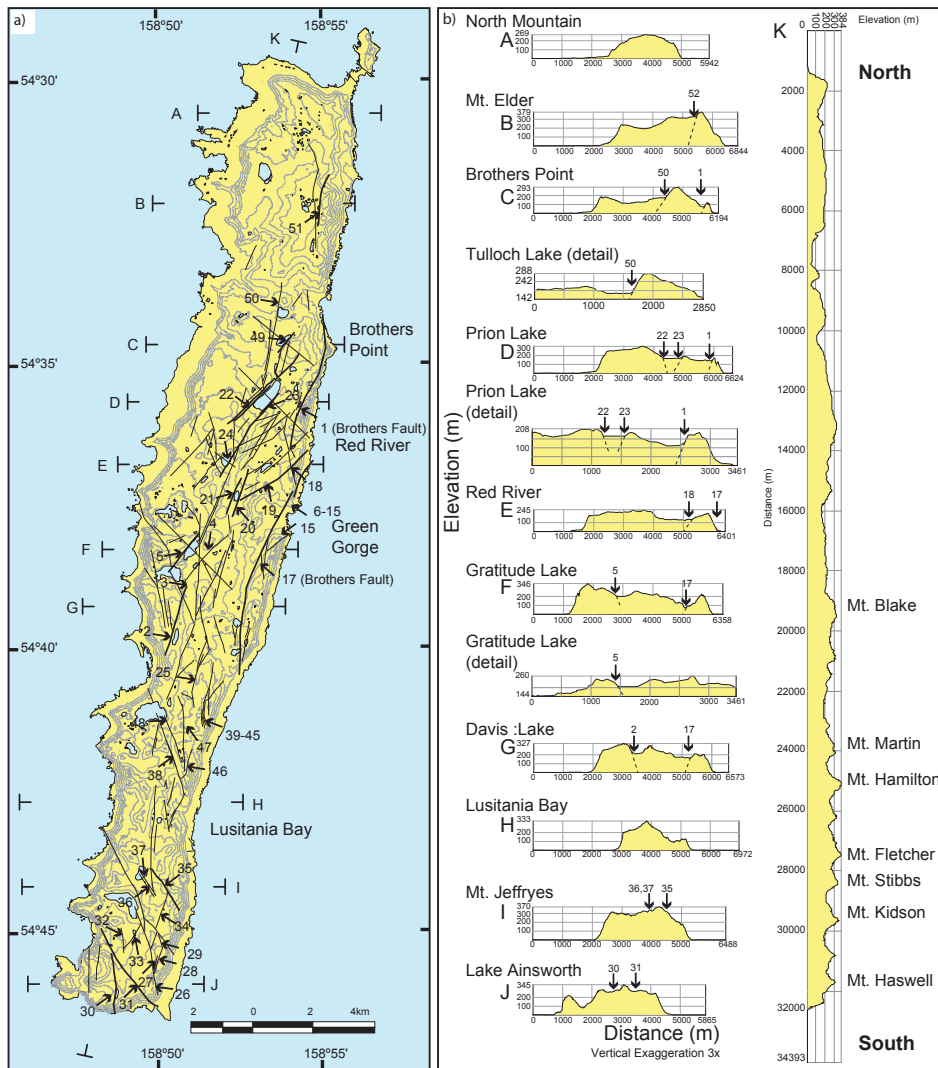


Figure 4.3. Topographic profiles and faults, Macquarie Island. a) Figure 4.2c repeated. T-bars mark cross section lines in Figure 4.4b. Three shorter cross sections ("detail" profiles in Figure 4.3b) are marked with lines. b) Topographic profiles of Macquarie Island. The steep sides of the island are not cliffs generated by faults; they form via mass wasting as the island is uplifted with the ridge complex. Numbered faults correspond to Figure 4.3a and Table 4.1. Faults with obvious scarps have been projected with dashed lines. Note that lake depths are unknown at present and flat areas in the profiles with lakes represent water level at time of survey. Profile K shows the topographic change from north to south, from rounded mountains in the north to rocky peaks dominating the south.

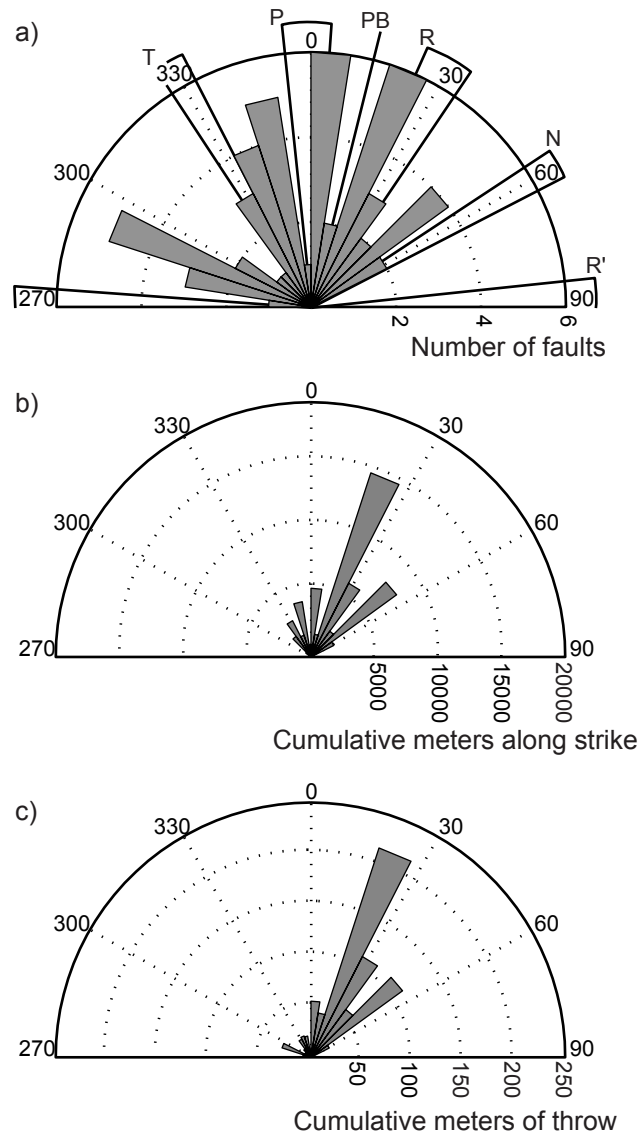


Figure 4.4. Recent Fault data. a) Rose diagram of the strike of recent fault data shown in Table 4.1. The orientations of the plate boundary (PB) and expected secondary faults for classical wrenching (R, R' - Riedel and P - primary shears; N-normal, T- thrust faults) are overlaid. The data do not fit the predicted fault orientations and types. b) Data shown in Figure 4.4a weighted for along strike length of the faults showing that the longest recent faults are within the NNE-striking group. c) Data shown in Figure 4.4a weighted for throw showing that the faults with the largest throw are within the NNE-striking group.

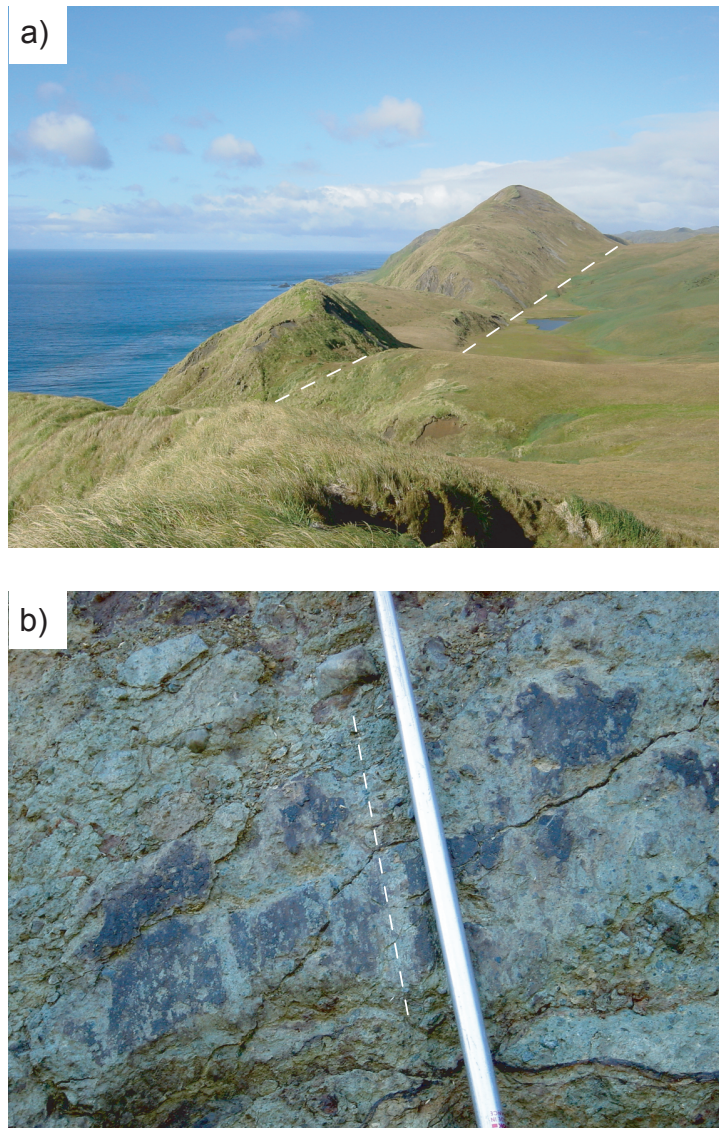


Figure 4.5. The Brothers Fault. a) The Brothers Fault scarp Between Brothers Point and Green Gorge, looking S (fault 1, Figure 4.4a, Table 4.1). The maximum estimated height of the scarp at this location is ~150 m. White dashed lines indicate the base of the W-dipping scarp. b) Exposure of the Brothers Fault west of the Brothers Point hut, view to E. Dashed white line shows orientation of down-dip slickensides. Ski pole is ~1-1.5 cm across.

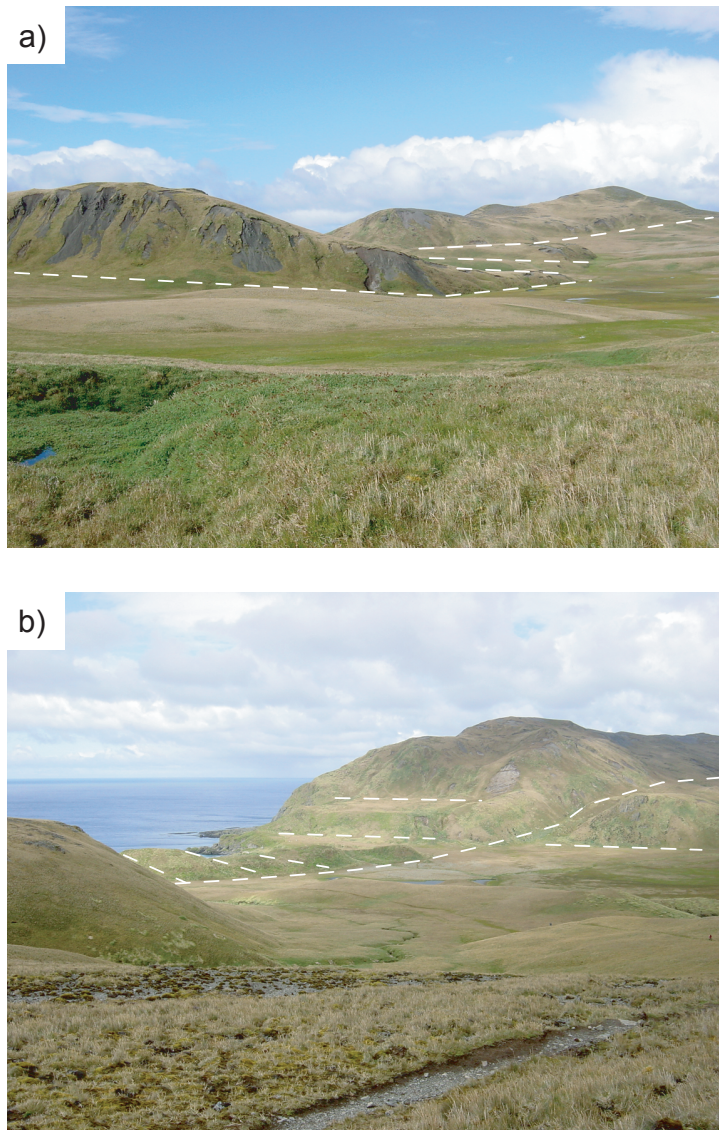


Figure 4.6. Brothers Fault transfer zones. a) The Brothers Fault transfer zone at Red River (Figure 4.2c), looking SE. White dashed lines mark fault traces in the transfer zone. The maximum estimated height of the scarp at this location is ~50 m. b) Green Gorge catchment, looking SE. White dashed line running parallel to the coast marks the Brothers Fault. White dashed lines running at a high angle to the coast are graben-bounding faults (faults 6-16, Figure 4.2c, Table 4.1). The maximum height of the scarps at this location is ~20 m.

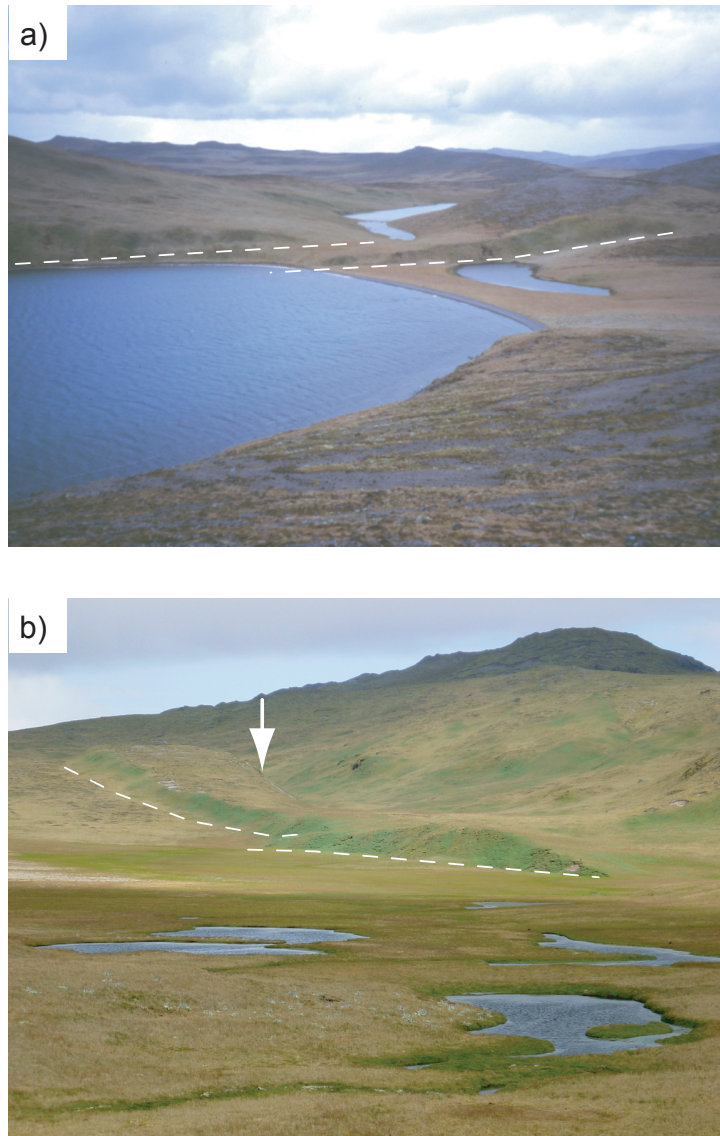


Figure 4.7. Prion Lake and Red River. a) Northern end of Prion Lake, looking NNW (fault 22, Figure 4.2c, Table 4.1). The white dashed line marks the fault that bounds the NW-shore. This fault steps to the right at the NE end of the lake. The maximum estimated height of the scarp in view is ~15 m. b) Horst west of Red River, looking SW. White dashed lines mark the base of the foreground fault scarp of the horst pair. The white arrow marks the top of the background fault scarp. The maximum estimated height of the foreground scarp at this location is ~5 m.

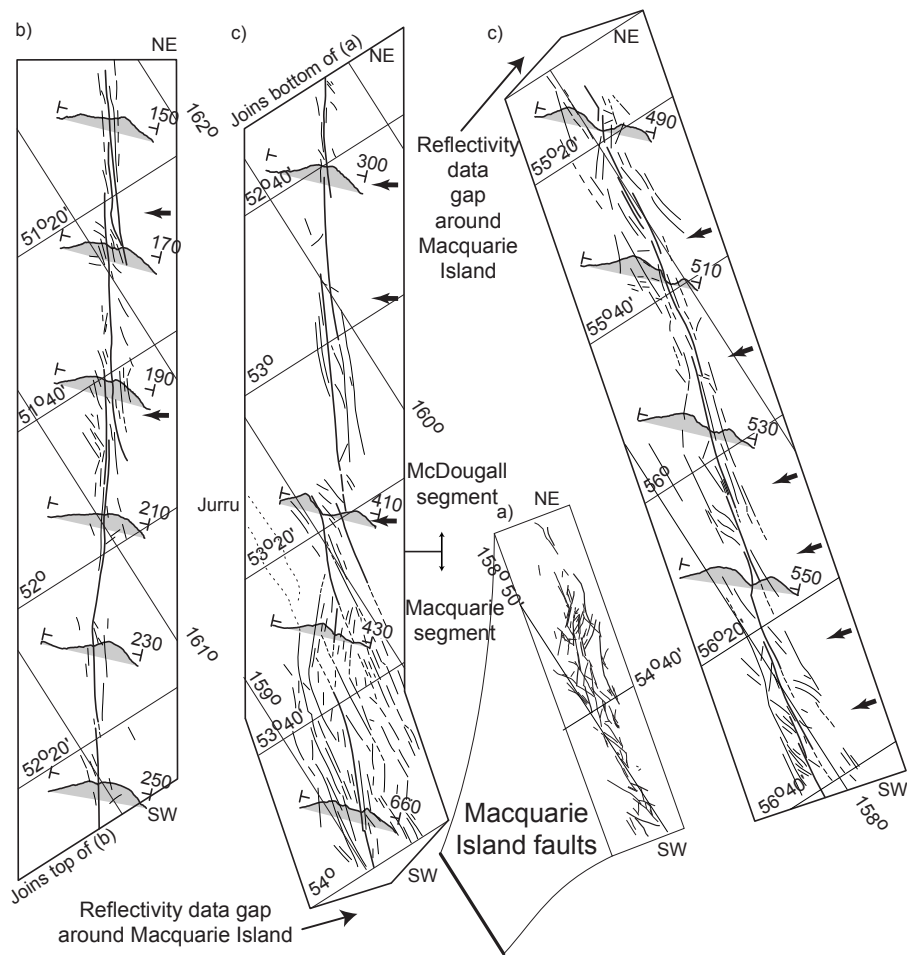


Figure 4.8. Recent fault patterns. a) Fault pattern on Macquarie Island observed in reflectivity data gap shown with geophysical interpretation of Daczko (modified from Daczko et al., 2003). Thick black line at southwestern end of Figure 4.8c indicates length and general longitude of Macquarie Island data strip. Note northern faults (above  $\sim 54^{\circ}40'$  S) are NNE- to NE-striking, similar to those in the seafloor at southwestern end of Figure 4.8b, whereas those to the southwest are N- to NW-striking similar seafloor faults in Figure 4.8d. The McDougall and Macquarie segments of the Australian-Pacific plate boundary interpreted from reflectivity data between  $51^{\circ}05'$  S and  $56^{\circ}40'$  S. Bathymetric profiles (V.E. = 1.75) compiled from interpreted 8-channel seismic reflection data are presented as grey shaded sections ( $\sim 21$  km long). R/V Rig Seismic reflection line numbers are indicated. Thick black line is the interpreted location of the active Australian-Pacific plate boundary. Thin black lines are associated lineaments. Black arrows indicate locations of en echelon right step-overs in the plate boundary.

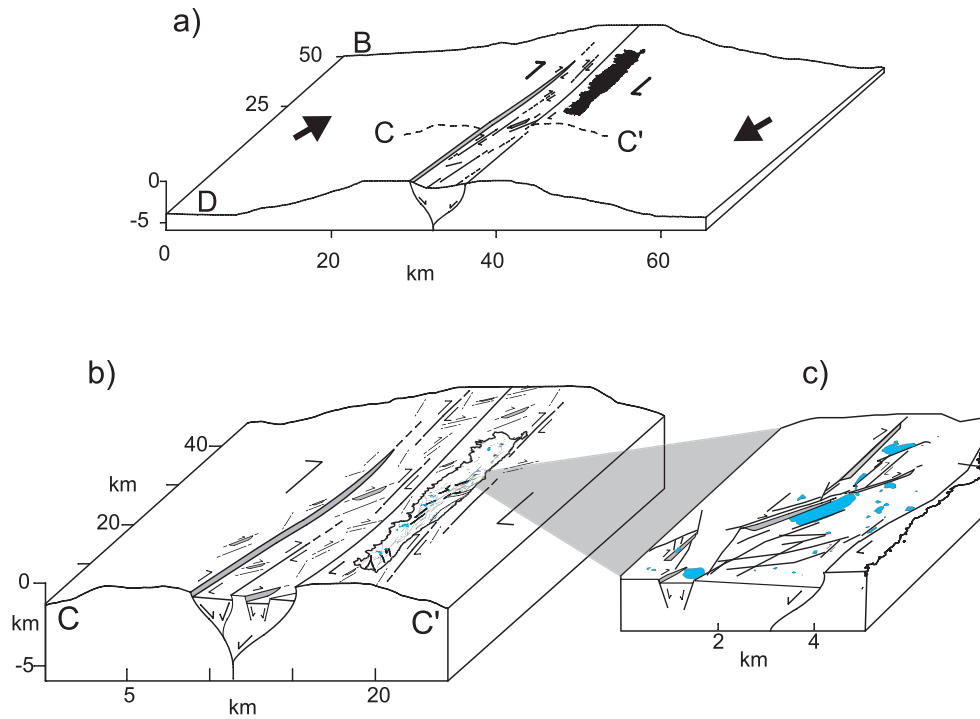


Figure 4.9. Block diagrams. a, b) Block diagram model of the faulting patterns on the Macquarie segment of the MRC (bathymetric profile V.E.=1) near Macquarie Island. Thick black arrows represent plate motion vectors that are  $\sim 20^\circ$  oblique to the plate boundary (a and b from Daczko et al., 2003). c) Detail shows Macquarie Island block diagram, showing Prion Lake and surrounds. The fault pattern on the island is identical to that seen on the seafloor.

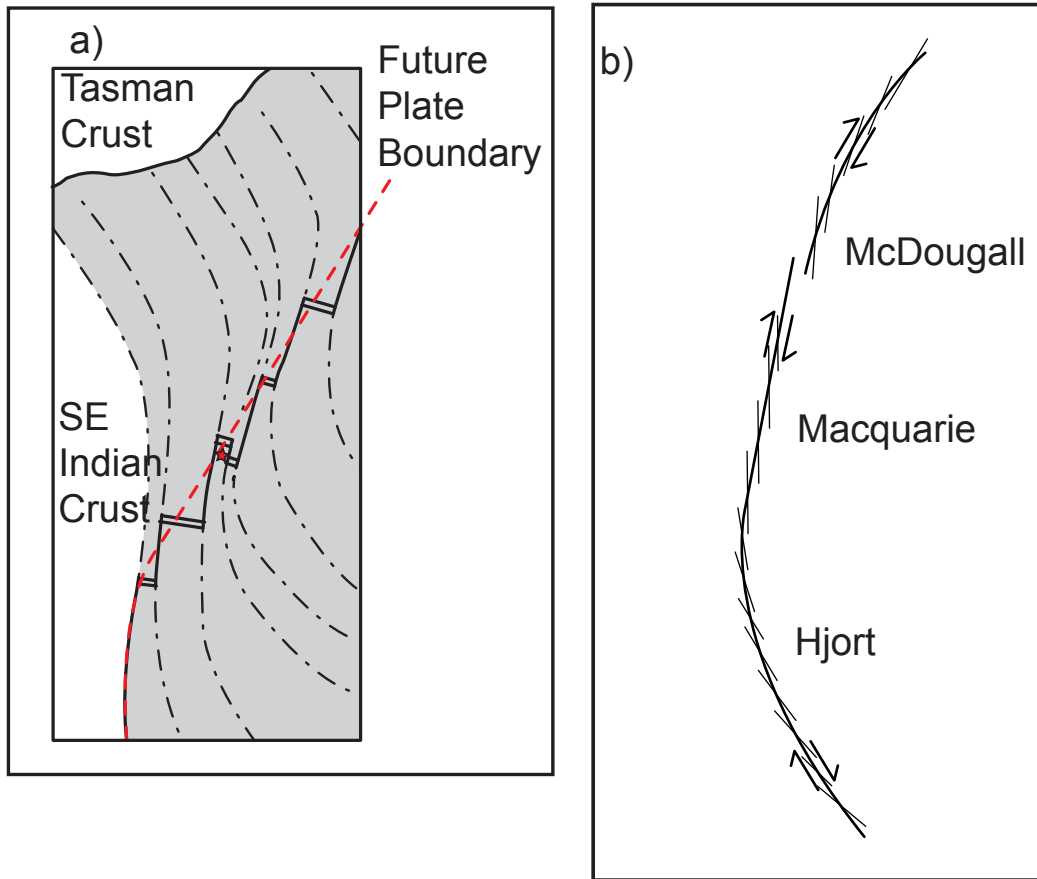


Figure 4.10. Recent fault model. a) Cartoon interpretation of the plate boundary geometry at ~10 Ma when spreading ceased. Gray area shows crust formed at the Macquarie spreading center between ~40 and ~10 Ma. Small red star locates our best estimate of where Macquarie Island formed. b) Summary diagram showing the overall pre-existing curvature to the Australian-Pacific plate boundary and echelon right lateral plate boundary faults that formed conforming to this geometry. Curvature on the McDougall segment, angle between plate boundary faults and plate boundary are exaggerated. Modified from Daczko et al., (2003).

Table 4.1a Recent fault data. Rock units: P = pillow basalt, D = sheeted dikes, M = peridotite. Locations: BP = Brothers Point, DPP = Davis Point Plateau, GL = Gratitude Lake, GG = Green Gorge, LI = Lake Ifould, PL = Prion Lake, WBP = Waterfall Bay Plateau, HP = Hurd Point, LA = Lake Ainsworth, WL = Waterfall Lake, MJ = Mt. Jeffryes, WR = Windy Ridge, ML = Major Lake, TL = Tulloch Lake, SL = Square Lake, ME = Mt. Elder. All fault locations are numbered on Figures 4.2, 4.3.

Fault #	Length (m)	Strike	block	Uphrown	Throw (m)	Rock Unit	Location	Comment
1	4300	030	120	100	P-D	BP	Brothers fault at Brothers Point	
2	2400	200	290	10	P	DPP	Davis lake	
3	300	166	256	0	P	DPP	Offsets Davis lake fault (2 and 4)	
4	2000	225	315		P	DPP	Continuation of Davis lake fault	
5	1600	220	310	8	P	GL	Gratitude lake	
6	20	105	195		P	GG	Brothers fault graben 1	
7	20	110	200	2	P	GG	Brothers fault graben 2	
8	20	290	020	10	P	GG	Brothers fault graben 2	
9	20	110	200	10	P	GG	Brothers fault graben 3	
10	20	290	020	6	P	GG	Brothers fault graben 3	
11	25	120	210	6	P	GG	Brothers fault graben 4a	
12	25	300	030		P	GG	Brothers fault graben 4a	
13	5	100	190	6	P	GG	Brothers fault graben 4b	
14	5	280	010		P	GG	Brothers fault graben 4b	
15	20	110	200	2	P	GG	Brothers fault graben 5	
16		090	180		P	GG	Brothers fault graben 6	
17	7400	018	108	150	P	GG	Brothers fault from GG to PL	
18	1000	060	150	10	P	GG	N end of fault, switches upthrown midway	

Table 4.1b Recent fault data. Rock units: P = pillow basalt, D = sheeted dikes, M = peridotite. Locations: BP = Brothers Point, DPP = Davis Point Plateau, GL = Gratitude Lake, GG = Green Gorge, LI = Lake Ifould, PL = Prion Lake, WBP = Waterfall Bay Plateau, HP = Hurd Point, LA = Lake Ainsworth, WL = Waterfall Lake, MJ = Mt. Jeffryes, WR = Windy Ridge, ML = Major Lake, TL = Tulloch Lake, SL = Square Lake, ME = Mt. Elder. All fault locations are numbered on Figures 4.2, 4.3.

Fault #	Length (m)	Strike	block Upthrown	Throw (m)	Rock Unit	Location	Comment
19	1000	240	330	10	P	GG	S end of fault, switches upthrown midway
20	1600	025	115	30	P	LI	Lake Ifould fault east bank, wave cut platform
21	1600	205	295		P	LI	Lake Ifould fault, west bank
22	3300	225	315	50	P	PL	Prion NW, height ranges from 5-50 m, from NE-SW
23	1000	035	125		P	PL	Prion SE a
24	2200	045	135	50	P	PL	Prion SE b, varies in throw from 1-50, NE-SW
25	800	045	135	10	P	WBP	Plateau W of WB, near layered picrite along track
26	3000	344	074	5	P	HP	N-most end throw increases to 20m, controls drainage, truncates 27 and 28
27	500	012	102	4	P	HP	Small fault parallel to Brothers system
28	1000	020	110	5	P	HP	East of 27
29	450	342	072	5	P	HP	Truncates 28
30	500	185	275	10	P	LA	Lake Ainsworth fault
31	2000	320	050	10	P	HP	Fault that veers out from SE bay. Dies out to the NW
32	500	313	043	5	P	WL	Little fault S of WL
33	1200	030	120	10	P	WL	Bounds small lake S of WL
34	1200	020	110	20	P	MJ	Mt Jeffryes fault, decreases to 5 m to S

Table 4.1c Recent fault data. Rock units: P = pillow basalt, D = sheeted dikes, M = peridotite. Locations: BP = Brothers Point, DPP = Davis Point Plateau, GL = Gratitude Lake, GG = Green Gorge, LI = Lake Ifould, PL = Prion Lake, WBP = Waterfall Bay Plateau, HP = Hurd Point, LA = Lake Ainsworth, WL = Waterfall Lake, MJ = Mt. Jeffryes, WR = Windy Ridge, ML = Major Lake, TL = Tulloch Lake, SL = Square Lake, ME = Mt. Elder. All fault locations are numbered on Figures 4.2, 4.3.

Fault #	Length (m)	Strike	block	Uplifted	Throw (m)	Rock Unit	Location	Comment
35	1600	325	055	10	P	MJ	Mt Jeffryes, truncates 34	
36	800	327	057	5	P	WR	Windy Ridge horst, S	
37	800	147	237	5	P	WR	Windy Ridge horst, N	
38	600	155	245	10	D-P	ML	Enters major lake, dies quickly	
39	400	005	095	5	P	WBP	Westernmost of curved faults	
40	190	350	080	5	P	WBP	have split into 2 faults at bend	
41	450	345	075	5	P	WBP	2nd from west	
42	550	005	095	5	P	WBP	3rd from W, N end	
43	230	335	065	5	P	WBP	S end	
44	530	005	095	5	P	WBP	Easternmost fault, N	
45	230	335	065	2	P	WBP	S end	
46	410	360	090	10	P	WBP	This and next two are related, hard to follow	
47	730	340	070	5	P	WBP		
48	960	355	085	5	P	WBP		
49	900	040	130	50	P	TL	Tulloch Lake	
50	3000	008	278	20	P	SL	Square Lake	
51	1300	010	100	40	M	ME	Mt Elder	

## SUMMARY AND MODEL

### Summary

Macquarie Island provides an exceptional opportunity to observe seafloor processes and features on land where the tectonic context is preserved in the surrounding seafloor. Data from this structural and geochemical field based study combined with marine geophysical data advance our understanding of the evolution of the Australian-Pacific plate boundary in the vicinity of Macquarie Island, a region where seafloor spreading shut down and evolved into a transpressional plate boundary.

Structural analyses were completed of both seafloor spreading-related faults and mylonites as well as uplift-related faults on the island. Both field data sets were related to faults mapped in the seafloor from geophysical data. Seafloor magmatism preserved on the island was studied via geochemical analysis of basalts and residual mantle peridotites in conjunction with field relationships. Evidence was found for periods of both low melt supply volcanism and high melt supply volcanism, which could be connected to an evolving magmatic system as spreading was shutting down on the paleo-Macquarie spreading ridge.

In chapter one, structural, sedimentological, mineralogical, and marine geophysical data were presented. The Finch-Langdon fault zone—on the basis of the fault pattern, mineralization, and associated sedimentary deposits, coupled with the tectonic setting documented by swath reflectivity and bathymetry data—is best explained as having formed in an inside corner of an active ridge-transform

intersection near the end of seafloor spreading. Uplift of lower crust and mantle sections on the seafloor occurs during periods when spreading rates are slow, magmatism is low, and spreading is primarily accommodated by extensional faulting.

In chapter two, geochemical data from residual mantle peridotites were presented. Macquarie Island peridotites are uniformly depleted harzburgites with few cpx porphyroclasts, high spinel Cr-numbers close to 0.5 and low HREE contents in cpx. This depletion is similar to depleted residual mantle rocks from the high melt volume, fast spreading ridges. Alternatively, the unique tectonic setting of Macquarie Island may have exposed peridotites that were generated at a segment center of a slow spreading ridge, as this would have more depleted residues than at a low-melt-supply segment end.

In addition, Macquarie Island peridotites have LREE-enriched cpx and some samples have a pronounced positive Sr anomaly. Such chemical signatures are not found in any abyssal peridotite, but have been reported in mantle sections of ophiolites. This similarity suggests that these fluid-mobile elements may have been contributed to the Macquarie Island peridotites through contamination by ancient subduction, which is also compatible with the high HREE and Al depletion. Alternately, I proposed that this signature is not contributed by subduction, but can also be caused by other factors that have not yet been recognized.

Basalts on the island have a distinctly different geochemical signature from the peridotites. Chapter three presented the first spatial and temporal

geochemical study of the basalts of Macquarie Island. The oldest basalts exhibit a steady decline in concentration of incompatible elements with time. These eruptions are followed by a sequence of basalts with varying incompatible element enrichment, with alternating enriched and less-enriched eruptions. This is followed by a period of relatively constant compositions. As E-MORBs, the basalts formed during low melt production typically associated with slow spreading, but also show a trend of decreasing incompatible element enrichment and increasing melting with time, which may reflect acceleration in spreading rate, and/or development of a magmatic system.

Magmatism ended at ~6 Ma, when transform-related faults cut across the remaining short spreading centers. Chapter four presents structural data from the recent faults of Macquarie Island that records deformation associated with transpression along the boundary. Recent faulting on the island reflects dominantly extensional tectonics, apparently in conflict with the island's transpressional tectonic setting and history of uplift. Faults cut across and rarely reactivate seafloor spreading related faults; the faults cannot be attributed to secondary faulting along a transpressional boundary. Instead, the recent faulting is dominated by normal faults forming pull apart basins and complex transfer zones where displacement is transferred. These faults are analogous to those on the seafloor where extensional tectonics within relay zones dominates in transfer zones between step-overs in lateral faults. Integrating the island data with results from a marine geophysical investigation of the plate boundary by Nathan Daczko

suggests that a stepped geometry formed to accommodate the inherited curved geometry of the Australian-Pacific plate boundary.

Below I propose a possible tectonic model that explains the combined structural and geochemical results.

### **A geologic model for Macquarie Island**

Macquarie Island represents oceanic crust/upper mantle uplifted in situ that formed during the last stages of spreading prior to the onset of transform motion along the Australia-Pacific plate boundary at ~6 Ma. Structural, geochemical, and field data from Macquarie Island and geophysical data from the surrounding seafloor, when considered together, are incompatible with a simple spreading ridge model and are best reconciled by a model incorporating ridge propagation.

Combined structural and geophysical data support formation of seafloor structures on the island in an inside corner of a ridge-transform intersection with the ridge north of the island (Figure 1.12). Geophysical data show a NNE-trending fracture zone with orthogonal spreading fabric to the east of the island (Figure 4.13). The primary seafloor spreading fault exposed on the island, the Finch-Langdon fault, is composed of fault segments that trend ~NNE-NNW, WNW, and NW; it juxtaposes sheeted dikes, gabbro and peridotite against volcanic rocks. Steeply-dipping faults with sub-horizontal mineral slickenlines indicate oblique- or strike-slip motion (Figure 1.3). Sheeted dikes and steep gabbro mylonite zones generally trend WNW. Thick talus breccias contain clasts of gabbro (Figure 1.11) and clasts of mineralized fault breccia, indicating that

faulting was occurring on the seafloor. The volcanic rocks are overturned adjacent to the fault, attaining more moderate dips with distance, indicating that they may have been rotated while eruptions were occurring.

As an inside-corner massif, the Macquarie Island northern plateau region is rather small, at ~5 km by ~8 km. “Mega-mullions” or “RTI massifs” can reach many 1000’s of km<sup>2</sup> in extent, as seen in the Parece Vela back-arc basin (Ohara et al., 2001), although this is rather unusual. Generally they are much smaller, around 20 or 30 km in length and width at most (Mitchell et al., 1998) and can be as small as <10 km across (Blackman et al., 1998) as seen on the Mid Atlantic Ridge. They are seen not only immediately at the RTI but also at a distance along the transform, where fossil massifs are seen that have been transported away from the RTI (Blackman et al., 1998) by continued spreading, their formation disrupted by renewed magmatism. It is likely that the size of these massifs is proportional to the duration of amagmatic extension in the system, with very large massifs developing during long amagmatic periods. A relationship between the size of the massif and the length of the spreading segment would also be expected, whereby larger features would develop on longer spreading segments. On Macquarie Island, we have evidence of significant, albeit sporadic, magmatism, as well as a very short spreading segments, thus a smaller RTI massif is to be expected.

There is no evidence of a major, low-angle ductile shear zone on Macquarie Island, like those that have been postulated to be the mechanism for the exposure of the upper mantle and lower crust on the seafloor at other inside

corner highs. It is difficult to explain how such deep rocks could have been exposed on the seafloor without a large detachment, yet there is no evidence for such a structure, nor for the large-scale corrugations seen on the surfaces of these structures on the seafloor (e.g., Smith et al., 1997). It is possible that there once was a detachment surface, but the low angle ductile fabric was eroded during uplift of the island. Alternately, it is possible that such a fabric does exist, but is completely obscured by Quaternary deposits on the island plateau. The seafloor faults of the F-L fault would have formed at a high angle to such a detachment, disrupting the low-angle surface, forming the pattern of faults seen on the island, a pattern also seen at RTIs on the seafloor (e.g., Macdonald et al., 1986). The mylonites are also steeply dipping, with steeply plunging stretching lineations, and it is likely that they formed in response to motion on the steep RTI faults. Mylonites and submarine faults of different temperature-pressure regimes are exposed at the same topographic level, which is unexpected, but this can be explained by uplift of the mylonites concurrent with brittle faulting at higher crustal levels and reactivation of the brittle faults, which is described in the model outlined in subsequent paragraphs.

Geochemical and field data also indicate a more complex evolution than simple seafloor spreading. The basalts and peridotites are not related to each other geochemically. Peridotites uplifted by the fault have high Cr-numbers (Figure 2.4), anomalous Sr, HREE depletion, and LREE enrichment (Figures 2.6, 2.8). Basalts have a distinctly different geochemical signature; E-MORBs with a wide range of enrichment show a progressive decrease in enrichment with time and

periods of alternating enriched and less-enriched eruptions followed by periods of relatively constant compositions (Figure 3.3). Basalts in the center of the island are associated with primitive picrites and evolved amphibole-bearing basalts. Upright eruptive centers are preserved on the island (Figure 3.5), which is unexpected near large detachment faults.

In the uplifted block, diabase dikes cut diabase, two generations of diabase dikes cut gabbro and peridotite, gabbro also intrudes peridotite, indicating that uplift was concurrent with magmatism. Sedimentary rocks interbedded with extensive volcanics south of the fault contain gabbro clasts, indicating gabbro was exposed on the seafloor during active volcanism.

Ridge propagation through or near an inside corner high exposing lower crust/uppermost mantle, as is seen on the Mid-Atlantic Ridge at 5°S (Reston et al., 2002), provides a means to unite this seemingly conflicting data.

Stage 1: The first stage of the model is a mature ridge with steady-state magmatism that produced the Hurd Point basalts, and possibly caused the depletion in the peridotites (Figure A.1a).

Stage 2: Magmatism slowed, perhaps in response to the shifting plate motions, and faulting commenced, initiating possible detachment faulting. In this stage, within the inside corner of a ridge-transform intersection, the original F-L fault geometry formed in conjunction with uplift of the deeper rocks by detachment faulting and formation of steeply dipping gabbro mylonites (Figure A.1b). Both the steep F-L faults and the steep mylonites would have formed at a high angle to the detachment fault.

Stage 3: As the spreading system accommodated the changes in relative plate motion, the ridge segments became unstable, and an adjacent eastern ridge segment began to propagate. As propagation continued, the ridge cut either through or adjacent to the crust uplifted within the inside corner high (Figure A.1c) causing the cessation of magmatism on the original spreading segment and the initiation of new volcanism. These eruptions would be from small melt batches with melting occurring in a deeper, more enriched source than the uplifted depleted peridotite. In addition, some shallow melting occurred, that allowed for rapid fractionation of some magmas. Initial eruptions were primitive (e.g., picrites) and/or bimodal with some more evolved lavas erupted as well (e.g., amphibole-bearing units with picrites), as seen beneath the Pyramid Peak and in the Major Lake sections. As the magmatic system developed and more magma bodies formed, more variable magma compositions were produced, expressed in eruptions of E-MORBs of varying incompatible element enrichments and some additional amphibole bearing units, like those seen in the Bauer Bay basalts. This pattern is seen in the vicinity of seafloor propagating ridge tips like the Galapagos spreading center (Christie and Sinton, 1981, 1986) and in regions where propagation has been proposed, like the Jan Mayan Platform and Mohs Ridge (Haase, 1996), one of the few places where magmatic amphibole has been recovered in MORB. As the magmatic system develops in the new rift, compositions become less variable as the effective spreading rate increases, more melt is produced, and the individual magma bodies become connected facilitating

mixing, with the basalt compositions approaching the normal compositions of the original spreading ridge.

Also in stage 3, new gabbro and diabase intruded the peridotite, while diabase intruded gabbro. The original corner structure faults were re-activated, creating the sub-horizontal mineral slickenlines and shedding talus to the south into the newly forming volcanic section associated with the propagating ridge, which included the preserved volcanoes in the center of the island. Gabbro mylonites that originally formed in steep orientations at greater depths were uplifted to the same level as lower-temperature hydrothermal faults.

The plate motions continued to change and finally, the spreading regime ended, and magmatism ceased. Faults related to transform motion exploited the curved plate boundary geometry, cutting through in an en echelon pattern. Transpression caused flexure of the plate boundary, and the Macquarie Ridge rose, ultimately breaching the surface of the sea with its apex, a small island in the Southern Ocean, known as Macquarie.

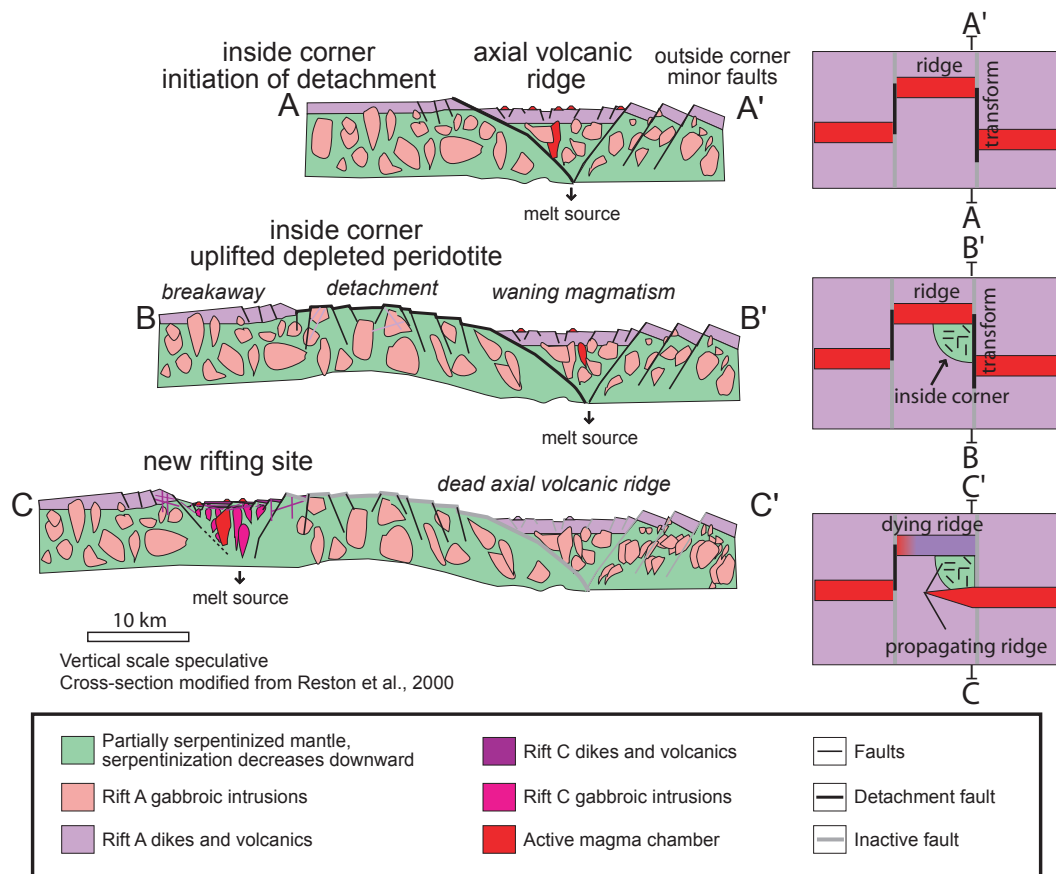


Figure A.1. Ridge propagation model. a) Normal spreading with the initiation of a detachment fault. b) Magmatism slows allowing the F-L fault detachment to develop. c) As the spreading direction changes the ridge segments become unstable, and an adjacent eastern ridge segment begins to propagate. As propagation continues, the ridge cuts through or adjacent to the crust uplifted within the inside corner high causing the cessation of magmatism on the original spreading segment and new volcanism begins. Initial eruptions have variable compositions, with E-MORBs of varying incompatible element enrichments as well as evolved, amphibole bearing basalts and primitive picrites. New gabbro and diabase intrude the peridotite, and diabase intrudes gabbro. The original corner structure faults are re-activated, shedding talus into the newly forming volcanic section.

## References

- Adamson, D.A., Selkirk, P.M., Price, D.M., Ward, N., and Selkirk, J.M., 1996, Pleistocene uplift and paleoenvironments of Macquarie Island: evidence from Paleobeaches and sedimentary deposits: *Papers and Proceedings of the Royal Society of Tasmania*, v. 130, p. 25-32.
- Alexander, R.J., and Harper, G.D., 1992, The Josephine Ophiolite; an ancient analogue for slow- to intermediate-spreading oceanic ridges: *Geological Society Special Publications*, v. 60, p. 3-38.
- Allerton, S., and Vine, F.J., 1992, Deformation styles adjacent to transform faults; evidence from the Troodos Ophiolite, Cyprus: *Geological Society Special Publications*, v. 60, p. 251-261.
- Alt, J.C., 1999, Hydrothermal alteration and mineralization of oceanic crust; mineralogy, geochemistry, and processes: *Reviews in Economic Geology*, v. 8, p. 133-155.
- Alt, J.C., Davidson, G.J., Teagle, D.A.H., and Karson, J.A., 2003, Isotopic composition of gypsum in the Macquarie Island Ophiolite; implications for the sulfur cycle and the subsurface biosphere in oceanic crust: *Geology Boulder*, v. 31, p. 549-552.
- Anders, E., and Grevesse, N., 1989, Abundances of the elements: meteoric and solar: *Geochimica et Cosmochimica Acta*, v. 53, p. 197-214.
- Anonymous, 2000, Macquarie Island; inscribed on the World Heritage List in 1997: Australia, Environment Australia : Canberra, A.C.T., Australia.
- Aydin, A., and Schultz, R.A., 1990, Effect of mechanical interaction on the development of strike-slip faults with echelon patterns: *Journal of Structural Geology*, v. 12, p. 123-129.
- Batanova, V.G., Suhr, G., and Sobolev, A.V., 1998, Origin of geochemical heterogeneity in the mantle peridotites from the Bay of Islands Ophiolite, Newfoundland, Canada; ion probe study of clinopyroxenes: *Geochimica et Cosmochimica Acta*, v. 62, p. 853-866.

- Bazylev, B.A., and Kamenetsky, V.S., 1998, Genesis of peridotites from the ophiolite complex of Macquarie Island, southwestern Pacific Ocean: *Petrology*, v. 6, p. 335-350.
- Bernardel, G., and Symonds, P., 2001, Seafloor mapping of the South-east Region and adjacent waters: AUSTREA final report: southern Macquarie Ridge: Australian Geological Survey Organisation Record, v. 2001/46.
- Bizimis, M., Salters, V.J.M., and Bonatti, E., 2000, Trace and REE content of clinopyroxenes from supra-subduction zone peridotites; implications for melting and enrichment processes in island arcs: *Chemical Geology*, v. 165, p. 67-85.
- Blackman, D.K., Cann, J.R., Janssen, B., and Smith, D.K., 1998, Origin of extensional core complexes; evidence from the Mid-Atlantic Ridge at Atlantis fracture zone: *Journal of Geophysical Research*, v. 103, p. 315-21.
- Bodinier, J.L., Vasseur, G., Vernieres, J., Dupuy, C., and Fabries, J., 1990, Mechanisms of mantle metasomatism: geochemical evidence from the Lherz orogenic peridotite: *Journal of Petrology*, v. 31, p. 597-628.
- Buchan, C., Cunningham, D., Windley, B.F., and Tomurhuu, D., 2001, Structural and lithological characteristics of the Bayankhongor Ophiolite Zone, Central Mongolia: *Journal of the Geological Society*, v. 158, p. 445-460.
- Büchl, A., Brugmann, G., Batanova, V.G., Munker, C., and Hofmann, A.W., 2002, Melt percolation monitored by Os isotopes and HSE abundances: a case study from the mantle section of the Troodos Ophiolite: *Earth and Planetary Science Letters*, v. 204, p. 385-402.
- Cande, S.C., and Stock, J.M., in review, Pacific-Antarctic-Australia motion and the formation of the Macquarie plate: *Geophysical Journal International*.
- Cande, S.C., Stock, J.M., Muller, R.D., and Ishihara, T., 2000, Cenozoic motion between East and West Antarctica: *Nature*, v. 404, p. 145-150.
- Cannat, M., Lagabrielle, Y., Bougault, H., Casey, J., de Coutures, N., Dmitriev, L., and Fouquet, Y., 1997, Ultramafic and gabbroic exposures at the Mid-Atlantic Ridge; geological mapping in the 15 degrees N region: *Tectonophysics*, v. 279, p. 193-213.

- Cannat, M., and Seyler, M., 1995, Transform tectonics, metamorphic plagioclase and amphibolitization in ultramafic rocks of the Vema transform fault (Atlantic Ocean): *Earth and Planetary Science Letters*, v. 133, p. 3-4.
- Casas, A.M., 2001, Analogue models of transpressive systems: *Journal of Structural Geology*, v. 23, p. 733-743.
- Charpentier, S., 2000, La zone de transition continent-ocean de la marge continentale passive ouest-iberique: etudes petrologique et geochemique des roches magmatiques et mantelliques [Dr.-thesis]: Clermont-Ferrand, Universite Blaise Pascal.
- Christie, D.M., and Sinton, J.M., 1981, Evolution of abyssal lavas along propagating segments of the Galapagos spreading center: *Earth and Planetary Science Letters*, v. 56, p. 321-335.
- , 1986, Major element constraints on melting, differentiation and mixing of magmas from the Galapagos 95.5 degrees W propagating rift system: *Contributions to Mineralogy and Petrology*, v. 94, p. 274-288.
- Christodoulou, C., 1994, Mineralogy of the Macquarie Island plutonic suite; fractionation processes at shallow level magma chambers and controls on basalt major element chemistry: *Ofioliti*, v. 19, p. 217-245.
- Christodoulou, C., Griffin, B.J., and Foden, J., 1984, The geology of Macquarie Island: Australian National Antarctic Research Expeditions Research Notes, v. 21, p. 1-15.
- Collette, B.J., 1986, Fracture zones in the North Atlantic; morphology and a model: *Journal of the Geological Society of London*, v. 143, p. 763-777.
- Daczko, N.R., Wertz, K.L., Mosher, S., Coffin, M.F., and Meckel, T.A., 2003, Extension along the Australian-Pacific transpressional transform plate boundary near Macquarie Island: *Geochemistry, Geophysics, Geosystems*, v. 41.
- Danyushevsky, L.V., Eggins, S.M., Falloon, T.J., and Christie, D.M., 2000, H<sub>2</sub>O abundance in depleted to moderately enriched mid-ocean ridge magmas; Part I, Incompatible behaviour, implications for mantle storage, and origin of regional variations: *Journal of Petrology*, v. 41, p. 1329-1364.

- Dick, H.J.B., 1989, Abyssal peridotites, very slow spreading ridges and ocean ridge magmatism: Geological Society Special Publications, v. 42, p. 71-105.
- Dick, H.J.B., and Bullen, T., 1984, Chromian spinel as a petrogenetic indicator in abyssal and alpine-type peridotites and spatially associated lavas: Contributions to Mineralogy Petrology, v. 86, p. 54-76.
- Dick, H.J.B., and Natland, J.H., 1996, Late-stage melt evolution and transport in the shallow mantle beneath the East Pacific Rise: Proceedings of the Ocean Drilling Program, Scientific Results, v. 147, p. 103-134.
- Duncan, R.A., and Varne, R., 1988, The age and distribution of the igneous rocks of Macquarie Island: Papers and Proceedings of the Royal Society of Tasmania, v. 122, p. 45-50.
- Einaudi, F., Godard, M., Pezard, P., Cocheme, J.J., Coulon, C., Brewer, T., and Harvey, P., 2003, Magmatic cycles and formation of the upper oceanic crust at spreading centers: Geochemical study of a continuous extrusive section in the Oman ophiolite: Geochemistry, Geophysics, Geosystems, v. 4.
- Fox, P.J., and Gallo, D.G., 1984, A tectonic model for ridge-transform-ridge plate boundaries; implications for the structure of oceanic lithosphere: Tectonophysics, v. 104, p. 205-242.
- Frohlich, C., Coffin, M.F., Massell, C., Mann, P., Schuur, C.L., Davis, S.D., Jones, T., and Karner, G., 1997, Constraints on Macquarie Ridge tectonics provided by Harvard focal mechanisms and teleseismic earthquake locations: Journal of Geophysical Research, v. 102, p. 5029-5041.
- Gallo, D.G., Fox, P.J., and Macdonald, K.C., 1986, A Sea Beam investigation of the Clipperton transform fault; the morphotectonic expression of a fast slipping transform boundary: Journal of Geophysical Research, v. 91, p. 3455-3467.
- Gente, P., Pockalny, R., A., Durand, C., Deplus, C., Maia, M., Ceuleneer, G., Mevel, C., Cannat, M., and Laverne, C., 1995, Characteristics and evolution of the segmentation of the Mid-Atlantic Ridge between 20 degrees N and 24 degrees N during the last 10 million years: Earth and Planetary Science Letters, v. 129, p. 55-71.

- Ghose, I., Cannat, M., and Seyler, M., 1996, Transform fault effect on mantle melting in the MARK area (Mid-Atlantic Ridge south of the Kane transform): *Geology*, v. 24, p. 1139-1142.
- Godard, M., Bodinier, J.L., and Vasseur, G., 1995, Effects of mineralogical reactions on trace element redistributions in mantle rocks during percolation processes: a chromatographic approach: *Earth and Planetary Science Letters*, v. 133, p. 449-461.
- Goscombe, B.D., and Everard, J.L., 1998, *Geology of Macquarie Island*: Hobart, Australia, Mineral Resources of Tasmania.
- , 2001, Tectonic evolution of Macquarie Island: extensional structures and block rotations in oceanic crust: *Journal of Structural Geology*, v. 23, p. 639-673.
- Griffin, B.G., and Varne, R., 1978, The petrology of the Macquarie Island ophiolite association; mid-Tertiary oceanic crust of the Southern Ocean: *Ophioliti*, v. 3, p. 230-231.
- Griffin, B.J., and Varne, R., 1983, The Macquarie Island ophiolite complex; major and trace element geochemistry of the lavas and dykes, in Oliver, R.L., James, P.R., and Jago, J.B., eds., *Antarctic earth science; fourth international symposium*: United Kingdom, Cambridge Univ. : Cambridge, United Kingdom, p. 659.
- Gruau, G., Bernard-Griffiths, J., and Lecuyer, C., 1998, The origin of U-shaped rare earth patterns in ophiolite peridotites: Assessing the role of secondary alteration and melt/rock reaction: *Geochimica Et Cosmochimica Acta*, v. 62, p. 3545-3560.
- Haase, K.M., 1994, The petrology and geochemistry of Vesteris Seamount, Greenland Basin; an intraplate alkaline volcano of non-plume origin: *Journal of Petrology*, v. 35, p. 295-328.
- , 1996, Geochemistry of lavas from Mohns Ridge, Norwegian-Greenland Sea; implications for melting conditions and magma sources near Jan Mayen: *Contributions to Mineralogy and Petrology*, v. 123, p. 223-237.
- Haase, K.M., Muhe, R., and Stoffers, P., 2000, Magmatism during extension of the lithosphere: geochemical constraints from lavas of the Shaban Deep, northern Red Sea: *Chemical Geology*, v. 166, p. 225-239.

- Hamlyn, P., R., and Bonatti, E., 1980, Petrology of mantle-derived ultramafics from the Owen Fracture Zone, Northwest Indian Ocean: implications for the nature of the oceanic upper mantle: *Earth and Planetary Science Letters*, v. 48, p. 65-79.
- Harper, G.D., 1980, The Josephine Ophiolite; remains of a Late Jurassic marginal basin in northwestern California: *Geology Boulder, July*, v. 8, p. 333-337.
- , 1984, The Josephine ophiolite, northwestern California: *Geological Society of America Bulletin*, v. 95, p. 1009-1026.
- Harper, G.D., Bowman, J.R., and Kuhns, R.J., 1988, A field, chemical, and stable isotope study of subseafloor metamorphism of the Josephine Ophiolite, California-Oregon: *Journal of Geophysical Research*, v. 93, p. 4625-4656.
- Hart, S.R., 1993, Equilibration during mantle melting - a fractal tree model: *Proceedings of the National Academy of Sciences of the United States of America*, v. 90, p. 11914-11918.
- Hayes, D.E., and Talwani, M., 1973, The Macquarie Ridge Complex, *Oceanography of the South Pacific 1972: New Zealand, N. Z. Comm. Unesco, Wellington*, p. 339.
- Hellebrand, E., and Snow, J., in press, Deep melting and sodic metasomatism underneath the highly oblique-spreading Lena Trough (Arctic Ocean): *Earth and Planetary Science Letters*.
- Hellebrand, E., Snow, J.E., Dick, H.J.B., and Hofmann, A.W., 2001, Coupled major and trace elements as indicators of the extent of melting in mid-ocean ridge peridotites: *Nature*, v. 410, p. 677-681.
- Hellebrand, E., Snow, J.E., Hoppe, P., and Hofmann, A.W., 2002a, Garnet-field melting and late-stage refertilization in 'residual' abyssal peridotites from the Central Indian Ridge: *Journal of Petrology*, v. 43, p. 2305-2338.
- Hellebrand, E., Snow, J.E., and Mühe, R., 2002b, Mantle melting beneath the Gakkel Ridge (Arctic Ocean): abyssal peridotite spinel compositions: *Chemical Geology*, v. 182, p. 227-235.
- Johnson, K.T.M., Dick, H.J.B., and Shimizu, N., 1990, Melting in the oceanic upper mantle; an ion microprobe study of diopsides in abyssal peridotites: *Journal of Geophysical Research*, v. 95, p. 2661-2678.

- Kamenetsky, V.S., 2000, Enriched end-member of primitive MORB melts; petrology and geochemistry of glasses from Macquarie Island (SW Pacific): *Journal of Petrology*, v. 41, p. 411-430.
- Kamenetsky, V.S., and Maas, R., 2002, Mantle-melt Evolution (Dynamic Source) in the Origin of a Single MORB Suite: a Perspective from Magnesian Glasses of Macquarie Island: *Journal of Petrology*, v. 43, p. 1909-1922.
- Karson, J.A., 1984, Variations in structure and petrology in the Coastal Complex, Newfoundland; anatomy of an oceanic fracture zone: *Geological Society Special Publications*, v. 13, p. 131-144.
- Karson, J.A., and Dick, H.J.B., 1983, Tectonics of ridge-transform intersections at the Kane fracture zone: *Marine Geophysical Researches*, v. 6, p. 51-98.
- Kastens, K.A., Ryan, W.B.F., Fox, P.J., and Macdonald, K.C., 1986, Structural and volcanic expression of a fast slipping ridge-transform-ridge-plate boundary; Sea MARC I and photographic surveys at the Clipperton transform fault: *Journal of Geophysical Research*, v. 91, p. 3469-3488.
- Kelemen, P.B., Hirth, G., Shimizu, N., Spiegelman, M., and Dick, H.J.B., 1997, A review of melt migration processes in the adiabatically upwelling mantle beneath oceanic spreading ridges: *Phil. Trans. R. Soc. London*, v. 355, p. 283-318.
- Keller, W.R., J.M. Stock, S.C. Cande, and Müller, R.D., 2002, Geophysical constraints on the plate tectonic history of the Emerald Basin and South Tasman Ocean Crust southwest of New Zealand: *Eos Trans. AGU*, v. 83, p. Fall Meet. Suppl., Abstract T52A-1185.
- Kornprobst, J., and Tabit, A., 1988, Plagioclase-bearing ultramafic tectonites from the Galicia margin (Leg 103, Site 637); comparison of their origin and evolution with low-pressure ultramafic bodies in Western Europe: *Proceedings of the Ocean Drilling Program, Scientific Results*, v. 103, p. 253-268.
- Lahitte, P., 2003, Silicic central volcanoes as precursors to rift propagation; the Afar case: *Earth and Planetary Science Letters*, v. 207, p. 103-116.
- Lamarche, G., Collot, J.Y., Wood, R.A., Sosson, M., Sutherland, R., and Delteil, J., 1997, The Oligocene-Miocene Pacific-Australia plate boundary, south of New Zealand: Evolution from oceanic spreading to strike-slip faulting: *Earth and Planetary Science Letters*, v. 148, p. 129-139.

- le Roex, A.P., Dick, H.J.B., and Watkins, R.T., 1992, Petrogenesis of anomalous K-enriched MORB from the Southwest Indian Ridge; 11 degrees 53'E to 14 degrees 38'E: *Contributions to Mineralogy and Petrology*, v. 110, p. 253-268.
- Lenoir, X., Garrido, C.J., Bodinier, J.-L., and Dautria, J.-M., 2000, Contrasting lithospheric mantle domains beneath the Massif Central (France) revealed by geochemistry of peridotite xenoliths: *Earth and Planetary Science Letters*, v. 181, p. 359-375.
- Li, Z.-X., and Powell, C.M., 2001, An outline of the palaeogeographic evolution of the Australasian region since the beginning of the Neoproterozoic: *Earth-Science Reviews*, v. 53, p. 237-277.
- Lin, J., Purdy, G.M., Schouten, H., Sempere, J.C., and Zervas, C., 1990, Evidence from gravity data for focused magmatic accretion along the Mid-Atlantic Ridge: *Nature*, v. 344, p. 627-632.
- Lowell, J.D., 1972, Spitsbergen Tertiary Orogenic Belt and the Spitsbergen Fracture Zone: *Geological Society of America Bulletin*, v. 83, p. 3091-3102.
- Macdonald, K.C., Castillo, D.A., Miller, S.P., Fox, P.J., Kastens, K.A., and Bonatti, E., 1986, Deep-tow studies of the Vema fracture zone; 1, Tectonics of a major slow slipping transform fault and its intersection with the Mid-Atlantic Ridge: *Journal of Geophysical Research*. v. 91, p. 3334-3354.
- MacLeod, C.J., Allerton, S., Gass, I.G., and Xenophontos, C., 1990, Structure of a fossil ridge-transform intersection in the Troodos Ophiolite: *Nature London*, v. 348, p. 717-720.
- Marks, K.M., and Stock, J.M., 1997, Early Tertiary gravity field reconstructions of the Southwest Pacific: *Earth and Planetary Science Letters*, v. 152, p. 267-274.
- Massell, C., Coffin, M.F., Mann, P., Mosher, S., Frohlich, C., Duncan, C.S., Karner, G., Ramsay, D., and Lebrun, J.F., 2000, Neotectonics of the Macquarie Ridge Complex, Australia-Pacific plate boundary: *Journal of Geophysical Research-Solid Earth*, v. 105, p. 13457-13480.
- Mawson, D., and Blake, L.R., 1943, Macquarie island, its geography and geology, Volume 5, Australasian Antarctic Expedition Science Report, series A.

- Meckel, T., Coffin, M., Mosher, S., Symonds, P., Bernadel, G., and Mann, P., in press, Underthrusting at the Hjort Trench, Australian-Pacific Plate Boundary: Incipient Subduction?: Geochemistry, Geophysics, Geosystems.
- Metzger, E.P., Miller, R.B., and Harper, G.D., 2002, Geochemistry and tectonic setting of the ophiolitic Ingalls Complex, North Cascades, Washington; implications for correlations of Jurassic Cordilleran ophiolites: *Journal of Geology*, September, v. 110, p. 543-560.
- Meurer, W.P., Sturm, M.A., Klein, E.M., and Karson, J.A., 2001, Basalt compositions from the Mid-Atlantic Ridge at the SMARK area (22 degrees 30'N to 22 degrees 50'N) - implications for parental liquid variability at isotopically homogeneous spreading centers: *Earth and Planetary Science Letters*, v. 186, p. 451-469.
- Miller, C., Thoeni, M., Frank, W., Schuster, R., Melcher, F., Meisel, T.Z., and Zanetti, A., 2003, Geochemistry and tectonomagmatic affinity of the Yungbwa Ophiolite, SW Tibet, *Lithos*, V.66, p. 155-172.
- Mitchell, N., Escartin, J., and Allerton, S., 1998, Detachment faults at mid-ocean ridges garner interest: *Eos, Transactions, American Geophysical Union*, March, v. 79, p. 127.
- Mitchell, N.C., Tivey, M.A., and Gente, P., 2000, Seafloor slopes at mid-ocean ridges from submersible observations and implications for interpreting geology from seafloor topography: *Earth and Planetary Science Letters*, v. 183, p. 543-555.
- Miyashiro, A., 1973, The Troodos ophiolitic complex was probably formed in an island arc: *Earth and Planetary Science Letters*, v. 19, p. 218-224.
- Moores, E.M., and Vine, F.J., 1971, The Troodos Massif, Cyprus and other ophiolites as oceanic crust; evaluation and implications, a discussion on the petrology of igneous and metamorphic rocks from the ocean floor: *Philosophical Transactions of the Royal Society of London, Series A: Mathematical and Physical Sciences*, v. 268, p. 443-466.
- Morishita, T., Arai, S., and Green, D.H., 2003, Evolution of low-Al orthopyroxene in the Horoman peridotite, Japan: and unusual indicator of metasomatizing fluids: *Journal of Petrology*, v. 44, p. 1237-1246.

- Navon, O., and Stolper, E., 1987, Geochemical consequences of melt percolation: the upper mantle as a chromatographic column: *Journal of Geology*, v. 95, p. 285-307.
- Naylor, M.A., Mandl, G., and Sijpesteijn, C.H.K., 1986, Fault geometries in basement-induced wrench faulting under different initial stress states: *Journal of Structural Geology*, v. 8, p. 737-752.
- Niu, Y., and Batiza, R., 1997, Trace element evidence from seamounts for recycled oceanic crust in the eastern Pacific mantle: *Earth and Planetary Science Letters*, v. 148, p. 471-483.
- Niu, Y., Bideau, D., Hekinian, R., and Batiza, R., 2001, Mantle compositional control on the extent of mantle melting, crust production, gravity anomaly, ridge morphology, and ridge segmentation: a case study at the Mid-Atlantic Ridge 33-35 degrees N: *Earth and Planetary Science Letters*, v. 186, p. 383-399.
- Niu, Y., and Hekinian, R., 1997, Spreading-rate dependence of the extent of mantle melting beneath ocean ridges: *Nature*, v. 385, p. 326-329.
- Niu, Y., Regelous, M., Wendt, I.J., Batiza, R., and O'Hara, M.J., 2002, Geochemistry of near-EPR seamounts; importance of source vs. process and the origin of enriched mantle component: *Earth and Planetary Science Letters*, v. 199, p. 327-345.
- Ohara, Y., Yoshida, T., Kato, Y., and Kasuga, S., 2001, Giant megamullion in the Parece Vela backarc basin: *Marine Geophysical Researches*, v. 22, p. 47-61.
- Peacock, S.M., 1990, Fluid processes in subduction zones: *Science*, v. 248, p. 329-337.
- Pearce, J.A., 1983, Role of the sub-continental Lithosphere in magma genesis at active continental margins, in Hawkesworth, C.J., and Norry, M.J., eds., *Continental Basalts and Mantle Xenoliths*: Cheshire, Shiva Publishing Ltd., p. 230-249.
- Pearce, J.A., Barker, P.F., Edwards, S.J., Parkinson, I.J., and Leat, P.T., 2000, Geochemistry and tectonic significance of peridotites from the South Sandwich arc-basin system, South Atlantic: *Contributions to Mineralogy Petrology*, v. 139, p. 36-53.

- Polat, A., Hofmann, A.W., Munker, C., Regelous, M., and Appel, P.W., 2003, Contrasting geochemical patterns in the 3.7-3.8 Ga pillow basalt cores and rims, Isua greenstone belt, Southwest Greenland: implications for postmagmatic alteration processes: *Geochimica et Cosmochimica Acta*, v. 67, p. 441-457.
- Reid, I., and Jackson, R., 1981, Oceanic spreading rate and crustal thickness: *Marine Geophysical Researches*, v. 5, p. 165-172.
- Reiners, P.W., 2002, Temporal-compositional trends in intraplate basalt eruptions: Implications for mantle heterogeneity and melting processes: *Geochemistry, Geophysics, Geosystems*, v. 3.
- Reston, T.J., Weinrebe, W., Grevemeyer, I., Flueh, E.R., Mitchell, N.C., Kirstein, L., Kopp, C., and Kopp, H., 2002, A rifted inside corner massif on the Mid-Atlantic Ridge at 5°S: *Earth and Planetary Science Letters*, v. 200, p. 255-269.
- Ross, K., and Elthon, D., 1997, Extreme incompatible trace-element depletion of diopside in residual mantle from south of the Kane F.Z: *Proceedings of the Ocean Drilling Program, Scientific Results*, v. 153, p. 277-284.
- Searle, M., and Cox, J., 1999, Tectonic setting, origin, and obduction of the Oman Ophiolite: *Geological Society of America Bulletin*, January, v. 111, p. 104-122.
- Selkirk, P.M., Adamson, D.A., and Wilson, M.E., 1990, Raised marine terrace on north-west coast of Macquarie Island: *Proceedings of the Linnean Society of New South Wales*, v. 112, p. 141-142.
- Sen, G., Frey, F.A., Shimizu, N., and Leeman, W.P., 1993, Evolution of the lithosphere beneath Oahu, Hawaii; rare earth element abundances in mantle xenoliths: *Earth and Planetary Science Letters*, v. 119, p. 53-69.
- Sen, G., Yang, H.-J., and Ducea, M., 2003, Anomalous isotopes and trace element zoning in plagioclase peridotite xenoliths of Oahu (Hawaii); implications for the Hawaiian Plume, *Earth and Planetary Science Letters*, v.207, p. 23-38.
- Severinghaus, J.P., 1988, High inside corners at ridge-transform intersections: *Marine Geophysical Researches*, v. 9, p. 353-367.

- Seyler, M., and Bonatti, E., 1997, Regional-scale melt-rock interaction in theherzolitic mantle in the Romanche fracture zone (Atlantic Ocean): *Earth and Planetary Science Letters*, v. 146, p. 273-287.
- Shimizu, N., and Hart, S.R., 1982, Applications of the ion microprobe to geochemistry and cosmochemistry: *Annual Review of Earth and Planetary Sciences*, v. 10, p. 483-526.
- Simonian, K.O., and Gass, I.G., 1978, Arakapas fault belt, Cyprus; a fossil transform fault: *Geological Society of America Bulletin*, v. 89, p. 1220-1230.
- Sinton, J.M., Wilson, D.S., Christie, D.M., Hey, R.N., and Delaney, J.R., 1983, Petrologic Consequences of Rift Propagation on Oceanic Spreading Ridges: *Earth and Planetary Science Letters*, v. 62, p. 193-207.
- Smith, D.K., Humphris, S.E., Tivey, M.A., and Cann, J.R., 1997, Viewing the morphology of the Mid-Atlantic Ridge from a new perspective: *Eos, Transactions, American Geophysical Union*, July, v. 78, p. 269.
- Smith, W.H.F., and Sandwell, D.T., 1997, Global sea floor topography from satellite altimetry and ship depth soundings: *Science*, v. 277, p. 1956-1962.
- Suhr, G., and Edwards, S.J., 2000, Contrasting mantle sequences exposed in the Lewis Hills Massif; evidence for the early arc-related history of the Bay of Islands ophiolite: *Special Paper Geological Society of America*, v. 349, p. 433-442.
- Sutherland, R., and Norris, R.J., 1995, Late Quaternary displacement rate, paleoseismicity, and geomorphic evolution of the Alpine Fault; evidence from Hokuri Creek, South Westland, New Zealand: *New Zealand Journal of Geology and Geophysics*, v. 38, p. 419-430.
- Sylvester, A.G., and Smith, R.R., 1976, Tectonic transpression and basement-controlled deformation in San Andreas fault zone, Salton Trough, California: *AAPG Bulletin*, v. 60, p. 2081-2102.
- Takazawa, E., Frey, F., Shimizu, N., and Obata, M., 1996, Evolution of the Horoman Peridotite (Hokkaido, Japan); implications from pyroxene compositions, *Chemical Geology*, v. 134, p. 3-26.

- Thompson, R.N., 1994, Magmatic expression of lithospheric thinning across continental rifts: *Tectonophysics*, v. 233, p. 41-68.
- Van Orman, J.A., Grove, T.L., and Shimizu, N., 2001, Rare earth element diffusion in diopside: influence of temperature, pressure, and ionic radius, and an elastic model for diffusion in silicates: *Contributions to Mineralogy and Petrology*, v. 141, p. 687-703.
- Varne, R., Gee, R., and Quilty, P., 1969, Macquarie island and the cause of oceanic linear magnetic anomalies: *Science*, v. 166, p. 230-233.
- Varne, R., Brown, A.V., and Falloon, T., 2000, Macquarie Island; its geology, structural history, and the timing and tectonic setting of its N-MORB to E-MORB magmatism: *Special Paper - Geological Society of America*, v. 349, p. 301-320.
- Varne, R., and Rubenach, M.J., 1971, The petrology of Macquarie Island, southern ocean: *Proceedings of the Pacific Science Congress*, v. 12, p. 456.
- , 1972, Geology of Macquarie Island and its relationship to oceanic crust: *Antarctic Research Series*, v. 19, p. 251-266.
- von der Handt, A., Snow, J.E., Hellebrand, E., Dick, H.J.B., and Michael, P., 2002, Plagioclase peridotites: subsolidus breakdown or trapped melt?: *Geochimica Et Cosmochimica Acta*, v. 66, p. A810-A810.
- Wakabayashi, J., and Dilek, Y., 2001, What constitutes 'emplacement' of an ophiolite?: *Abstracts with Programs - Geological Society of America*, v. 33, p. 226.
- Wertz, K.L., Danyushevsky, L.V., Mosher, S., and Kamenetsky, V.S., in prep, Temporal patterns of incompatible-element enrichment in Macquarie Island basalts.
- Wertz, K., Daczko, N. R., Mosher, S., Coffin, M.F., 2000a. Macquarie Island's Finch-Langdon Fault zone: a ridge-transform corner structure preserved along the Pacific-Australian plate boundary, *GSA Abstracts with Programs*, v. 32, n. 7, p. A-237.
- Wertz, K., Daczko, N. R., Mosher, S., Coffin, M.F., 2000b. Transition from spreading ridge to transform plate boundary: integration of marine

- geophysical data and field data from Macquarie Island, *Eos, Trans. AGU*, v. 81 (48), F1078-1079
- Wilcox, R.E., 1973, Basic Wrench Tectonics: American Association of Petroleum Geologists Bulletin, v. 57, p. 74-96.
- Williamson, P., 1974, Recent studies of Macquarie Island and the Macquarie Ridge Complex: Bulletin - Australian Society of Exploration Geophysicists, v. 5, p. 19-22.
- , 1979, The palaeomagnetism of outcropping oceanic crust on Macquarie Island: *Journal of the Geological Society of Australia*, v. 25, Part 7-8, p. 387-394.
- Williamson, P., Hawkins, L.V., and Long, B., 1981, An examination of the possible occurrence of sea-floor spreading magnetic anomalies on Macquarie Island: *Marine Geophysical Researches*, v. 5, p. 139-155.
- Williamson, P., and Rubenach, M.J., 1972, Preliminary report on geophysical studies on Macquarie Island: *Antarctic Research Series*, v. 19, p. 243-249.
- Williamson, P.E., 1988, Origin, structural and tectonic history of the Macquarie Island region: *Papers and Proceedings of the Royal Society of Tasmania Royal Society of Tasmania*, v. 122, p. 27-43.
- Wood, R., Lamarche, G., Herzer, R., Delteil, J., and Davy, B., 1996, Paleogene seafloor spreading in the southeast Tasman Sea: *Tectonics*, v. 15, p. 966-975.

## Vita

Karah Lynn Wertz was born February 6, 1971, in Columbus, Ohio to Lana Jean (née Duemmel) and Eugene Ralph Wertz. Her family moved to Cupertino, California in 1971. She discovered geology while an employee of Hodges Figgis Booksellers (Dublin, Ireland), when she read a book that was “recommended” for a geology course at Trinity College, which she picked up because she was intrigued by the large number of students purchasing this book that was not “required”. She returned to California and enrolled at De Anza College, where she was taught geology by Edward “Sandy” Hay, completing her studies at University of Wyoming (B.Sc., 1997). Her senior thesis “Testing tilting of the footwall to a major low angle fault: geobarometric constraints from the syntectonic Sacram Suite, Southeastern California” was supervised by Prof. Barbara “Bobbie” John. As an undergraduate and immediately following graduation, she did internships with Burlington Resources in Houston and Midland, Texas and for Marathon Oil Company in Anchorage, Alaska. She began her graduate study at the University of Texas at Austin in 1998. While working toward her degree, she spent a summer studying ophiolites in the Cascade Mountains in central Washington and in the Klamath Mountains in Oregon and California. She also spent 11 months in the field on Macquarie Island, which was a life-changing experience.

Permanent address: 10581 Madera Drive, Cupertino, California, 95014 U.S.A.

This dissertation was typed by the author.